Domain II (S5-P) region in *Lymnaea* T-type calcium channels and its role in determining biophysical properties, ion selectivity and drug sensitivity

by

Wendy Guan

A thesis
presented to the University of Waterloo
in fulfillment of the
thesis requirement for the degree of
Master of Science
in
Biology

Waterloo, Ontario, Canada, 2014

AUTHOR'S DECLARATION

I hereby declare that I am the sole author of this thesis. This is a true copy of the thesis, including any required final revisions, as accepted by my examiners.

I understand that my thesis may be made electronically available to the public.

Abstract

Invertebrate T-type calcium channels cloned from the great pond snail, *Lymnaea Stagnalis* (LCav3) possess highly sodium permeant ion channel currents by means of alternative splicing of exon 12. Exon 12 is located on the extracellular turret and the descending helix between segments 5 and segments 6, upstream of the ion selectivity filter in Domain II. Highly-sodium permeant T-type channels are generated without altering the selectivity filter locus, the primary regulatory domain known to govern ion selectivity for calcium and sodium channels. Comparisons of exon 12 sequences between invertebrates and vertebrate T-type channels reveals a conserved pattern of cysteine residues. Calcium-selective mammalian T-type channels possess a single cysteine in exon 12 in comparison to invertebrate T-type channels with either a tri- or penta- cysteine framework. Cysteine residues in exon 12 were substituted with a neutral amino acid, alanine in LCav3 channels harbouring exon 12a and 12b to mimic the turret structure of vertebrate T-type channels. The results generated T-type channels that were even more sodium-permeable than the native T-type channels in snails. Furthermore, permeant divalent ions similar in structure to calcium (eg. barium) were unable to sufficiently block the monovalent ion current of channels lacking cysteines in Domain II, suggesting that the pore is highly sodium permeant, and has weak affinity and block by permeant divalent ions other than calcium. Besides ion selectivity, the cysteine mutated T-type channels were 10 to 100 fold more sensitive to inhibition by nickel and zinc, respectively. The cysteine mutation data highly suggests that the cysteines form an extracellular structure that regulates ion selectivity and shields T-type channels from block by nickel and zinc. In addition, we replaced exon 12 from the sodium permeant snail T-type channel with exon 12 from human Cav3.2 channels. The snail T-type channel with exon 12 from human T-type channels produced a T-type channel that was modestly sodium permeable, but did not confer the high calcium permeability of Cav3.2 channels. These findings suggest that the cysteine containing extracellular domains in exon 12 are not sufficient to generate calcium selective channels similar to human Cav3.2 and likely work in concert with other extracellular domains to regulate the calcium or sodium selectivity of T-type channels.

Acknowledgements

My time here at Waterloo has been an incredible, long and rewarding experience, I have encountered great people and brilliant scientists. Dr. J. David Spafford, I would like to thank you for investing your time and energy into me. Your enthusiasm to this research project would not be as far along without your guidance and keenness to publish, traits I find astounding and commendable. At bleak moments, you have supported and encouraged me and most importantly, believed in my skills and abilities. I appreciate the trust you have gained for me over the years, building my confidence as a scientist.

To my committee members, Dr. Bruce Mckay, Dr. Gaynor Spencer and Dr. Matthijs van der Meer, thank you for taking the time to read my thesis. Your advice and expertise throughout this process is greatly appreciated. I would also like to acknowledge Dr. Adriano Senatore, this project would not have started without him, who spent two years cloning the *Lymnaea* T-type calcium channel. I am very grateful to have worked with and be mentored by a compassionate and dedicated scientist as yourself. Dr. Adrienne Boone, I have gained a valuable friendship, one that will be dearly missed when I leave. Your patience, guidance, advice and friendship is priceless to me and has made me a better scientist for it.

Dr. Jean-Philippe Thivierge and Dr. Leonard Maler, thank you providing me the opportunity to conduct research in your laboratories as an inexperienced undergraduate and starting me on this journey. Your enthusiasm for neuroscience is contagious and inspiring to many future neuroscientists.

I have formed many wonderful friendships over the years, these people were there for me when science was at its worst. Thank you to Darryl Jones, Julia Fux, Eve Suman, Minhee Kim, Aaron Robertson, Elizabeth Drolle, Dinu Nesan, Erin Fraught, Laura Dindia, Carol Best, Nataliya Melnyk-Lamont, Robert Stephens, Wilten Nicola, Arthur Wong, Bonnie Au, and Kathleen Vincent.

Finally, my family. To my mother and father, you have watched me grow and continued to encourage me to pursue my interests. Your love for your daughter is expressed

in the strangest ways, but has motivated me to continue with my own career path. My sisters, Berniz and Rebecca, you were role models for me when I was growing up and have provided love and support unconditionally. I am very grateful for everyone I have encountered and for those that continue to be active within my life, thank you.

Dedication

To my loved ones,
past, present and future.

Table of Contents

List of Figures

List of Tables

List of Abbreviations

AMFE	Anomalous mole fraction effect
CCD	Couple charged device
DMEM	Dulbecco's modified Eagle's medium
EGTA	ethylene glycol tetraacetic acid
FBS	Fetal bovine serum
HEK293T	Human embryonic kidney 293T
HEPES	4-(2-hydroxyethyl)-1-piperazineethanesulfonic acid
HES	HEPES-buffer saline
HPRT1	hypoxanthine phosphoribosyltransferase 1
HVA	High voltage activated
LB	Luria Bertani
LTS	Low threshold spike
LVA	low voltage activated
NEB	New England Biolabs
NMDG	N-methyl-D-glucamine
SB	Super Broth
TEA	Tetraethylammonium
TM	Transmembrane
TTA-P2	3,5-dichloro-N-[1-(2,2-dimethyl-tetrahydro-pyran-4-ylmethyl)-4-fluoro-piperidin-4-ylmethyl]-benzamide

Chapter 1
Introduction

1.1 Evolutionary origins of voltage gated ion channels

Voltage gated ion channels contribute to the electrical excitability and action potentials to control internal processes such as muscle contraction, secretion, and synaptic transmission. The simplest structural form of these ion channels are the inward rectifying potassium channels (K_{ir}). They consist of a pore domain with two transmembrane segments separated by a pore-loop (P-loop) (Anderson & Greenberg, 2001). Two pore domains linked together form four transmembrane (TM) segments, this generates members of the potassium leak conductance or two pore (K_{2P}) channel. Six transmembrane segments generated voltage-gated potassium channels and hyperpolarization-activated cyclic nucleotide (HCN) channels (Anderson & Greenberg, 2001; Hille, 2001). Channels containing six transmembrane segments have a voltage-sensor domain, a hallmark feature of voltage-gated channels. The fourth segment of the voltage sensor domain contains repeating positive charges every third amino acid. This charged segment moves outward in response to changes to the membrane electric field along a set of countercharges in segments 2 and 3 of the voltage-sensor domain, and imparts opening of the pore domain to which it is attached through a S4-S5 cytoplasmic linker (Catterall, 2010).

The six transmembrane motif of voltage-gated channels consisting of a voltage-sensor domain and a pore domain, provides the structural basis of eukaryotic potassium, sodium and calcium channels. Typically, in potassium channels, the pore forming subunit consists of four repeat subunits forming homomultimers or heteromultimers with members within the same potassium channel family (Anderson & Greenberg, 2001). Sodium and calcium channels and sodium leak conductance channel (NALCN) contain a single long polypeptide that encompasses all four domains of twenty-four segments, with each domain separated by a cytoplasmic linker between domains I-II, II-III and III-IV. The remainder of this section will focus on the how sodium and calcium channels (and NALCN) evolved from a single six TM motif like a voltage-gated potassium channel (Hille, 2001; Senatore & Spafford, 2010; Senatore & Spafford, 2013).

The evolution of the four repeat domains of sodium and calcium channels is apparent in the greater similarities between domain pairs. Domains I and III have greater similarities with each other, and the same goes for domains II and IV, which are more similar to each other. Strong

and colleagues (1993) suggested that the singleton domain duplicated and then after a period of time allowed divergence to occur for these domains. Subsequently, domains I and domains II each duplicated to generate the four domain sodium and calcium channels, and NALCN template. This scheme of evolution of domains necessitates a two domain intermediate channel at some point in time. See Figure 1.1 and 1.2a for a phylogeny tree of voltage gated ion channels and the proposed duplication of domains that generated the sodium and calcium channels.

The functional diversity of calcium channel types was first identified by Susumo Hagiwara and colleagues in starfish eggs as 'Channel I' and 'Channel II' calcium selective currents. These two channel types in starfish eggs represent the two categories of calcium channels separable by voltage: the low-voltage activated (LVA) channels and the high-voltage activated (HVA) channels (Hagiwara, Ozawa & Sand, 1975; Hille, 2001). Ten different mammalian genes coding for calcium channels are known, four belong to the Ca_v1 channel class (L-type), three for the Ca_v2 channel class (P/Q, N- and R- type) and three for Ca_v3 channel class (T-type), see Figure 1.2b for phylogenetic tree of calcium channels. Ca_v1 and Ca_v2 are classified as HVA calcium channels because they both require a large depolarization (more positive than -40mV) to activate, while Ca_v3 channels will activate at much lower voltages (less positive than -40 mV) (Hille, 2001; Zamponi, 2005). There are three Ca_v3 channel genes in vertebrates: $Ca_v3.1$ (α_{1G}), Ca_v 3.2 (α_{1H}) and $Ca_v3.3$ (α_{1I}). Within these channels there is significant variation in kinetics, drug blocking effects and ion permeation differences. Unlike the vertebrate channels, invertebrates, such as the pond snail, *Lymnaea stagnalis* only has one gene that codes for each calcium channel category, designated as LCa_v1, LCa_v2 and LCa_v3 (Senatore & Spafford, 2010). The simplicity in the number of genes provides opportunities to gain insight on the fundamental features of LVA channels. Vertebrate Cav3 channels have been difficult to characterize because the three different vertebrate genes cannot be easily distinguished by drugs or biophysical features.

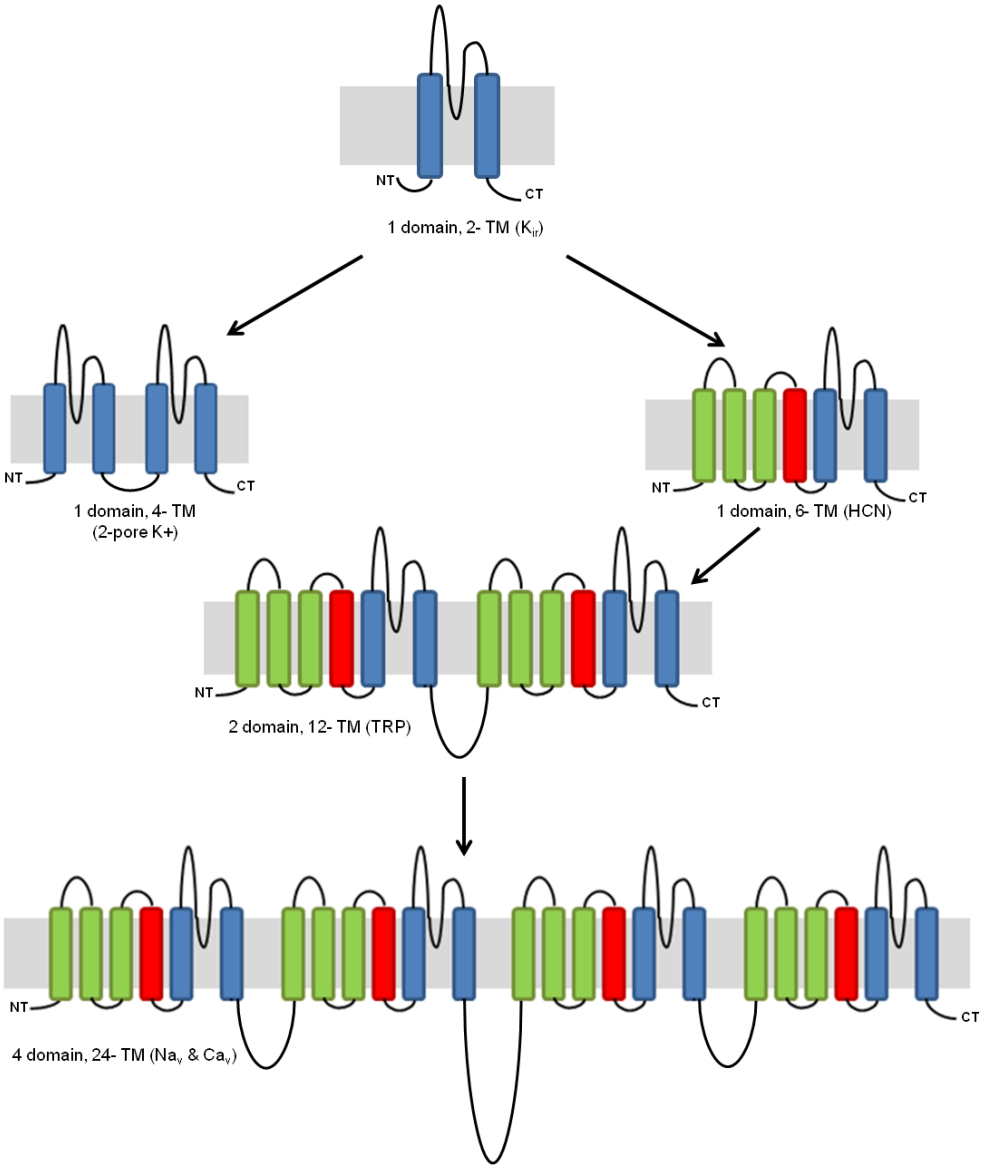

Figure 1.1 Proposed evolutionary origins of voltage gated ion channels.

Transmembrane segments (TM) are denoted by long rectangles, with the green rectangles representing S1-S3 segments, red denotes S4 segments and blue is S5-S6 segments. The TM are separated by intra- and extracellular linkers in black and the amino- and carboxyl- termini are labeled as NT and CT respectively. The basic building block of voltage-gated ion channels is a 2 TM segments with a pore (P-) loop connecting between them, like an inward rectifying potassium channel (K_{ir}). Pore duplication create a 4TM (eg. 2-pore potassium channel) and addition of a voltage sensor generates 6TM channels (eg. hyperpolarized- activated cyclic nucleotide-gated (HCN)). Duplication of the 6 TM voltage-gated K+ channel creates a 12 TM intermediate (eg. transient receptor potential channel (TRP)) and a second round of duplication results in the 24 TM ion channels evident in sodium and calcium channels.

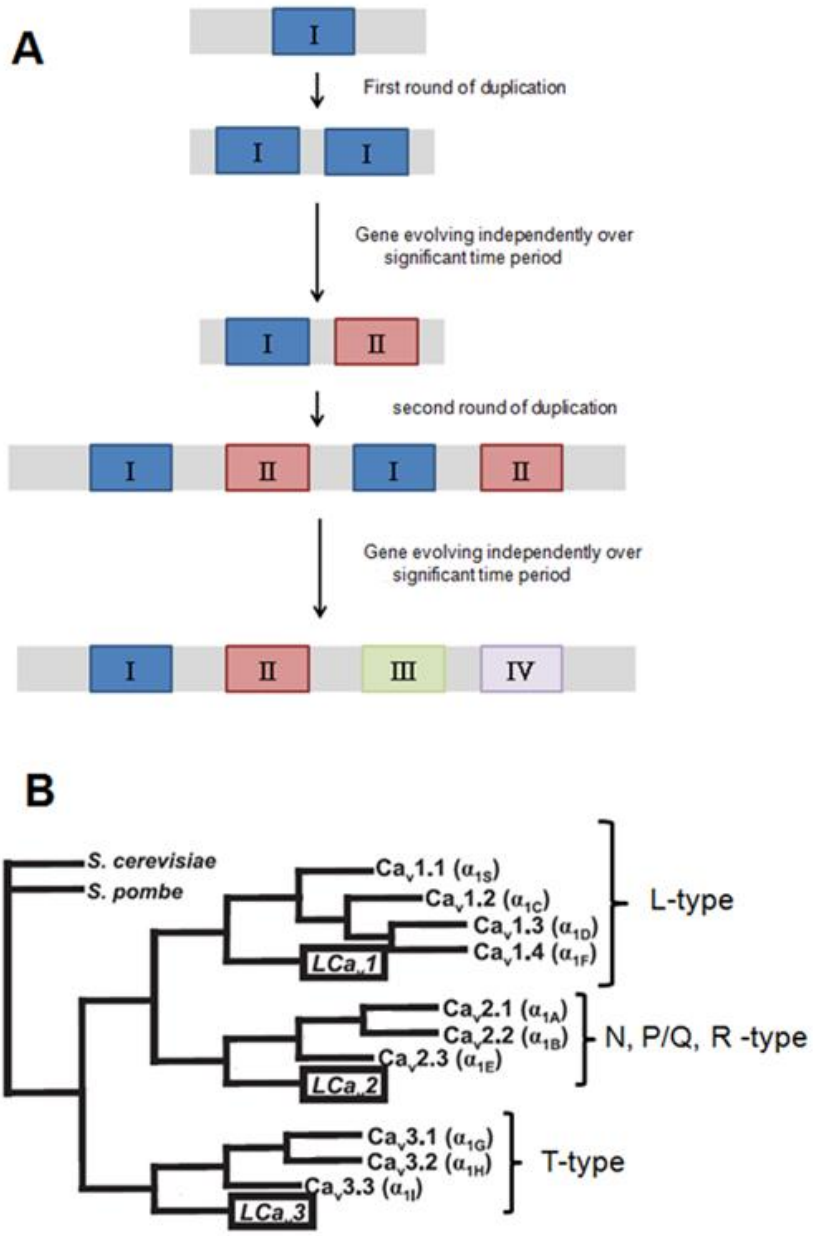

Figure 1.2 Evolutionary diagram of ion channel domains and the phylogenetic tree of calcium channels.

(A) A proposed scheme of how domains evolved in sodium and calcium channels. One repeat channel went through two rounds of duplication with gene divergence occurring in between the domain duplications to create four distinct but homologous repeat domains. (B) A phylogenetic tree illustrating snail and mammalian voltage-gated calcium channels. There are four mammalian genes for Ca_v1, three for Ca_v2 and three for Ca_v3. The pond snail, *Lymnaea stagnalis* has only a single gene for each calcium channel class (LCa_v1, LCa_v2 and LCa_v3). The out group shown on the phylogenetic tree is fungal calcium channels from *Saccharomyces cerevisiae* and *Schizosaccharomyces pombe* (Reproduced from Senatore & Spafford, 2010).

1.2 Structural model of T-type calcium channels

A common feature of calcium channels is the pore-forming α_1 subunit. High voltage activated (HVA) calcium channels differ from low-voltage activated (LVA) calcium channels, by requiring additional auxiliary subunits such as β, γ, and $\alpha_2\delta$ to function. This chapter will be limited to a discussion of the primary pore forming subunit of T-type calcium channels, the α_1 subunit. The α_1 subunit is a long polypeptide connected together by four homologous domains (DI- IV), each domain contains six transmembrane segment (S1-S6). The N- and C- terminus and the three linkers (I-II, II-III and III-IV) are located intracellularly. Key features of the T-channels include a voltage sensor, selectivity filter and gating brake (Hille,2001; Zamponi, 2005; Senatore & Spafford, 2011).

1.2.1 Voltage sensor

The voltage sensor in voltage-gated ion channels respond to changes in the membrane electric field to open or close the channel. The voltage sensing region is comprised of S1 to S4 segments, with the S4 segment bearing repeating positive charges that senses voltage-changes. All voltage-gated channels share a similar structure arrangement of one positive charge every third amino acid (either lysine or arginine) in each of the S4 transmembrane segments (Hille, 2001; Perez-Reyes, 2003). During a depolarization, the positivity charged S4 transmembrane segments induces a conformational change by moving outward to initiate channel opening or activation (Baumgart et al, 2008; Catterall, 2010).

1.2.2 The membrane pore and selectivity filter

The hypothesized structure of the pore for calcium channels contains a large outer vestibule funneling to a narrow, tight pore that leads into an aqueous pore cavity within the membrane, see Figure 1.3 C for a two dimensional topology map (Catterall,1995). The outer vestibule is made up of S5 and S6 linkers which contains an outer turret, descending helix, a selectivity filter and an ascending helix, see Figure 1.3B for structural layout of these determinants. The extracellular turret emerges from the S5 transmembrane helix and then descends into the pore with a descending pore helix, which then turns upwards to a selectivity filter to an ascending pore helix generating a re-entrant or hairpin shaped, P-loop (Catterall, 1995; Hille, 2001; Senatore, Zhorov & Spafford, 2012).

Ionic conduction through the channel is primarily governed by a selectivity filter and has the ability to discriminate between ions. The selectivity filter is made up of a single amino acid in the same position in the four P-loops located between S5-S6 in all four domains. In HVA channels, the conserved amino acid sequence for the selectivity filter are four glutamates (E), EEEE, while LVA channels differ with two glutamates and two aspartates (D), EEDD. These residues form a ring that lie close to the extracellular mouth of the pore and it is proposed that the carboxylate side chains of glutamate allow for high affinity binding to divalent cations to create a multi-ion pore (Nosal et al., 2013). However, since T-type channels contain two aspartates, their carboxylate side chains are shorten and are expected to bind calcium at a weaker affinity. This tradeoff allows for Cav3 channels to have faster kinetics and reduced sensitivity for calcium over monovalent ions (Senatore, Zhorov & Spafford, 2012). Mechanisms on how the selectivity filter works is mentioned in section 1.4.

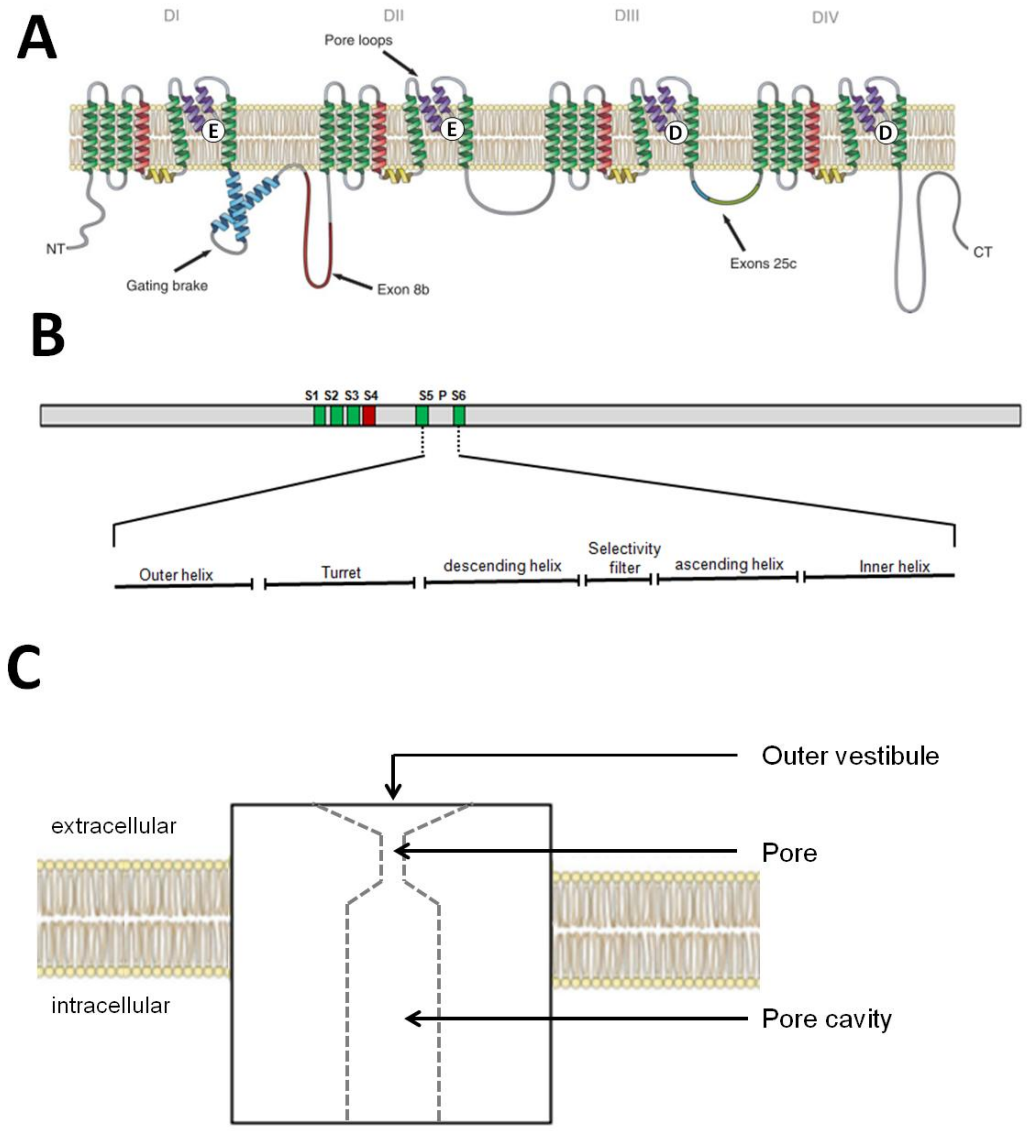

Figure 1.3 Structural determinants of a T-type channel.

(A) Depiction of T-type calcium channel structure: A single long polypeptide containing four domains, each with 6 transmembrane segments. Green transmembrane segments are S1 –S3 and S5-S6, red represents the voltage sensor S4. In between S5 and S6 lies the pore loop (P-loop) and within each P-loop is a key amino acid governing ion selectivity within the selectivity filter. The I-II linker contains the gating brake and exon 8b and the III-IV linker contains exon 25c. (Reproduced from Senatore, Zhorov & Spafford, 2012) (B) A close-up of the structural determinants between S5-S6 linker. The outer helix refers to S5 and the inner helix is S6, in between them contains an extracellular loop called the turret, and a descending pore helix and ascending pore helix that flank the selectivity filter within the membrane. (C) A proposed 2D topology map of a calcium channel pore, illustrating the extracellular outer vestibule that funnels down into a narrow pore leading into a pore cavity.

1.2.3 Gating brake and membrane expression

Gating kinetics such as inactivation and activation are modulated by structural components within the α1 subunit. A highly conserved arrangement amongst all voltage gated channel is an "inverted tepee" configuration made up of the four S6 helices, together they act as the inactivation gate that prevents the passage of ions through the aqueous pore cavity (Senatore, Zhorov & Spafford, 2012). The helical S6 in domain I extends into the cytoplasmic I-II linker, to form a binding platform to couple β subunits, this is known as the Alpha Interaction Domain (AID) and modulates kinetic gating in HVA channels. In contrast, LVA channels have lost this motif and replaced with a 62 amino acid region that forms a helix-loop-helix structure known as the gating brake (Zamponi, 2005; Vitko et al., 2007). The gating brake provides regulatory function for gating kinetics in T-type calcium channels and stabilizes the channel in a closed state, in a manner that parallels the role of the beta subunit in its regulation of Cav1 and Cav2 channels (Perez-Reyes, 2010). In Cav3 channels, deletions of this region causes activation and inactivation kinetics to occur at more hyperpolarized potentials (Vitko et al., 2007; Arias-Oluin et al., 2008; Baumgart et al., 2008). However, mechanisms on how the gating brake interacts with the pore domain to regulate the voltage-dependent channel opening and inactivation remains unclear. Within the I-II linker, downstream of the gating brake, lies a region encompassed by exon 8b that is responsible for membrane trafficking of T-type channels (Senatore & Spafford, 2010). Omission of optional exon 8 in snail LCav3 and Cav3.1 channels causes a twofold increase in current density. The effect of the deletion in the distal portion of the I-II linker is different for different T-type channels, and corresponds to a ~3.7 increase in size of channel currents for Cav3.2 and a decrease of ~1.7 in channel currents for Cav 3.3 (Arias-Oluin et al., 2008; Baumgart et al., 2008). Hotspot cluster of mutations in the I-II linker have been identified in Cav 3.2 T-type channels for Chinese patients with childhood absence epilepsy (CAE). Twelve single amino acid mutations in the I-II loop of Cav3.2 gene were found in these patients and seven of these mutations had the effect of increasing membrane trafficking in Cav3.2 channels. Models predict that this increase in surface expression would trigger thalamo-cortical oscillations such as those observed in absence epilepsy (Perez-Reyes, 2010). Animal models in mouse absence epilepsy have supported this notion with enhanced expression of T-type currents compared to normal mice (Zhang et al., 2002).

1.3 Biophysical properties of T-type channels

Generally, ion channels are characterized in terms of their gating kinetics looking at properties such as activation, deactivation and inactivation. Activation refers to the process of ion channels opening in respond to a depolarization, whereas deactivation are channels closing in response to a repolarization, and is usually measured by tail currents. Inactivation refers to the process of an ion channel moving to a refractory state after a period of depolarization. In a voltage clamp experiment, T-type channels will open upon depolarization from a negative membrane potential of -100 mV to one that generates maximal channel opening at -35 mV. The user sees (1) a rapid inward current which is depicted by a negative current to peak (activation) followed by (2) a decay of from this initial current over time (inactivation). Typically, an ion channel in an inactivated state must have their inactivation removed, usual by hyperpolarizing the cell for a given time frame before becoming available to be activated again (Hille, 2001). The negative currents are shown as downward deflections because the voltage clamp are the compensatory currents generated by the feedback circuit of the patch clamp amplifier to keep the voltage level clamped at a particular voltage, in response to channel opening events.

1.3.1 Activation, inactivation and window currents

T-type calcium channels are distinguished from other calcium channels for their tiny conductance and transient currents when barium is the charge carrier based on single channel recordings (Perez-Reyes,2003). They are activated at low voltages, hence the classification of low voltage activated calcium channels. These channels are quick to inactivate and slow to deactivate (transition to closing from an open state). The activation voltage that triggers the most modest channel opening for T-type channels occur around -75 to -60 mV in physiological solutions, with half maximal voltages ($V_{½}$) for channel activation between -60 to -40 mV (Perez-Reyes, 2003; Talavera & Nilius, 2006). T-type channel currents typically peak around -30 mV for Cav 3.1 and Cav 3.2 isoforms and -25 mV for Cav 3.3 (Chemin et al., 2002). Increases in depolarizations will recruit more channels to a maximum generating a sigmodal curve function. Activation kinetics can be fitted with a tau constant (τ_{act}), (the time constant to reach ~2/3 of maximal channel opening). Tau decreases as the channel is triggered to open with stronger voltages for depolarization, which ranges from 8 to 15 ms decreasing to 1-2 ms during maximal activation voltage (greater than -20 mV) (Perez-Reyes, 2003). The increasingly faster responses

to channel opening τ_{act} with increasing depolarizations is a property shared for all recombinant T-type channels. Although, Cav3.1 and Cav 3.2 share similar kinetic properties to one another, Cav 3.3 displays a much slower $\tau_{act,}$ decreasing from ~80 ms to 10 ms at voltages more positive than -10 mV (Monteil et al., 2000).

Steady state inactivation is often studied alongside activation, which is measured as the percentage of channels that are in a refractory state and unavailable at a given transmembrane potential and can be described using a Boltzmann equation. Inactivation is measured at a "steady-state" where the cells are held at differing potentials for a length of time to establish an equilibrium of available and unavailable (inactivated) channels at that particular voltage. It is to measure the voltage- but not the time-dependence (kinetics) of the inactivation process (Molleman, 2003).

T-type channels typically exhibit a rapid inactivation rate with a half maximal inactivation range between -75 to -70 mV (Chemin et al., 2002; Talavera & Nilius, 2006). Similar to τ_{act}, the tau inactivation (τ_{inact}) is a curve fit of the rate of current amplitude decay with increasing time, that corresponds to an increasing fraction of channels migrating from the available to inactivated state when cells are held at a particular potential. The exponential decrease in the rate of inactivation decay varies in different channel isoforms (Chemin et al, 2001). The kinetics of inactivation, like activation increases exponentially with stronger depolarizations. There is an apparent coupling of the mechanism that governs inactivation and activation kinetics, because when mutations are made that alter the inactivation, it similarly alters the rate of activation in the same direction and vice-versa (Talavera & Nilius, 2006;Hille, 2001).

HVA calcium channels such as L-type channels have a rate of inactivation that is highly modified by the presence of calcium-calmodulin bound to the channel (Taiakina et al., 2013). This means that when the channel is depolarized the influx of calcium flows into the cell increases intracellular free calcium, that in turn activates calcium-calmodulin and rapidly increases the rate of inactivation of these calcium channels (Simms et al., 2013; Hille, 2001). This form of calcium-dependent inactivation is not present in Cav3 channels. T-type channels have a rapid calcium-independent inactivation that is rapid for calcium channels, but is slower than the inactivation kinetics for classical Nav1 sodium channels (Hille, 2001).

One of the unique biophysical characteristics in all T-type channels is the presence of a window current. A window current is defined as an overlapping region between the activation

and steady state inactivation curves (Senatore, Zhorov & Spafford, 2012). There is a measureable fraction of channels at the base of the activation curve that are open and also are not in a refractory, inactivated state. Most channels are not open and are in the refractory state, but up to 2% of channels are both open and available at a "window" of voltages, mostly near the resting membrane potential (~-65 mV), where there is a steady stream of calcium influx (Serrano, Perez-Reyes & Jones, 1999; Talavera & Nilius, 2006; Senatore, Zhorov & Spafford, 2010). Researchers have proposed that this dribble of constant calcium influx contributes to pacemaking activity during the late phase of diastolic depolarization (Zhou & Lipsius, 1994).

1.3.2 Recovery from inactivation

Recovery from inactivation, also known as reactivation, measures the duration it takes for a channel to transition from an inactivated state to one where it is available for opening (activation) again. The mechanism behind this process is thought to be related to deactivation. Burgess et al. (2000) showed that gating charge from tail currents (which provides a measure of the rate of deactivation) recovered faster than gating currents generated by activation first and made the conclusion that T-type channels recovered from inactivation via a deactivation first pathway. In terms of the three human isoforms, Cav 3.1 recovers the quickest from inactivation between from 120-140 ms, then Cav 3.3 and Cav 3.2 at 260-350 ms and 400-440 ms respectively (Klöckner et al, 1999; Chemin et al, 2001; Talavera & Nilius, 2006).

1.3.3 Deactivation

Deactivation is the rate of channel closing from the open state and is measured by tail currents in whole cell electrophysiology recordings. The cell is held at a highly depolarized membrane voltage to elicit maximal channel openings, then after a short delay, the membrane potential is dropped from this highly depolarized potential to differing voltages (Molleman, 2003). The decay rate of the current at these different voltages reflects the rate at which channels transition from the open to the closed state. The deactivation rate is very slow in T-type channels compared to HVA calcium channels, and the rate of deactivation tends to increase with hyperpolarization (Talavera & Nilius, 2006).

1.4 Current theories on ion selectivity and permeability

Most mechanisms surrounding ion selectivity and permeability have been focused on the selectivity filter locus, however, it is important to distinguish the two terms ion selectivity and permeability first. Ion selectivity refers to the channel's capability to reject or accept an ion into the pore, whereas ion permeability is defined as how readily an ionic substance can be transported through the membrane. A couple of experiments are commonly performed to investigate these properties, (1) bi-ionic reversal potential and (2) the anomalous mole fraction effect.

The bi-ionic reversal potential approach is one that looks at the relative permeabilities (P_x/P_y) of two ions (eg. P_{Ca} (permeability of calcium ions) / P_{Na} (permeability of sodium ions)) measured by their relative contribution to the reversal potential. The reversal potential is the voltage at which the current is zero and is a characteristic for each calcium and sodium ion which varies depending on the concentration gradient and electrical charge (valence) of each ion (Hille, 2001). Calcium ions and sodium ions are set up to have very different reversal potentials, because one ion is set up as an inward current (with high relative concentrations of calcium on the outside compared to inside the cell) and the sodium ion is set up as an outward current (with high relative concentration of sodium ions inside compared to outside the cell). In the bi-ionic model it is assumed that the calcium influx and sodium efflux are permeating through the ion channels independently from each other. Typically ions with smaller atomic radii will permeate more than an ion with a larger atomic radii (Hille, 2001; Sather & McCleskey, 2003; Nosko & Roux, 2006).

In addition, we can directly measure how two different ions (calcium versus sodium ions) compete and interfere with each others' permeation through the channel pore. The experimental outcome is known as the anomalous mole fraction effect (AMFE). The setup is one where the concentration of one ion is at a fixed concentration (60 mM sodium ions on the outside) and we measure the relative change in current size to increasing doses of the competing ion, in this case calcium. It leads to an "anomaly" where the increasing concentration of the second ion (calcium) leads to a decreasing size of the total current, as the second ion blocks the first ion (sodium). But at higher doses, the second ion dominates (Sather & McCleskey, 2003). The typical "U" shaped dependence of the current to increasing doses of the second ion reflects the second ion's ability to block the first ions' conduction. This leads to a monotonic decline in

the current and with increasing doses, the molar fraction of the second ion increases far beyond the first ion and becomes more permeant as doses increase (Gillespie & Boda, 2008). The "U" shaped dependence thus reflects how multiple ions compete for a limited number of binding sites in the pore which must pass in single file motion (Hille, 2001; Gillespie & Boda, 2008). A basis for understanding how channels regulate the selectivity and relative permeation of ions has come from detailed structural models derived from X-ray crystallography studies. This is introduced in the next section.

1.4.1 Potassium channels

A breakthrough in understanding the permeation of ion channels was in the work of Roderick Mackinnon's laboratory who determined the X-ray crystal structure of a bacteria inward rectifying potassium channel from *Streptomyces lividans* (KcsA) (Doyle et al. 1998). This work provided Dr. Mackinnon a share in the Nobel Prize for Medicine in 2003, and a created the foundation for understanding ion selectivity and permeation in calcium and sodium channels.

The KcsA channel is formed as a tetramer of two transmembrane segments that form the pore domain of voltage-gated potassium channels with a created signature selectivity filter sequence of TVGYG (threonine – valine – glycine – tyrosine – glycine) (Doyle et al., 1998). Like other voltage gated ion channels, potassium channels have the ability to highly discriminate amongst other cations, for example potassium (K^+) channels will select for K^+ over sodium (Na^+) molecules at ~1000:1 (Nosko & Roux, 2006). The selectivity filter of KcsA lines the narrowest constricture of the channel pore. It is a long and narrow pore with five binding sites (S0-S4), with S0 located near the extracellular mouth of the pore and S1-S4 are located inside the pore. The pore is formed by the carbonyl backbone of the signature selectivity filter residues TVGYG, see figure 1.4 (Nimigean & Allen, 2011). Potassium ions can reside in every other position, either as S0, S2 and S4 positions or the S1 and S3 positions. The driving force due to the electrochemical gradient and repulsion between ions in the pore drives potassium ions between binding sites in the multi-ion pore and out through the channel (Nimigean & Allen, 2011).

K^+ ions entering the pore selectivity filter must lose their hydration shell of water ions which is replaced by coordinated carbonyl oxygen atoms within the hydrophobic internal pore that

mimics the potassium ion's hydration shell (Doyle et al., 1998; Nosko & Roux, 2006). As K^+ ions move into the pore cavity, they must expend energy to shed their water molecules, but quickly gain energy by association in the pore selectivity filter which is designed to accommodate the dehydrated potassium ion (Berneche & Roux, 2003). The dehydrated sodium ion is smaller than the potassium ion, but is not an optimal fit for the potassium pore, and thus is not energetically favorable for passing through a potassium-selective pore (Armstrong, 1971; Hille,2001; Nosko & Roux, 2006). The work performed on prokaryotic K^+ channels has allowed researchers to gain a better understanding of how ion selectivity and permeability works, however, more complex voltage gated ion channels such as sodium and calcium have proven to be more complicated.

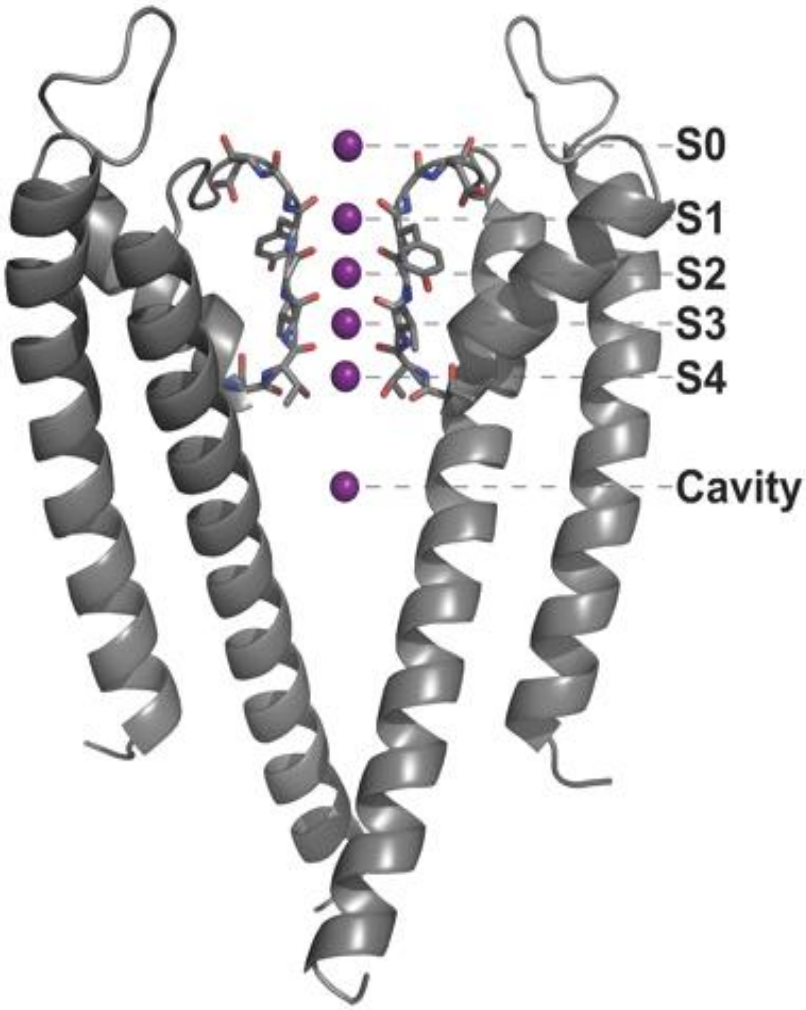

Figure 1.4 The pore structure of KcsA channel. A side view of a KcsA channel pore, showing only 2 out of 4 subunits.

There are five binding sites (S0-S4), S0 is located extracellularly and S1-S4 reside intracellularly. Potassium ions become dehydrated upon entering the pore from the inner cavity and bind to the carbonyl oxygen atoms of the selectivity filter. A traditional outward potassium ion migrates from the pore cavity 'transitioning from positions S1-S3 and S2-S4 binding sites as a dehydrated ion and then rehydrated at position S0 on the extracellular side of the channel pore. (Reproduced from Nimigean & Allen, 2011)

1.4.2 The pore configuration of calcium and sodium channels

An understanding of the probable common structure of the sodium and calcium channels was revealed in the X-ray crystal determination of the bacterial sodium channel, NavAb from *Arcobacter butzleri* (Payandeh et al. 2011). Compared to the long and narrow potassium selectivity filter of potassium channels, sodium and calcium channels likely have a much broader and shorter selectivity filter. The equivalent narrow construction point of the selectivity filter in Cav1 and Cav2 calcium channels is a glutamate residue contributed by each of the four domains DI,DII, DIII, DIV: (EEEE) which differs from the signature selectivity filter positions in classical Nav1 sodium channels (DEKA, aspartate-glutamate-lysine-alanine). Unlike potassium channels, the side chains of the pore selectivity filter face into the pore and contribute to the high selectivity of sodium and calcium channels (Payandeh et al. 2011). Mutations of the DEKA selectivity filter in sodium channels to EEEE of calcium channels generates a highly calcium select channel in a sodium channel (Heinemann et al. 1992; Schlief et al. 1996). L-type calcium channels with the EEEE selectivity filter can effectively selective for calcium over sodium ions at a 1000:1 ratio even though the diameters of L-type calcium channels and Nav1 sodium channels are nearly identical at 2 Å (Sather & McCleskey, 2003). Two mechanisms have emerged to explain the high selectivity of calcium channels; (1) calcium channels discriminate ions based on ion affinity and (2) ion flux through calcium channels is a multi-ion process.

Hypotheses surrounding ion binding in the pore comes from studies examining the relative permeability of differing ions. Hagiwara et al. (1974) demonstrated that cobalt blocks calcium currents more effectively than barium currents. Hagiwara and colleagues (1974) suggests the likely cause is that calcium can bind more tightly to the channel pore than barium, therefore, calcium permeates slower through the channel, providing a greater resistance against the blockage by cobalt ions. This was further supported by single channel recordings to investigate how rapidly an ion could pass through the pore. The overall unitary conductance values for calcium channels is $Ca^{2+} < Ba^{2+} < Li^{+} < Na^{+} < K^{+} < Cs^{+}$. These findings indicate that calcium ions pass through the pore at a much slower rate (Eisenman et al., 1967; Hess, Lansman & Tsien, 1986). The high binding affinity and slow rate of passage of calcium ion channels has been dubbed the “sticky pore” hypothesis. Ions that bind more tightly to the pore will have high selectivity but lower conductance (eg. calcium ions in calcium channels) whereas ions that bind

less tightly will have a low selectivity with high conductance (eg. sodium ions in a calcium channel pore) (Sather & McCleskey, 2003).

Observations from the anomalous mole fraction effect (AMFE) studies are consistent with the "sticky pore hypothesis". The AMFE studies reveal a classical "U" shaped dose response curve. At very low calcium concentrations, the inward current is large and is predominantly conducted by sodium ions. As calcium concentrations increase (10^{-6} M), the current sizes get smaller, indicating that calcium ions are binding with high affinity to the pore and are preventing sodium ions from flowing through. At calcium levels above physiological concentrations (10^{-2} M), the current will mostly be carried by calcium ions and begin to saturate. This saturation is seen as the maximum rate of binding- unbinding of calcium ions (Hille, 2001; Sather & McCleskey, 2006). It is thought that the carboxyl side chains of the EEEE locus protrude into the pore lumen to tightly bind a single Ca^{2+} ion at low calcium concentrations and to block sodium ions, while at high concentrations of calcium, carboxylate side chains will spatially rearrange themselves to accommodate for multiple calcium ions as shown in Figure 1.5A (Yang et al., 1993; Shuba, 2014).

Models were formulated to explain how calcium channels were highly sodium permeable in the absence of calcium ions, but were highly calcium selective and resistant to sodium permeation in the presence of calcium ions. Rate theory models have attempted to explain this behavior in HVA calcium channels. These two models are based on (1) ion-ion interactions and (2) a stair step mechanism (Dang & McCleskey, 1998).

A topological map illustrates potential binding sites and energy barriers that ions need to overcome in order to permeate through the pore. These diagrams are typically represented as valleys and hills, where the valleys are the binding sites and hills are the relative energy barriers, with the largest hill being the rate-limiting factor of ion movement, see Figure 1.5b (Dang & McCleskey, 1998). In the ion-ion interaction model, it is assumed that the pore has two identical high affinity binding sites. When only a single Ca^{2+} ion is bound, it struggles to escape because it does not have enough energy to overcome the energy barrier. However, when both binding sites are occupied, the energy barrier is reduced and electrostatic repulsion between the two ions promotes calcium flux (Sather & McCleskey, 2006; Shuba, 2014). A better theory for explaining multi-ion permeation behavior is a stair steps mechanism. The stair steps is represented by a single high affinity binding site flanked by two low affinity sites on each side of

it (Sather & McCleskey, 2006; Shuba, 2014). Based on this model, high calcium flux occurs when a calcium ion saturates the high affinity binding site. Calcium ions cannot occupy the same site at a time, so residual calcium ions overflow to low affinity sites. The lower energy barriers are easier to overcome in the lower affinity sites, leading to a rapid and highly calcium-selective ion flux once a calcium ion is saturated at the high affinity site (Dang & McCleskey, 1998; McCleskey, 1999).

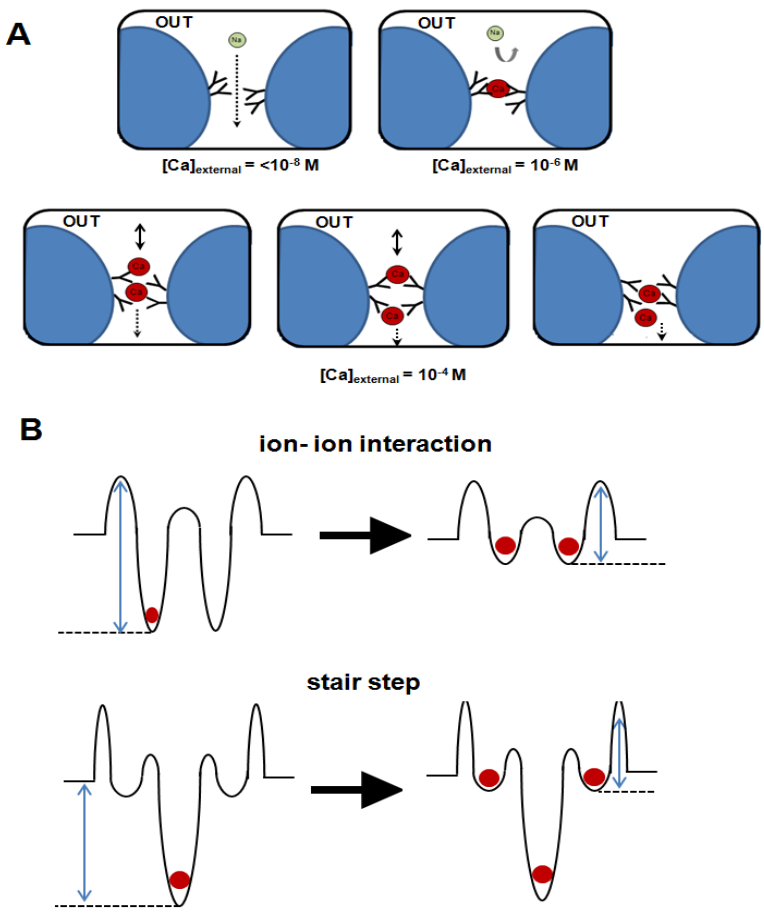

Figure 1.5 Various mechanisms and theories on ion selectivity and permeation in calcium channels.

(A) At low calcium concentrations (< 10^{-8} M), monovalent ions such as sodium can easily pass through, however once the concentration of calcium reaches 10^{-6} M, a calcium ion will bind to the high affinity binding site and prevent the passage of sodium ions. At higher levels of calcium concentrations, the glutamate residues will rearrange themselves to create multiple binding sites to allow the passing of calcium. (B) Two proposed mechanisms of ion permeation in a multi-ion pore based on rate theory. Calcium ions are depicted by red circles and the relative energy barrier needed to exit the binding site is represented by a double blue arrow. The ion- ion interaction states that there are two high affinity binding sites, when a single calcium ion enters, it cannot expend enough energy to get to the next binding site. However, when a second calcium ion is present, it reduces the energy barrier and causes an ion repulsion. The repulsion is enough force to allow the passage of ions through the pore. A stair step mechanism hypothesizes three binding sites, one high affinity site flanked by two low affinity sites. A calcium ion entering the pore will be drawn to the high affinity binding site but cannot leave due to the high energy barrier. Since two ions cannot occupy one site, the incoming ions will residue in the low affinity sites. The lower affinity sites require less energy to 'hop' over it, thus, allowing calcium ions to easily pass through the pore.

1.4.3 Less calcium selective T-type calcium channels

T-type channels are different than L-type calcium channels in being much less calcium selective. Normally in the presence of calcium ions at physiological (mM) levels, L-type calcium channels will not pass sodium ions, whereas, T-type channels will pass 20 to 40% of their current as sodium ions even in the presence of calcium ions at physiological (mM) levels (Senatore, Guan, & Spafford, 2014).

A major difference between T-type channels and the more calcium selective HVA L-type channels is the selectivity filter locus, containing EEDD (glutamate-glutamate- aspartate – aspartate) instead of EEEE of HVA channels. Since aspartate side chains are one methyl group shorter than glutamates, it is suggested that these residues were less favourable in stabilizing divalent cations, allowing for T-type channels more rapid calcium influx (Shuba, 2014). The consequences to mutations of the EEDD selectivity filter of Cav3.1 T-type channels to resemble the selectivity filter of L-type channels (EEDE, EEED and EEEE), generated calcium channels that were even less calcium selective (Talavera et al, 2001; Talavera et al., 2003; Park et al., 2013). The counterintuitive results indicate that the EEDD selectivity filter of T-type channels is not the only determinant responsible for the high sodium permeability of T-type channels.

Examinations of the anomalous mole fraction effect (AMFE) using calcium/sodium solutions showed a much weaker calcium selectivity for T-type channels. While calcium blocks sodium currents in HVA channels at 10^{-6} M, it takes a higher 10^{-4} M concentration of calcium to block the sodium current in T-type channels indicating that T-type channels have a reduced affinity for calcium binding and that they will accommodate both sodium and calcium ions at physiological levels (Shcheglovitov & Shuba, 2006; Shcheglovitov, Kostyul, & Shuba, 2007) .

1.5 T-type channels in biological systems and diseases

Calcium channels have both electrogenic and regulatory roles in biological systems. Activation of T-type channels through membrane depolarization can facilitate the generation of actions potentials demonstrating calcium's ability to act in an electrogenic process. Rises in internal calcium ions as a result of T-type channel activity activates calcium-dependent cell functions such as muscle contraction, hormonal secretion, gene expression and synaptic plasticity (Hille, 2001; Zamponi, 2005). T-type channels are abundantly expressed in the brain, heart, smooth muscle, sperm, kidneys and other endocrine organs (Perez-Reyes, 2003). The wide

tissue distribution of T-type channels suggest that they have a wide diversity of physiological roles. My discussion will be limited to the possible functions of T-type channels in the heart and the brain.

1.5.1 Cardiovascular system – the heart

The cardiovascular system supplies blood, nutrients and eliminates waste. The sino-atrial node is the primary pacemaker that generates the heart beat. Action potentials generate pacemaker currents, that spread through the atria to the atrioventricular node, delayed at the A-V bundle (Bundle of His) and then the excitation progresses to the right and left bundle branches of the right and left ventricles to the Purkinje fibers which excites the ventricles to promote a synchronous alternating contractions of the atria and the ventricles (Mullins, 1981; Langer, 1990). Action potentials spread along muscles into membrane invaginations deep within heart muscles (T-tubules) where L-type calcium channels are present in high density. The influx of calcium through L-type calcium channels, trigger the release of intracellular calcium through ryanodine receptors (RyR2) in the intracellular membranes of stored calcium in the sarcoplasmic reticulum which envelope heart muscle cells. T-type channels and hyperpolarization-activated cyclic nucleotide gated (HCN) channels are implicated in generating the pacemaker current in the sino-atrial node, that drives the heart beat and synchronous calcium release and contractions of heart muscle, see figure 1.6 (Mullins, 1981; Langer, 1990; Zamponi, 2005; Silverthorn, 2007; Grant, 2009).

Spontaneous and repetitive pacemaking occurs in cells when there is an absence of a stable resting membrane potential. After repolarization in phase 3 (generated by delayed rectifying potassium currents), the T-type channels and HCN channels are recruited, producing a rising baseline and depolarization during phase 4 that reaches threshold to generate an action potential spike (phase 0) carried by L-type calcium channels, see Figure 1.6 (Grant, 2009). Pacemaking currents are spread to other areas of the heart via the heart conduction system, and through gap junctions that connect between heart cells. The more rapid upstroke and conduction speed of the cardiac action potential outside the primary pacemaker, sino-atrial node (and atrioventricular node), is carried by rapidly activating Nav1 sodium channels, mostly Nav1.5 in mammalian cardiac cells (Langers, 1990; Silverthorn, 2007). Pacemaking currents in mammalian sino-atrial nodes have seven identifiable ion current types. These include the

sustained inward current (I_{st}), the delayed rectifier current (K_{ir}), the muscarinic potassium current, the sodium/potassium pump current, funny currents (I_f) controlled by hyperpolarization-activated cyclic nucleotide gated channel (HCN), and L- and T- type calcium channels (Zamponi, 2005; Grant, 2009; Ono & Iijima, 2010). Pacemakers set the rhythm and occur spontaneously without the aid of electrical stimulation, also known as autorhythmicity. T-type currents are found at a high density in pacemaker cells located in the sino-atrial node of the atrium in the heart, and not present outside of pacemaker cells of the heart, such as the ventricles. Although calcium channels act as an important second messenger, their role as a pacemaker is related to its voltage dependence (Hille, 2001; Vassort, Talavera, & Alvarez, 2006).

T-type currents are most abundant in the embryonic heart in both the atrial and ventricular chambers, and this current either becomes absent or significantly reduced in the ventricle after birth (Vassort, Talavera & Alavarez, 2006). Mouse studies demonstrated that mRNA levels of Cav3.2 is the predominant variant in the heart during early stages of fetal development (embryonic 9.5 days (E9.5)), that later gets down regulated, while mRNA levels of Cav 3.1 are up-regulated in later stages of fetal development (E18) (Cribbs et al, 1998; Cribbs et al, 2001; Larsen, Mitchell & Best, 2002). After birth, T-type channel expression continues to decline. T-type channels can be recorded from 8 day old mice but disappears by 3 weeks post-natal, even though the mRNA levels can still be measured for Cav3.1 and Cav3.2 channels (Ono & Iijima, 2010). There is a strong correlation between the size of the animal and T-type channel current density. Smaller animals have a higher heart rate and increase current density of T-type channels. As body size increases (mouse >guinea-pig>rabbit> pig), T-type channel density drops to levels where they are not readily detectible in the human sino-atrial node (Hart, 1994; Ouadid et al, 1991; Ono & Iijima, 2005).

T-type current density dramatically declines over the course of development but a spike in re-expression of these channels is associated with heart disease. Rises in T-type channel expression has been associated with cardiac arrhythmias, pressure overload cardiac hypertrophy and heart failure (Martinez, Heredia & Delgado, 1999; Nuss & Houser, 1993; Vassort, Valavera & Alvarez, 2006). It is proposed that the re-expression of T-type currents in ventricular hypertrophy is associated with Ca^{2+} overload (Huang, 2000). Abnormally high levels of T-type channel expression provide a continuous leak of calcium into heart cells through their window currents, which is expected to exacerbate heart disease (Bkaily, 1997). The only T-type channel

blocker that has been marketed was mibefradil, which was used to treat high blood pressure, angina (heart pain) and ischemia, especially in patients with congestive heart failure. Mibefradil was taken off the market because of side effects on drug metabolism in the liver (Levine et al., 2000). Current research in development of more specific T-type channel drugs have potential therapies for treating heart disease.

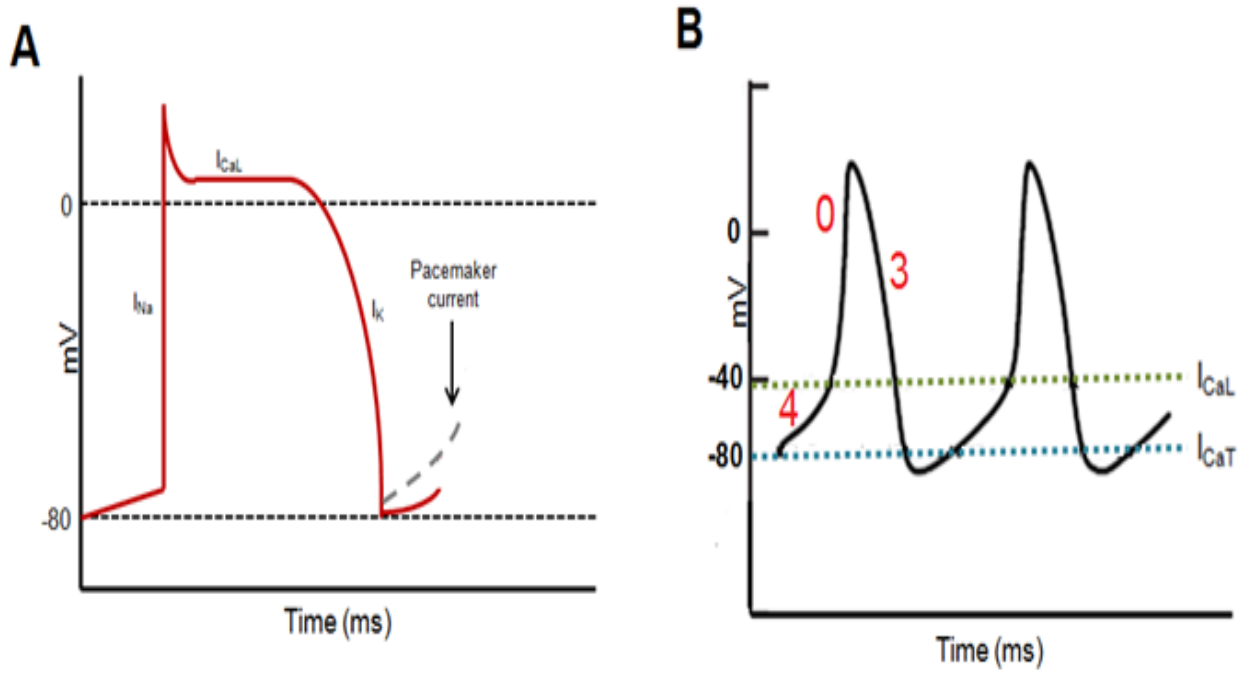

Figure 1.6 Cardiac and pacemaker action potentials.

(A) A cardiac action potential is initiated by a pacemaking current. The pacemaking current depolarizes the cell to activate voltage gated Na_v1 sodium channels. Strong depolarizations above threshold activates high voltage-activated L-Type calcium channels. The L-type calcium channel are delayed in opening because they are high voltage-activated, and have slower kinetics of opening compared to the faster sodium channels, as a result the L-type current contributes to the plateau in the cardiac action potential. The plateau is generated because of outward, delayed rectifying K^+ currents opposing the depolarization induced by the L-type calcium channels. Once repolarizing K^+ currents begin to dominate, the L-type calcium channels turn off, and membrane repolarization of the cardiac action potential is rapid. (B) The pacemaker current occurs in three stages, stage 4 is a diastolic depolarization, phase 0 is the upstroke and phase 3 is repolarization. Potassium channels repolarize in phase 3, it recruits HCN and T-type channels, which open upon strong membrane repolarization, and depolarize the membrane. The pacemaker current generated by HCN and T-type channels activates the L-type calcium channels at a high threshold to create phase 0. Potassium currents hyperpolarize the cells during phase 3.

1.5.2 Central nervous system – the brain

The highest levels of T-type channel expression in adult mammals is the thalamus. LVA T-type channels contribute to low-threshold calcium spikes (LTS), which have been described in the thalamocortical neurons but also other areas of the brain such as the thalamic relay nucleus inferior olive, and the hippocampus (Deschenes et al., 1984; Highasima, Kinoshita & Koshino, 1998; Llinas & Yarom, 1981). T-type channels are tonically inactivated in these cell types, so low threshold spikes are triggered by strong hyperpolarizations, which remove the T-type channel refractoriness. T-type channel activity triggers a burst of action potential spikes on a plateau (known as a rebound burst) carried by activated voltage gated Na_v1 sodium channels (Cheong & Shin, 2013; Perez-Reyes, 2003). Low threshold spikes in burst firing and rhythmic oscillations are observed in physiological states such as sleep (Lee, Kim & Shin, 2004; Steriade, 2005) and pathological conditions such as absence epilepsy (Cheong & Shin, 2013).

The phase of sleep which involves T-type channels is mainly during non-rapid eye movement (NREM) sleep. NREM sleep is divided into three stages slow waves (<1 Hz), delta waves (1-4 Hz) and sleep spindles (7-14 Hz). Delta waves originate from the thalamus, which is known to have a rhythmic pattern generated by T-type currents. Mice with the knockout gene, Cav 3.1 lacked the production of delta waves due to the loss of low threshold spikes and, this results in observable abnormalities in sleep behavior (Lee, Kim & Shin, 2004; Lee & Shin, 2007).

Absence epilepsy is associated with a brief loss of consciousness and marked by a 3 Hz-spike- wave discharge (SWD) on electroencephalography (EEG) recordings. During an epileptic episode, oscillations in the thalamcortical region often shift the firing pattern from tonic to bursting behavior and these sustained abnormal oscillations during the epileptic SWD are mediated by LTS (Kim et al., 2001). The involvement of T-type channels in epilepsy was first demonstrated by Kim and colleagues (2001), who showed that knockout mice of Cav3.1 channels both demolished the presence of LTS in the thalamocortical region and provided a resistant to absence epilepsy induced by agonists. On the other hand, overexpression of Cav 3.1 was sufficient to generate spontaneous SWDs in transgenic mice, that replicate a similar pattern of oscillations observed in absence epilepsy (Zhang et al, 2002). Mutations of Cav3.2 channels led to enhanced T-type channel activity has been found in a population of Chinese patients with childhood absence epilepsy (Vitko et al, 2005). Modeling suggests that the enhanced T-type

channel activity in these mutants contribute to a lower threshold for the generation of LTS, and asynchronous neural firing in the thalamocortical region is consistent with the output during an epileptic seizure. These gain-of-function mutations are clustered in the I-II linker, associated with enhanced membrane expression of T-type channel current density that would contribute to absence epilepsy (Vitko et al., 2007).

1.6 *Lymnaea stagnalis* Model

The Spafford lab has adopted an invertebrate model to study T-type calcium channels. *Lymnaea stagnalis* is a freshwater pond snail, that has accessible heart cells and brain neurons for culturing and physiological measurement using electrophysiology. It is also a simple model where there is only one Cav3 channel gene expressed in the snail (LCa_v3) versus three in mammals ($Ca_v3.1$, 3.2 and 3.3). Prior to starting this thesis work, initial characterizations of the snail T-type channel gene were completed (Senatore & Spafford, 2010). The full length cDNA of LCa_v3-12b is the largest known voltage-gated ion channel mRNA transcript ever identified, producing a >2.8 kB transcript. It is also the only known description of a T-type channel outside of the mammalian Cav3 channel isoforms. Preliminary expression of LCa_v3-12b reveals a T-type channel with typical features for T-type channels including a low threshold for activation, a window current at rest, rapid activation and inactivation kinetics, and slow deactivation (Senatore & Spafford, 2010).

More recently, Senatore and Spafford (2012) reported conserved exon splicing of exons 8b and 25c regions in the *Lymnaea* T-type channel (LCa_v3), which is conserved amongst particular mammalian Cav3 channels. Optional exon 8b is found in the I-II linker, upstream of the gating brake and has been shown to contribute to the total surface expression of the LCa_v3 channel protein (Senatore & Spafford, 2012). A 50 % reduction in surface expression is observed when this exon is present. These results parallel the findings from human Ca_v3 channels, where researchers have located alternatively spliced exon 8b in rat Cav3.1 channels that controls surface membrane expression in the same manner (Arias-Oluin et al., 2008; Baumgart et al., 2008). Exon 25c is located in the III-IV linker and has been shown to alter biophysical properties of LCa_v3 and a similar exon 25c regulates mammalian $Ca_v3.1$ and $Ca_v3.2$ channels (Senatore and Spafford 2012). LCa_v3 transcripts decline from embryonic to juvenile/adult life stage like their mammalian counterparts and is a gene that is abundantly

expressed in the brain and heart (Senatore & Spafford, 2012). The description of snail LCa_v3 provides a fundamental basis for further investigation of snail T-type channels.

1.7 Objectives & Hypothesis

There are two main focuses in my research, the first is an examination of ion permeability and selectivity in the T-type calcium channel isolated from the freshwater pond snail, *Lymnaea Stagnalis* (LCa_v3). The second focus is to examine the differences between snail LCav3 and mammalian T-type channels (hCa_v3). Dr. Adriano Senatore discovered novel alternative splicing in an extracellular turret region coded by exon 12 in LCa_v3. The two isoforms of LCa_v3 with alternative turrets are dubbed as exon 12a and 12b. Exon 12 is located in the pore of domain II between S5 and S6 transmembrane segments, just upstream of the selectivity filter. It is hypothesized that the location of exon 12 in the channel pore domain has potential associations with roles in regulating ion selectivity and permeability of LCa_v3 channels (Senatore et al., 2014). Based on the sequences of exon 12 the following hypotheses were made:

1. Alternative splicing of exon 12 would differ in their ion selectivity and permeability from their mammalian counterparts due to their differing turret sizes and conserved cysteine residues. Exon 12a contains a tri-cysteine motif, while 12b and hCa_v3 channels contain a penta- and uni- cysteine(s) in their turret respectively.
2. Senatore & Spafford (2012) found that LCa_v3 with exon 12a but not exon 12b is expressed in cardiomyocytes. It is hypothesized that snail T-type channel currents in snail heart cells would exhibit the expression of *in vitro* expressed features of the LCa_v3-12a gene isoform in recombinant heterologous cells.
3. In addition, it is hypothesized that highly conserved cysteine residues in the turret are responsible for calcium selectivity in mammalian T-type channels. Cysteine substitution to alanines within exon 12a and exon 12b turrets were created to mimic the uni-cysteine framework of mammalian hCa_v3 channels to generate a calcium selective snail T-type channel, out of a more sodium permeable one.
4. Finally, substituting the snail exon 12 with the corresponding region from mammalian Ca_v 3.2 (α1H) into LCa_v3 (generating LCa_v3-α1H), is expected to confer mammalian $Ca_v3.2$ ion selectivity and permeation characteristics onto the snail LCa_v3 T-type channel.

The objective of this research project focuses on 1) characterizing T-type calcium channel isoforms with novel extracellular turrets in domain II in LCa_v3 2) investigating the features of T-type channels expressed *in vitro* from *Lymnaea* cardiomyocytes 3) Comparing and contrasting the differences and similarities in LCa_v3 and the three mammalian hCa_v3 channel genes. This research was conducted by utilizing the following methods 1) prepping DNA plasmid for transfection and performing electrophysiological recordings on snail and mammalian T-type channels 2) maintaining, culturing and expressing T-type channels in human embryonic kidney cells (HEK293T) and 3) developing a protocol to culture snail ventricular myocytes. Transfected T-type calcium channels in HEK293T cells and snail ventricular cardiomyocytes were recorded using the whole cell patch clamp technique. The electrophysiological data collected is subtracted for leak currents, and analyzed and T-type channels are measured for their biophysical properties, ion selectivity, permeability and drug sensitivities.

Dr. Adriano Senatore and Dr. David Spafford performed sequence alignments from available genomes of species in the animal kingdom to gain insight into the evolutionary origins of T-type calcium channels and how invertebrates have diverged from their vertebrate counterparts in ion selectivity and permeation properties. We sought to understand the physiological relevance behind the need for alternative splicing in exon 12 in invertebrates. As a result, I modified a primary culture protocol to isolate *Lymnaea* cardiomyocytes to record their basic kinetics, drug sensitivity and ion permeation/selectivity and compared these features to recombinant T-type channel genes expressed *in vitro*. The discovery of significant differences in ion selectivity and permeation between the snail LCa_v3 channels with differing exons (12a or 12b) and the vertebrate hCa_v3 channels led to the speculation of highly conserved cysteines and differing turrets sizes and their potential role. A fourth year undergraduate student (Robert Stephens) working in the Spafford laboratory constructed three turret mutants in LCav3 channels. Mutants were created with cysteine substitution to a neutral amino acid alanine, to transform exon 12a with three cysteines and exon 12b with five cysteine to ones reduced down to one cysteine, which we dub as LCa_v3-12a ΔC and LCa_v3-12b ΔC respectively. We also replaced the snail exon 12 with the corresponding region from human $Ca_v3.2$, this generated a construct known as LCav3-α1H. The production of these chimeric and mutagenized channels from snails were compared to their original counterpart channels and the expression of the three human Cav3

homologs. The overall goal of this research aimed to create a comprehensive structural model of how variations in the T-type channel pore altered functions of ion permeability and selectivity.

Chapter 2
Materials & Methods

2.1 General cloning methods

The snail LCa_v3 calcium channels presented in this thesis were cloned by Dr. Adriano Senatore (Senatore & Spafford, 2010) and the mutations of LCa_v3 calcium channels were carried out by Robert Stephens, a fourth year undergraduate project student in the Spafford laboratory. Human $Ca_v1.2$, $Ca_v3.1$, Cav3.2 and $Ca_v3.3$ calcium channels as well as rat calcium channel β_{1b} and $\alpha_2\Delta$ subunits were a gift to the Spafford laboratory from Edward Perez-Reyes (University of Virginia) or Gerald Zamponi (University of Calgary) and *Lymnaea* L-type channels (LCa_v1) cloned by Dr. J. David Spafford (Spafford et al. 2006).

2.1.1 Preparing electrocompetent E. coli Copycutter

Ion channel subunits in bacterial plasmids were transformed by electroporation and grown as bacterial cultures and then purified in a plasmid maxi- preparation. Electroporation was carried out with prepared electrocompetent cells. Electrocompetent CopyCutter™ cells (Epicenter Biotechnologies, #C400EL10) were streaked onto a Luria Bertani (LB) agar plate without antibiotics and incubated at 37°C overnight. The next day, a single bacterial colony was inoculated into 250 mL of Super Broth (SB) without antibiotic into a 37°C shaking incubator spun at 300 rpm until an optical bacterial density was reached that measured in the spectrophotometer at 600 nm (OD_{600}),or until 0.3-0.6 was reached on the nanodrop. Cells were then chilled on ice for 20 minutes and transferred to a cold centrifuge bottle and spun down at 4000 g for 15 minutes in a 4°C centrifuge (Beckman Coulter Allegra 25R). The supernatant is discarded and the pellet was re-suspended in 250 mL of ice cold 10% (v/v) glycerol (Fischer Scientific, #56-81-5) and centrifuged for 4000g for 15 minutes at 4°C. This wash step was repeated again. Afterwards, the supernatant was discarded and cells were re-suspended in 20 mL of ice cold 10% glycerol and transferred to a 50 mL falcon tube, where it was centrifuged at 4000g for 15 minutes at 4°C. Once again, the supernatant was removed and the cells were re-suspended in a final volume of 1-2 mL of ice cold 10% glycerol for a total cell concentration of 1-3 $x10^{10}$ cells/mL. Cells were then aliquoted into microcentrifuge tubes, 25 µL per tube and stored in a -80°C freezer until use.

2.1.2 Bacterial transformations

Two types of *E.coli* derivatives were used for bacterial transformations, chemically competent Stbl2 cells (Invitrogen, #10268-019) and electrocompetent CopyCutter™ cells. Splice isoforms of LCa_v3 channels were transformed using electrocompetent CopyCutter™ cells. 1 µL of plasmid was mixed into a 1.5 mL micro centrifuge tube with 20 µL of thawed electrocompetent CopyCutter™ cells, and placed on ice for 5-10 minutes. The mixture was then pipetted into a pre-chilled 90µL electroporation cuvette (VWR, #89047-206) and electroporated at 1200 mV using an Eppendor Electroporator 2510. 1 mL of Super Broth (SB) media without antibiotics was mixed with the cells and transferred to a new 1.5 mL centrifugation tube and incubated for 1 hour in a 37°C shaking incubator, rotating at 350 rpm. Afterwards, the microcentrifuge tube was spun at 4000 rcf for 2.5 minutes at room temperature. 900 µL of the supernatant was removed, and the remaining 100 µL of supernatant was used to re-suspend the cells and plated onto a LB agar plate containing 50 µg/mL of Kanamycin (OmniPur, #5880). Plates were inverted and placed into a 37°C incubator for 30-36 hours for growth, afterwards isolated colonies were inoculated.

All human Ca_v3 channels (Ca_v 3.1, 3.2 and 3.3) underwent a heat shock bacterial transformation using chemically competent Stbl2 cells. 50 µL of thawed chemically competent Stbl2 cells were pipetted and mixed with 1-3 µL of plasmid into a 0.2 mL micro centrifuge tube and placed on ice for 5-10 minutes. Cells were then heat shocked for 30 seconds at 42°C (MJ Research PTC-200 Peltier Thermal cycle) and incubated on ice for 1 minute afterwards. Then the mixture was pipetted and mixed into a 1.5mL centrifuge tube containing 1 mL of SB media without antibiotic and incubated for 1 hour in a 30°C shaking incubator at 350 rpm. The tube was then centrifuged at 4000 rcf for 2.5 minutes at room temperature and 900 µL of supernatant was removed. The remaining 100 µL of supernatant was used to re-suspend the cells and they were plated onto a LB agar plate containing 100 µg/mL of Ampicillin (OmniPur, #2200). Plates spread with bacteria were left inverted in a 30°C incubator overnight.

2.1.3 Culturing bacteria for plasmid isolation

Large quantities of plasmids were prepared with the maxi-prep method. Single pinprick sized colonies that grew within 30-36 hours after bacterial transformation on the agar plate using electroporation were chosen and inoculated into 250 mL of SB media containing 50 µg/mL of

Kanamycin and grew for ~36 hours in a 37°C shaking incubator at 350 rpm. Heat shocked plasmids were inoculated after ~16-20 hours of growth into 250 mL of SB containing 100 µg/mL of Ampicillin from a single bacterial colony and were grown overnight in a 30°C shaking incubator at 300 rpm.

Once the bacterial culture reached its optimal cell density, the cells were transferred to a 250 mL centrifuge and spun down at 4500 rcf for 10 minutes at 4°C. The supernatant was discarded into bleach and the cells were re-suspended in a mixture of 6 mL glucose-Tris-EDTA (50 mM glucose, 25 mM Tris-HCl, pH 8.0 and 10 mM EDTA, pH 8.0).12 mL of a lysis buffer containing 1% (v/v) sodium dodecyl sulfate (SDS) and 0.2M sodium hydroxide (NaOH) was added to the centrifuge tube and the tube was gently rotated to lyse the bacterial cells and placed on ice. Then 9 mL of an ice cold solution containing 3M potassium acetate (KoAC) and 11.45% (v/v) of glacial acetic acid was added to the centrifuge tube and the tube was inverted and rocked a couple times until a flocculent white precipitate formed. Then the centrifuge tube was spun down at 7000 rcf for 10 minutes at 4°C to pellet the precipitate. The supernatant was transferred to a 50 mL Falcon tube containing 16.2 mL of 2-propanol, then the sample was vortexed and left in a 4°C fridge overnight to allow for DNA to precipitate for maximal yield. The tube was spun at 9000 rcf for 10 minutes at 4°C to isolate the DNA pellet and the supernatant was discarded.

Next, 3 mL of Milli-Q-water was added to re-suspend the pellet and 3mL of ice cold 5M lithium chloride (LiCl) was pipetted in and vortexed, and then left on ice for 20 minutes before being spun down at 9000 rcf for 16 minutes. The supernatant was then transferred to a 15 mL centrifuge tube (Cell star, #188-271) with 7mL of 2-propanol and mixed, then left overnight in a 4°C fridge. Afterwards, the centrifuge tube was centrifuged at 7000 rcf for 12 minutes at 4°C and the supernatant was removed while the pellet was dissolved in 400µL of Milli-Q-water and transferred to a 1.5 mL microtube. 1 µL of 20 mg/mL of RNAse A (Sigma, #R4875) was pipetted into the tube and vortexed, then incubated at 37°C for 3-4 hours.

The final treatment to purify plasmid DNA was to remove any remaining protein. This was done by adding 400 µL of 50:50 phenol/chloroform mixture and vortexed for 5 seconds and spun at maximum speed for 4 minutes at room temperature to separate two different phases. The upper aqueous layer was transferred to a new 1.5 mL micro centrifuge tube and the phenol/chloroform step was repeated until there was no more white precipitate visible between the phases. Lastly, 400 µL of pure chloroform was added, vortexed and centrifuged at maximum

speed for 4 minutes at room temperature, and then the supernatant was transferred to a new centrifuge tube.

Subsequently, 21µL of 10M ammonium acetate was pipetted in, along with 840 µL of 100% ethanol and vortexed. The centrifuge tube was then incubated on ice for 3-4 hours to allow for plasmid DNA precipitation, then the tube was spun down at maximum speed for 10 minutes at 4°C. The supernatant was removed and the pellet was washed with 500 µL of 70% ethanol, vortexed and spun at maximum speed for 5 minutes at 4°C. This wash step was repeated twice. Finally, the pellet was re-suspended in sterile Milli-Q-water. The volume of the final DNA solution depended on the size of the pellet but typically ranges between 100-500 µL. A Nanodrop (Thermo Scientific, Nanodrop 1000 Spectrophometer) was used to assess DNA concentrations and purify the DNA using an absorbance reading at $A_{260/280}$. Sterile Milli-Q-water was added to adjust the DNA concentration, a final concentration ~1µg/mL was obtained and stored in a -20°C freezer until use.

2.1.4 Restriction digests

Restriction enzymes were obtained from New England Biolabs (NEB) and used to digest plasmid DNA as a diagnostic tool to determine whether or not the correct plasmid was properly grown. Typically 1 unit of restriction enzyme was used to digest 1 µg of DNA. All reactions were carried out in a 1.5 mL microcentrifuge tube incubated at 37°C; to check the sequence of ion channels, mixtures were incubated for 1.5 hours. An uncut plasmid was always run in parallel with each restriction digest serving as a diagnostic control sample.

All full length variants of LCa_v3were digested in 3µL of 10x NEB buffer 3(#B7003), 3µL of 10x bovine serum albumin (BSA) (#B9001), 1µL Bgl II (#R0144), 1µL BamHI –HF (#R3136), 1µL SalI-HF (#R3138) and 1µL of plasmid. A total volume of 30 µL was used for this reaction, the remaining volume was filled by water. The expected bands consisted of ~2500 bp, 4300 bp and 6400 bp for LCav3 lacking exon 8b. With LCav3 variants with exon 8b present, four expected band sizes should occur, 6453 bp, 4349 bp, 2168 bp and 930 bp.

Human $Ca_v3.1$ was digested with 1µL of 10x NEB buffer 4 (#B7004), 1µL of 10x BSA, 1µL of SalI-HF, 1 µL of plasmid and 6µL of water, for a total reaction volume of 10 µL. Expected band sizes include ~7600bp, 3300 bp and 1200 bp.

Human $Ca_v3.2$ was carried out in 1µL of 10x NEB buffer 3, 1µL of 10x BSA, 1µL of EcoRV (#R0915), 1 µL of plasmid and 6µL of water, for a total reaction volume of 10 µL. The present reaction should produce band sizes of ~ 8800 bp and 4300 bp.

Finally, $Ca_v3.3$ was carried out in 1µL of 10x NEB buffer 4, 1µL of 10x BSA, 1µL of BamHI-HF, 1 µL of plasmid and 6µL of water, for a total reaction volume of 10 µL. This should result in band sizes of ~7500 bp, 5000 bp and 640 bp.

Once restriction digest reactions were completed, each mixture had a 6x loading dye pipetted in, the volume added varied depending on the total reaction volume. Each mixture was loaded onto a 1% (w/v) agarose gel containing 75 mL of Tris-acetate buffer, 0.75g of agarose (BioShop, #AGA001-250) and ethidium bromide (EtBr) and ran on a Bio-rad Power Pac200 set at 100 mV for 1 hour. Gel bands were illuminated with a UV light source on an Alpha Innotech AlphaImager HP gel documentation system.

2.2 Primary tissue culture of *Lymnaea* ventricular myocytes

Animals were kept on a 12 hour light-dark cycle at 22 ± 2 °C fed Romaine lettuce once a week as well as fish pellets (Nutrafin max) twice a week. They were raised at University of Waterloo.

The age of hatched snails and their sexual maturity was determined by their shell length as described by McComb, Varshney, & Lukowiak, K. (2005). Juvenile *Lymnaea* have shell lengths less than 15 mm and they reach adulthood at 20 mm. Ventricular cardiomyocytes were taken from juvenile snails with a shell length between 10-15mm, while adults had a shell length between 20- 25 mm. The original protocol for culturing *Lymnaea* cardiomyocytes was adapted from Gardner & Brezden (1990) with some modifications.

2.2.1 Dissection of the *Lymnaea* ventricle

Four to six adult snails were typically dissected for extraction of hearts. Snails were de-shelled with Vannas spring scissors (Fine Sciences, #15018-10) and anesthetized in 10% (v/v) Listerine for 10 minutes. The dissection and dissociation of snail hearts took place in a sterile environment, using a laminar flow work station. Tools and the work station were sprayed with 70% ethanol before animal surgery. The *Lymnaea* snails were placed in tank water mixed with Listerine and pinned down with Austerliz insect pins (0.22 mm, #S44-020) and the heart ventricle was extracted using a Carl Zeiss SteREO Discovery V8 microscope, cut up into smaller

pieces using Vannas spring scissors and placed in 0.5 mM Ca^{2+} Leibovitz media (Gibco, Formula No. 82-5154EB) supplemented with 500 μg/mL of the antibiotic, gentamicin sulfate (Sigma, #G3632).

2.2.2 Dissociation of ventricular cardiomyocytes

Ventricles cut up into small pieces, were treated with trypsin to isolate the cardiomyocytes. The heart pieces were placed in a 15 mL centrifuge tube (Cell Star, #188-271) with 0.5 mM Ca^{2+} Leibowitz media containing 0.25% Trypsin (Sigma, #T9201) and 500 μg/mL of gentamicin sulfate for 12 minutes onto a rocking platform (VWR rocking platform, model 200). The cells were spun down at 700 rpm (Hettich Zentrifugen Rotofix 32A) for 3 minutes, and the media was aspirated and replaced with 0.1% Type II collagenase (Sigma, C6885) in 0.5 mM Ca^{2+} Leibovwitz containing gentamicin sulfate. Collagenase treated heart cells were incubated for 35 minutes on the rocking platform. The media was then spun down at 700 rpm for 3 minutes and aspirated then replaced with 3.5 mM Ca2+ Leibovwitz supplemented with 2% (v/v) fetal bovine serum (FBS; Sigma, F105) and 500 μg/mL of genatmicin sulfate; the combination of high calcium and FBS was used to inactivate any remaining collagenase and trypsin. Cells were washed three times with 3.5 mM Ca^{2+} Leibovwitz and the isolated cardiomyocytes were re-suspended in a final volume of 6 mL in this media.

2.2.3 Plating cardiomyocytes for electrophysiological recordings

Circular glass coverslips (Fischer Scientific, Circles No.1 – 0.13to 0.17 mm thick, size: 12mm, #12-545-80) were treated with hydrochloric acid (HCl) and sodium carbonate (Na_2CO_3). Eight to ten coverslips were placed in a 60 mm petri dish (Corning Life Sciences, #430166), and 6 mL of 3% HCl was added to the dish. Acid etching of the coverslips was carried out for 30 minutes and was then aspirated and then 6 mL of neutralization solution 0.1% (w/v) Na_2CO_3 was added for 30 minutes. Afterwards, the Na_2CO_3 was aspirated and the coverslips were left to dry in a 50°C oven for 2-4 hours. The coverslips were kept in a 4°C fridge until use.

Once the cardiomyocytes were ready to be plated, the acid etched coverslips were transferred to a sterile 60 mm petri dish (Corning Life Sciences, #430166), and 3 mL of cells and 3mL of fresh 3.5 mM Ca2+ Leibovitz media was added to the dishes and left at room temperature for 24 hours before electrophysiological recordings took place. Spontaneous

contractions could be observed 24 hours later, which was an indicator of viable and healthy heart muscle cells.

2.3 Mammalian cell culture

Human embryonic kidney cells (HEK293T) cells were cultured in Dulbecco's modified Eagle's medium (DMEM) (Sigma, D5796) supplemented with heat-inactivated 10% fetal bovine serum (FBS; Sigma, F1051), 1% sodium pyruvate (Sigma, S8636) and 250 µg/mL of penicillin/streptomycin (Sigma, P4458). Media was pre- warmed in a 37°C water bath prior to use. All manipulations of HEK293T cells were performed under a laminar flow hood. Fetal bovine serum was heat-inactivated by a 56°C water bath incubation period of 30 minutes.

2.3.1 Thawing HEK cells

HEK293T cells (obtained from ATCC) were stored in aliquots, frozen in liquid nitrogen for long term storage. A new batch of HEK-293T cells were used after 30 to 40 passages. One aliquot of stored HEK293T cells in liquid nitrogen were thawed in a 37°C water bath rapidly. 1 mL of pre-warmed media was mixed with the cells and placed in 5 mL of warm media in a 50mL, 25 cm^2 tissue culture flask (Cell Star, #690-170). Afterwards, cells were incubated in a 37°C CO_2 incubator for 3-4 hours to adhere cells. The media was then replaced with 6 mL of fresh warm media and placed back into the 37°C CO_2 incubator until fully confluent.

2.3.2 Cell culturing

The original protocol for HEK cell culturing and transfections was adapted from Senatore et al. (2011), although some modifications were made. Cells were split bi-weekly from a monolayer that was ~90-100% confluency, to a 1:8 dilution on Monday and a 1:12 dilution on Thursday. To split the HEK-293T cells media was aspirated and 1 mL of 0.25% Trypsin (Sigma, T4049) solution was added. The flask was inverted and gently rocked by hand to help de-attach the cells from the flask surface. Then the trypsin was removed and 500 µL of trypsin was applied directly onto the cells and the flask is incubated at 37°C, CO_2 incubator for 2-3 minutes. Afterwards, 6 mL of media is pipetted into the flask to inactivate the trypsin, and the cells were re-suspended and mixed by pipetting up and down ~10 times. Different ratios of cells to fresh media were added into a new flask. A 1:4 split from a confluent flask is carried out 4 hours prior to a transfection to allow for cell attachment.

2.3.3 Transfections of recombinant ion channels cDNAs

A standard calcium phosphate protocol was used for transfections. Typically 1μg/mL of the ion channel plasmid construct was introduced into HEK cells, for a total of 6μg of DNA in 600 μL of transfection solution in each flask. For a co-transfection of multiple ion channels, a total of 20μg of DNA was used. Each transfection requires two 1.5 mL sterile micro centrifuge tube, one containing buffer and the other containing calcium ions. The DNA was added to the tube containing calcium ions along with 30 μL of 2.5M $CaCl_2$, and Milli-Q –water for a total volume of 300 μL. The other tube contained 300 μL of HEPES-buffer saline (HES) solution. The calcium ion mixture was added to the HES tube drop wise then calcium phosphate crystals were facilitated by blowing bubbles with a pipette into the tube 5 times and finally pipetting the solution to mix 5 times. The microcentrifuge tube containing the calcium phosphate treated plasmids were left to incubate for 20 minutes before being added in a dropwise zigzag motion into the flask and then the flask containing media was left overnight in a 37°C CO_2 incubator.

The next day, the transfected flask was washed three times with warm media to remove the calcium phosphate solution, which is toxic to the cells. Old media was aspirated and replaced with 6 mL of fresh warm media onto an inverted flask. The flask was then slowly turned over and rocked gently over the attached cells and then the media was removed. Washing the cells with media was conducted an additional two times and placed back into the 37°C CO_2 incubator for 2-4 hours then transferred to a 28°C CO_2 incubator for several days. The use of 28°C was a temperature which facilitated the heterologous expression of the ion channel proteins, and limited the cell division of HEK293T cells. The time duration for incubation at 28°C depended on the efficiency of expression of ion channels. Typically snail LCa_v3 and human $Ca_v3.3$ was ready to record two days after transfection. Human Ca_v 3.1 and 3.2 and co-transfections of Ca_v3 channels with Ca_v1 channels required 6 days of incubation at 28°C before adequate expression was achieved for electrophysiological recording. Successful transfections was confirmed using an epifluorescence microscope since all ion channels were contained in a bicystronic vector pIRES2-EGFP which expressed green fluorescent protein (eGFP) from the same mRNA as the ion channel contained within the multiple cloning site of the vector. Cells emitting a green fluorescence when exposed under mercury lamp illumination light were an indicator of positive transfection of the ion channels.

2.3.4 Plating transfected HEK cells for electrophysiological recordings

One hour prior to recording, transfected HEK cells were de-attached from the flask by trypsinization. The same trypsinization procedure was used as cell culturing. However, after the 37°C incubation, the cells were re-suspended in 10 mL of fresh media and plated onto uncoated circular glass coverslips (Fischer Scientific, Circles No.1 – 0.13to 0.17 mm thick, size: 12mm, #12-545-80). Coverslips were placed in a 60 mm petri dish (Corning Life Sciences, #430166), 2.5 mL of fresh media and 2.5 mL of cells was added to each dish. Petri dishes were then placed in a 37°C CO_2 incubator for one hour, this will allow the cells to recover from trypsinization and attach to the coverslips.

2.4 Electrophysiology recordings

Coverslips containing attached cells were removed from the DMEM media contained in the 60 mm petri dishes prior to recordings, The coverslips were lifted by tweezers into 35 mm petri dishes (Falcon, #3109617) filled with external bath solution for electrophysiological recording. The ground electrode contained 1.25% agarose in 3M cesium chloride (CsCl) filled with 3M CsCl. Pipettes were pulled prior to recordings with a Sutter P-1000 or P-97 micropipette puller containing a trough-shaped platinum filament for HEK293T cells or a box-shaped platinum filament for cardiomyocytes. An outer diameter of 1.5 mm and an inner diameter of 0.86 mm borosilicate capillary glass containing filament were used for pulling pipettes (Sutter Instruments, #BF150-86-15). Each pipette was fire polished with a microforge (Narishige, #MF-830).

Whole cell patch clamp recordings were performed in both cardiomyocytes and HEK cells at room temperature. Recordings were obtained using an Axopatch 200B amplifier, sampled through a Digidata 1440a A/D converter to a PC computer. The pipette resistance for cardiomyocytes were set between 4-10 MΩ, while pipette resistances for HEK mammalian cell line recording were maintained between 2-5 MΩ. Only cells with a typical access resistance of <10 MΩ, recordings with minimal leak (<10%) and small current sizes (<1nA) were used for analysis. For all recordings, offline leak subtraction was carried out and data was filtered using a 500 Hz Gaussian filter in Clampfit 10.2. Microsoft Excel, SPSS, and Origin 9.0 were also used to handle and analyze the data.

2.5 Electrophysiological analysis and solutions

2.5.1 Characterization of basic kinetics in all T-type channels in HEK293T

Solution

The external recording solution for patch clamp recording were matched close to physiological levels for cardiomyocytes and neurons, and was used to collect data on the biophysical properties of calcium channels such as their activation, steady state inactivation, recovery from inactivation and deactivation. External recording solution consisted of 2mM $CaCl_2$, 160 mM tetraethylammonium chloride (TEA-Cl) and 10 mM 4-(2-hydroxyethyl)-1-piperazineethanesulfonic acid (HEPES), pH to 7.4 with TEA-OH.

Internal recording solution within the recording pipette for all the experiments (unless otherwise stated) contained 110 mM CsCl, 10 mM HEPES, 10mM ethylene glycol tetraacetic acid (EGTA) 3 mM MgATP and 0.6 mM LiGTP (pH to 7.2 with CsOH). Recording solution was filtered through a Nalgene 0.2 μm cellulose acetate syringe filter prior to use (Nalgene, #171).

Activation and IV curves

A step protocol starting from a holding potential of -110mV (below resting membrane potential), to a wide range of voltages in 5 mV incremental steps from -100 mV to +80 mV, was used to evaluate voltage-dependent responses of calcium channels. The raw data was transformed into a current-voltage (IV) curve by taking the raw peak current sizes at each given stepped voltage and normalized using the equation I/I_{max}, where I refers to the current in picoamps (pA) and I_{max} represented the maximum current. From each IV curve, the reversal potential (E_{rev}) was calculated to measure at what voltage the overall net flow of ionic current is zero. The linear portion of the IV curve was calculated to determine the slope (m) and y-intercept (b) using the equation y=mx +b and the E_{rev} was determined at the abcissa when y = 0.

The whole cell conductance is the rate of ions flowing across the membrane, and was determined by the following equation:

$$g = I /(V_{command}-E_{rev})$$

Where, g is the conductance value, I refers to the current at a given voltage step and $V_{command}$ is the command voltage membrane potential. The conductance was then normalized using $g/g_{max,}$ where g_{max} refers to the maximum conductance in a given set of voltages. Next, each cell recording was fitted to the Boltzmann equation:

$$activation\ curve = \frac{g}{g_{max}} = \frac{1}{\left(1 + e^{\frac{\left(-V_{command} - V_{\frac{1}{2}}\right)}{K}}\right)}$$

$V_{1/2}$ represents half-maximal activation, while k is the slope of the activation curve.

Using the same data file, the time to peak (ms) and tau inactivation (τ_{inact}) can be determined. The time to peak is the amount of time it takes for the average channel in a patch to reach its peak current at a given voltage step. This calculation involves subtracting the time point at which the current maximal peak from the time point after the capacitance transient occurs which represents the onset of the step depolarization. The τ_{inact} measures the time it takes for the average ion channel to inactivate ~2/3 of its channels. Inactivation is denoted by the decay in current after its peak. To obtain tau, the following standard exponential equation is used to measure the decaying portion of the current:

$$f(x) = \sum_{i=1}^{n} A_i\, e^{-t/\tau_i} + C$$

Steady state inactivation

The steady-state inactivation protocol involves a step depolarization to various potentials (known as a prepulse), held for 10 seconds to generate a steady-state fraction of channels that migrate from the open to the inactivated state. Following the inactivating prepulse, the cell is tested immediately at a step depolarization to peak current, to measure the percent reduction in maximal currents from open, available channels as a result of the increasing number of refractory channels in the inactivation state with greater depolarizing prepulses.

Calculations of the steady-state inactivation fraction of the maximal current I/I_{max} divided by the voltage of pre pulse potential. The fraction of maximal currents generated from the steady state inactivating prepulse was fitted with the Boltzmann equation:

$$h_{\infty}(V) = \frac{1}{\left(1 + e^{\frac{\left(V_{command} - V_{\frac{1}{2}}\right)}{K}}\right)}$$

$V_{1/2}$ represents half-maximal activation, while k is the slope of the inactivation curve.

Recovery from inactivation

Recovery from inactivation measures the time it takes for the average ion channel to recover from a state of maximal inactivation (or refractoriness). The recorded cell is subjected to a depolarization step to peak current (first pulse) that maximally opens and inactivates ion channels. Then different wait times are provided before the cell is subject to a step depolarization back to its peak current (second pulse). The time points between the two pulses were (in ms) 10, 50, 125, 250, 500, 750, 1000, 1250, 1875, 2500, 3750, 5000, 6250, 7500, 10 000, 12 500, 15 000, 17 500, 20 000 and 30 000 ms. During the waiting period between pulses, the ion channels recover from inactivation, and the fraction of maximally recovered current for each wait time can be measured as the percentage of the maximal current recovered was at the second pulse compared to the first pulse.

Deactivation

Deactivation refers to the measurement of the rate of ion channel closure from their open state. In the deactivation protocol, the cell is subject to a step depolarization to generate its peak current. which will maximally open channels. Once maximally opened, the cell is subjected to a range of hyperpolarizing steps to differing potentials before any significant inactivation takes place. Because of the increase in driving force with steps to lower potentials, a "tail" current is visible. The measurement of the decay of the tail current at differing hyperpolarized potentials is the rate of the channels migrating from the open to the closed state. The tau values from the decay of the tail currents are measured by a standard exponential equation:

$$f(x) = \sum_{i=1}^{n} A_i \, e^{-t/\tau_i} + C$$

Ca^{2+} vs. Ba^{2+}

2 mM Ca^{2+} and Ba^{2+} were used to examine the effects of similar sized divalent ions in the pore. Ba^{2+} differs from Ca^{2+} because it mimics calcium in the pore, but does not activate Ca^{2+}-dependent regulatory mechanisms. The external solutions containing either barium or calcium as the charge carrier were loaded into a Valvelink 8.2 Telfon perfusion system and a step protocol was used for each solution on the same cell.

2.5.2 Investigating ion selectivity and permeability in Ca_v3 channels in HEK 293T

Bi-ionic reversal potentials

A family of voltage steps generating current-voltage curves used for measuring activation was applied to the bi-ionic reversal experiment. The purpose of the bi-ionic reversal experiment was to measure the relative permeability of an inward calcium current (with 2 mM external calcium), compared to the relative permeability of outward monovalent ions (with 100 mM external monovalent ion). The more permeable the monovalent ions are compared to the calcium ions, the larger the outward monovalent ion current compared to the inward calcium current. Also the reversal potential would reflect the reversal potential of the outward monovalent ion if it is much more permeable than the inward calcium current.
Four different monovalent ions were tested, lithium (Li^+), sodium (Na^+), potassium (K^+) and cesium (Cs^+). See Table 1 for a list of internal and external solutions.

Permeability ratios were calculated based on the following equation:

$$\frac{P_{Ca}}{P_x} = \frac{[X]_i}{4[Ca]_o} \exp(E_{rev}\, F/RT)\,\{\exp\left(\frac{E_{rev}F}{RT}\right) + 1\}$$

Where [X] is the concentration of the monovalent ion, [Ca] is the concentration for calcium, E_{rev} is the reversal potential, F is the Faraday constant (9.65×10^4 C mol^{-1}), R is the universal gas constant (8.31 J K^{-1} mol^{-1}) and T is absolute temperature, at 298K. See section 2.6.1.2 on how to calculate E_{rev}.

Table 1. External and Internal solutions used for the bi-ionic reversal potential

External ionic composition (mM) solution

$CaCl_2$	TEA-Cl	HEPES
4	155	10

pH 7.4 with TEA-OH

Internal ionic composition (mM) solution

Solution	CsCl	NaCl	KCl	LiCl	EGTA*	TEA-Cl	HEPES
1	100	0	0	0	10	10	10
2	0	100	0	0	10	10	10
3	0	0	100	0	10	10	10
4	0	0	0	100	10	10	10

pH 7.2 with XOH, X = Cs+, Na+, K+ or Li+

*pH 8.0 with XOH

Anomalous mole fraction effect

I carried out the analyses of the anomalous mole fraction effect to measure the competition of sodium and calcium ions through the T-type calcium channel pore. This study required the perfusion of differing concentrations of external calcium solutions using a gravity-flow Valvelink 8.2 Telfon perfusion system. Solutions were prepared from low concentrations ($1x10^{-9}$ M) to high concentrations ($1x10^{-2}$ M) levels of calcium, in the presence of 60 mM external sodium concentration. The internal and external solutions can be found in Table 2. The peak of the current shifts with each differing solution, so the voltage step level for generating maximal currents were adjusted for each solution. To test which voltage step level generated the peak current, the cell is stepped to a range of voltage close to its peak (usually +/- 20mV) in 10 mV increments. Then the solution was switched to test differing solutions. The concentration of free calcium in the external solutions were calculated using the following website: http://maxchelator.stanford.edu/CaEGTA-TS.htm. The peak current for each solution was divided by the largest current overall to obtain the fractional of maximal current (I/I_{max}) value of differing calcium solutions.

Table 2. External and Internal solutions used for the anomalous mole fraction effect

External ionic composition (mM) solution

Solution	Ca^{2+} free	$CaCl_2$	NaCl	TEA-Cl	EGTA	HEPES	Glucose
1	$1x10^{-9}$	0.01	60	90	1.246	10	26.3
2	$1x10^{-7}$	1.00	60	90	2.236	10	20.4
3	$1x10^{-5}$	1.00	60	90	1.002	10	24.1
4	$1x10^{-4}$	0.1	60	90	0	10	29.7
5	$3x10^{-4}$	0.3	60	90	0	10	29.1
6	$1x10^{-3}$	1	60	90	0	10	27
7	$3x10^{-3}$	3	60	90	0	10	21
8	$1x10^{-2}$	10	60	90	0	10	0

pH to 7.4 with TEA-OH

Internal ionic composition (mM) solution

CsCl	EGTA	Mg-ATP	Li-GTP	HEPES
110	10	3	0.6	10

pH 7.2 CsOH

Ramp protocols

Ramp protocols involved looking at the currents elicited from a rapid and continuous voltage change from -100 mV to +100 mV in 1 second. The point of carrying out a ramp protocol is to look at the separation of differing voltage-activated currents (low and high voltage activated) during the ramp range. The voltage ramps were repeated every 10 seconds in a sweep. The cell was held for a minimum of three sweeps at a stabilized current level in the ramp before switching external solutions to examine changes in the ramp generated currents. To measure the change in current size, I normalized the sodium current to the size of the current substituted with large monovalent ion, and weakly permeant, NMDG+ ion.

Table 3. External and Internal solutions used for the ramps

External ionic composition (mM) solution

$BaCl_2$	NaCl[1]	NMDG+ [2]	TEA-Cl	$MgCl_2$	HEPES
2	100	0	50	1	10
2	0	100	50	1	10

[1] pH 7.9 TEA-OH

[2] pH 7.9 HCl

Internal ionic composition (mM) solution

CsCl	4-AP	EGTA	Mg-ATP	HEPES
135	5	10	2	10

pH 7.7 CsOH

Inward sodium permeability

Inward sodium permeability was measured as a percentage of current that is contributed by sodium ions compared to large monovalent, and weakly permeant ion, $NMDG^+$. The cell was subjected to voltages to generate maximal peak currents, repeated every 10 seconds with an inter-stimulus period where the membrane was held at -110 mV. A minimum of three sweeps

where there was no observed change in current size was collected before switching to a new external solution to evaluate the change in peak current size as a result of the solution change.

Table 4. External and Internal solutions used for the inward sodium permeability

External ionic composition (mM) solution

CaCl2	NaCl	NMDG	TEA-Cl	HEPES
2	135	0	25	10
2	0	135	25	10

pH 7.4 TEA-OH

Internal ionic composition (mM) solution

CsCl	EGTA	Mg-ATP	Li-GTP	HEPES
110	10	3	0.6	10

pH 7.2 CsOH

2.5.3 Dose responses with drugs and metal cations

Dose response curves for drugs were carried out with concentrations that spanned the low concentrations, generating no drug block to the concentration that generated a near-maximal drug block. The effect of the drug block was measured as the change in peak current as a result of drug addition. Stabilized current results in a minimum of three sweeps separated by 10 seconds each, was used to determine the effect at each drug concentration level. Percentage of current block was measured by taking the current from each concentration and dividing by the baseline maximal control current size without drug addition.

Mibefradil

Mibefradil was tested as a classical blocker of T-type channels. Mibefradil was prepared in a 5 mM stock, dissolved in distilled water and kept frozen until used. This drug permeates relatively slowly and requires the use of the Valvelink 8.2 Telfon perfusion system. Final

solutions concentrations were constituted for each of the day's experiments to the concentration needed in the external solution.

Isradipine

Isradipine is a dihydropyridine that is highly selective for L-type calcium channels, and was used to test for L-type channel currents in heart cells. Isradipine was prepared as a 10 mM stock in DMSO and kept in a 4°C fridge until use. Isradipine precipitates at cooler temperatures and needed to be fully dissolved before preparing final concentrations. A Smart Squirt microperfusion system (Automate Scentific) was used to carry out this experiment. In the Smart Squirt system, the drug delivery lines are minimized because the drug vials are directly connected to the perfusion pencil allowing for faster delivery and measurement of rapidly activating drugs like isradipine.

Nickel and Zinc

Solutions are made fresh on the day and dissolved in the external solution. Drugs were applied with the gravity-flow perfusion system controlled by teflon pinch valves operated using external buttons on a Valvelink 8.2 controller (Automate Scientific).

2.5.4 Cardiomyocytes

We did not measure any Nav1 sodium channel or Cav2 channel gene expression in cardiomyocytes. The only major pacemaker sodium or calcium currents that we could measurably conceive are L-type channels (LCav1 gene) that are abundantly expressed in snail cardiomyocytes and the Cav3 T-type channels, exon 12a isoform, that are expressed in snail cardiomyocytes. A HCN homology is also likely expressed in snail cardiomyocytes and may also contribute to cation currents, but this remains to be investigated. T-type currents and L-type channel currents are measured in 2 mM Ba^{2+}/ 100 mM $NMDG^{+}$ (see section 2.6.2), looking at a range of responses to differing voltage-steps generating current-voltage relationships. Barium was used as a charge carrier instead of calcium ions because L-type currents are dramatically slower and easier to kinetically separate from the faster T-type currents in external barium solution. Current voltage-relations were assess from a holding potential of -110 mV with voltage steps in 10 mV increments from -100 mV to +60 mV. I also repeated the step protocol from a holding potential of -60 mV. Previous studies in snail neurons (Staras, Gyori & Kemenes, 2002)

and our *in vitro* expression work suggest that most of the T-type channel current is inactivated at a holding potential at -60 mV. The difference between currents generated from the holding potential of -110 mV and -60 mV was thus likely to be the T-type channel current component that is most affected by this change in holding potential. The external solutions used to study drugs and metal cations block in snail cardiomyocytes was 2 mM Ba^{2+} and100 mM Na^{+}, see section 2.6.2.

2.5.5 Statistical Analysis

Numerical values in all electrophysiological experiments were compared using a parametric one way ANOVA when three or more data sets were compared in SPSS. If the one way ANOVA results were statistically significant, a Student-Newman-Keuls *post hoc* test was performed and reported, unless otherwise stated.

Chapter 3
Results

The research conducted in this thesis is a collaboration of Dr. J. David Spafford, Dr. Adriano Senatore, Dr. Adrienne N. Boone, Robert F. Stephens and myself (Wendy Guan). Dr. Spafford provided the figures of sequential alignments across various invertebrate and vertebrate species. Dr. Senatore cloned and characterized the electrophysiological characteristics of the *Lymnaea* snail T-type channel, LCa_v3 (Senatore and Spafford 2010) and later conducted a study of splice variants of exon 8b and 25c (Senatore et al 2012). Dr. Senatore discovered novel exons 12a and 12b, and initiated the comparative study of the *Lymnaea* Ca_v3 channels for novel exon 12a compared to exon 12b. Exon 12b was the native isoform described in the first publication describing LCa_v3 (Senatore and Spafford 2010; Senatore et al. 2012). In this thesis, Dr. Senatore carried out a comparisons of the basic kinetics, nickel block, bi-ionic reversal potential and the anomalous mole fraction for LCa_v3 channels with exons 12a and 12b. Furthermore, Dr. Adriano Senatore performed qPCR to detect the expression of LCa_v3, its splice variants, and other calcium channels (LCa_v1, LCa_v2) and sodium channels (LNa_v1 and LNa_v2) in *Lymnaea* tissues, from the brain, heart, glands and muscle. Robert Stephens, an NSERC undergraduate summer student and fourth year project student created three mutagenized channels for LCa_v3 in the domain II turret including LCa_v3-12a (DIIS5P$^{\Delta cys}$), LCa_v3-12b (DIIS5P$^{\Delta cys}$) and LCa_v3(DIIS5P$^{\alpha 1H}$) in this chapter. Dr. Boone recorded the activation kinetics of calcium currents in cardiomyocytes.

Part of this thesis is published in the journal, *Journal of Biological Chemistry*: Senatore, A***.,** Guan, W*., Boone, A.N., and Spafford, J.D. (2014) " T-type channels become highly permeable to sodium ions with an alternate extracellular turret region (S5-P) outside the selectivity filter" *Journal of Biological Chemistry*. doi:10.1074/jbc.M114.551473. (* indicates these authors have contributed equally).

3.1 Alternative splicing changes ion selectivity and permeation in Ca_v3 channels

The diversification of human T-type calcium channels are rooted as a single gene in the great pond snail, *Lymnaea stagnalis* dubbed LCav3. Through sequencing of different brain cDNAs coding for LCav3, a unique mutually-exclusive exon was identified for exon 12. Two forms of exon 12 (a and b forms) have been identified in most protostome invertebrate T-type calcium channels, including nematodes (almost all), arthropods and mollusks. Flatworms, some nematodes, some annelids and all lower deuterostomes have an exon 12a, but lack exon 12b. One annelid, *Capitella* is unusual in possessing only an exon 12b isoform. Exon 12 codes for the region that spans from the S5 membrane helix in domain II to the extracellular region known as the "turret", to the descending pore helix that projects into the pore towards the selectivity filter. As part of my thesis, I examined the two splice variants, exon 12a and 12b and compared their differences, this includes their ion selectivity and permeability with mammalian T-type calcium channels, hCav 3.1 (α1G), hCav 3.2 (α1H) and hCav 3,3 (α1G). Evaluation of T-type calcium channel functions require repeated successful transfections and expression in HEK293T cells. All the snail plasmids of LCav1 and LCav3 were constructed into a bicystronic vector containing pIRES2- EGFP. Mammalian Cav1.2, Cav3.1, Cav3.2 and Cav3.3 channels are expressed from transcriptional fusion vectors (pMT2 or pcDNA3.1) which lacked the bicystronic vector expression of EGFP, were instead co-transfected with EGFP. Positively transfected HEK293T cells were evaluated by their green fluorescence under mercury lamp illumination with an epifluorescence microscope. Primary cultured cardiomyocytes were dissociated 24 hours prior and had a muscular and elongated appearance. A small percentage of muscle cells may spontaneously contract immediately after dissociation, which was an indicator of healthy, viable cardiac cells. See an illustration of recordable HEK293T cells (Figure 3.1a) and snail cardiomyocytes (Figure 3.1b) below.

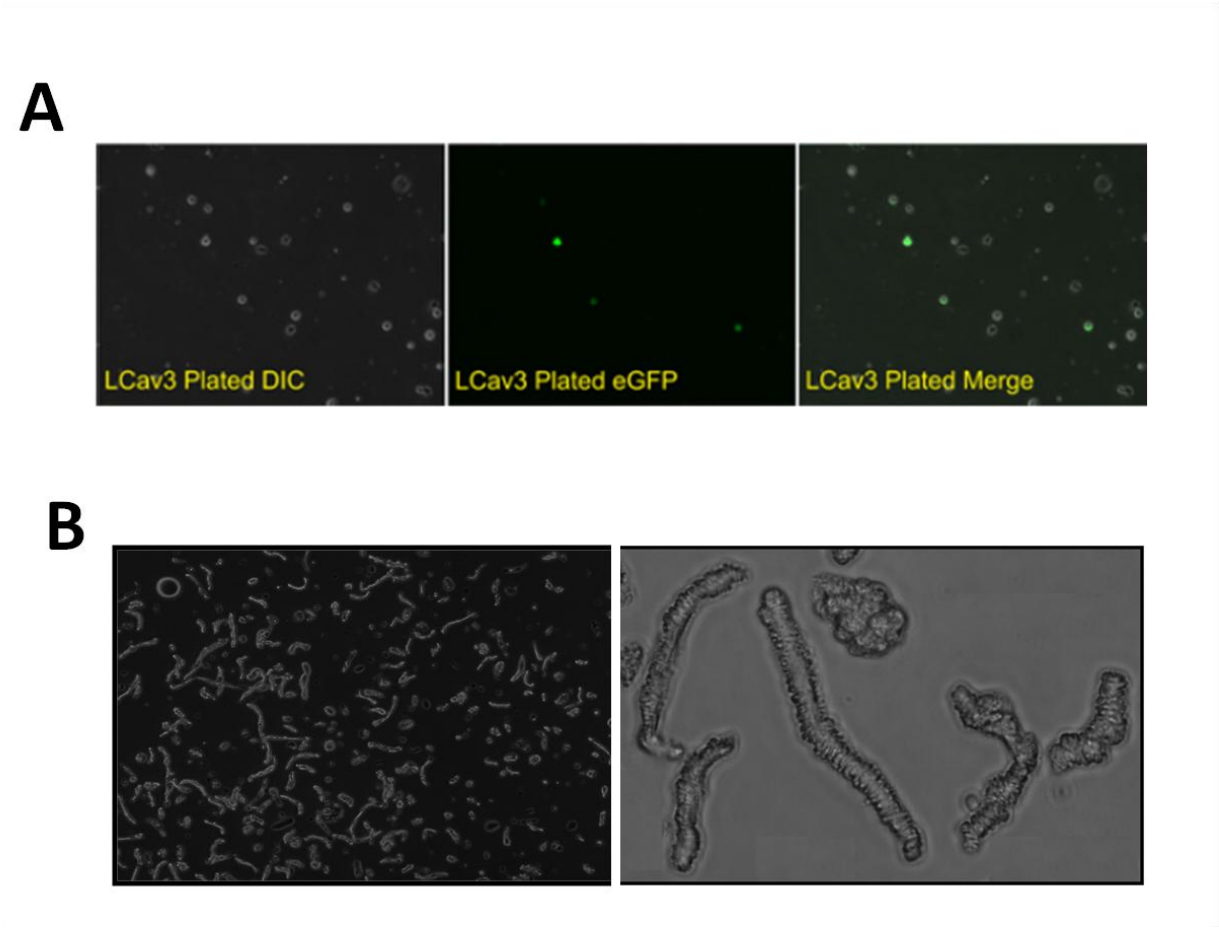

Figure 3.1. Transfection and expression of LCav3 in HEK293T cells and dissociation of cardiomyocytes.

(A) Successful transfections of LCav3 channels are trypsinized and plated onto glass coverslips, isolated for electrophysiology recordings. Images were taken using Differential Interference Contrast (DIC) on a Zeiss AxioObserver Z1 microscope. (B) The left panel shows the typical density of ventricular cardiomyocytes obtained from four adult snails immediately after dissociation, zoomed at 10x magnification. A close up of these cardiac cells reveal their muscular appearance at 40x magnification in the right panel.

3.1.1 Biophysical properties of LCav3 and hCav3 channels

A notable difference detected between 12a and 12b variant is a large outward current, this is present in LCav3-12a with voltage steps above 0 mV that is not present in the expression of LCav3-12b (Figure 3.2b). It is suspected that this large outward current is carried out by internal 110 mM cesium ions from the intracellular patch pipette, since this is the only major cation within the pipette. Replacement of internal Cs^+ with a large monovalent cation, N-methyl-D-glucamine (NMDG), diminishes the large outward current in LCav3 isoforms. Despite differences in outward currents, LCav3 isoforms retain similar kinetics to activation, inactivation, tau inactivation, time to peak and nickel blocking concentration at 300 μM concentration. The 12b variant differs slightly from 12a for recovery from inactivation, with exon 12b occurring at a slower rate, and having a faster deactivation rate (see Figure 3.2 C-I). Overall the biophysical properties of snail Cav3 T-type channels are reminiscent of the characteristic features of mammalian Cav3 calcium channels, such as low voltage activation, rapid inactivation kinetics, slow deactivation and possessing a window current maximal near the resting membrane potential of -65 mV, see Table 5 for kinetic values.

Comparison of hCav3 channel currents through a series of voltage steps, reveal a minor outward current by Cs^+ ions, indicating less permeable channels than snail LCav3 channels (see Figure 3.3). T-type currents generated from different hCav3 channel genes have distinct kinetic properties. hCav 3.1 produces a faster activation and inactivation kinetics to hCav 3.2, yet they both activate and inactivate at similar voltages. A slower and positively shifted voltage-sensitivity is produced with the hCav 3.3 channel subunit and is nearly three times slower to activate than Cav3.1 or Cav3.2 channels and possess the slowest kinetics of inactivation compared to the other mammalian T-type channels. Another significant difference between hCav3 channel isoforms is their recovery from inactivation. hCav3.1 recovered the fastest followed by hCav3.3 and hCav3.2. The exact values differ from that reported by Chemin and colleagues (2002) but the hCav3 channels follow a similar trend as that reported by Chemin et al.(2002). The differences can be accounted for by experimental parameters and the different hCav3 splice isoforms that were included.

The snail LCav3 T-type channels are negatively shifted in their activation and inactivation threshold properties by ~10 mV compared to their mammalian counterparts. Furthermore, LCav3 isoforms have a faster time to peak, tau inactivation and deactivation

values, but are slower to recover from inactivation. Snail T-type isoforms were not statistically significant from hCav3.2 kinetics in recovery from inactivation. A ~1.3 increase in current when barium is the charge carrier in LCav3 resembles hCav 3.2 (Shcheglovitov, Kostyuk & Shuba, 2007). A summary table of all T-type channel kinetics are presented in Table 5 and an one way ANOVA combined with a Student Newman-Keuls *post hoc* test comparing Cav3 channels is presented in Table 6.

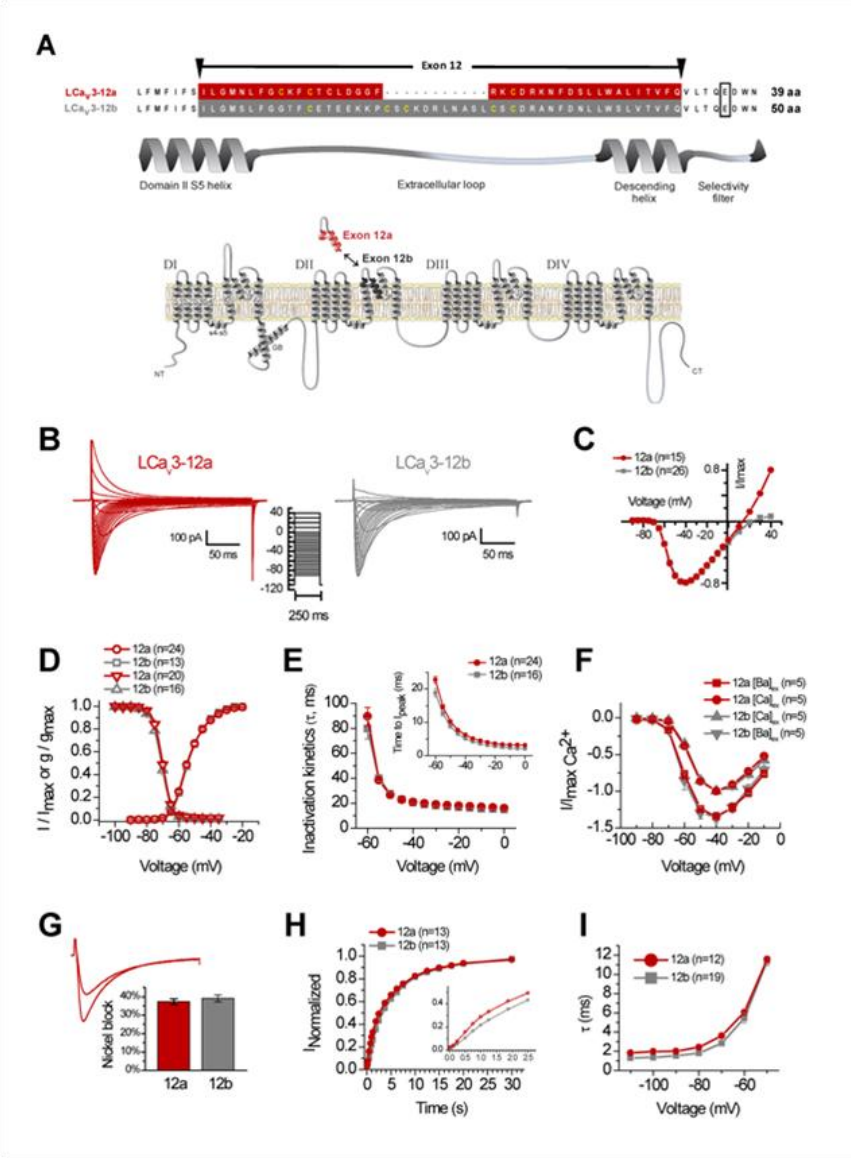

Figure 3.2. Characterization of biophysical properties of LCa$_v$3-12a and 12b.

(A) An illustration depicting the aligned turret sequences in Domain II in LCav3, comparing the sequence between exon 12a and 12b in the top panel. Beneath the panel is an illustration of the extracellular turret region for exon 12a and 12b in Domain II. (B) Differences in outward Cs^+ currents were observed without major differences in biophysical properties between LCa$_v$3-12a and LCa$_v$3-12b in 2 mM $CaCl_2$ from a holding potential of -110 mV. (C) A normalized current – voltage (IV) curve (D) Activation and steady state inactivation curves with a noticeable window current (E) Similar properties in tau inactivation (ms) and time to peak (ms) are plotted. (F) Current size differences between $[Ba^{2+}]_{ex}$ vs. $[Ca^{2+}]_{ex}$, currents in both LCav3 isoforms are ~1.3 times larger when barium is the charge carrier. (G) Percentage of nickel block at a concentration of 300 µM for LCav3-12a and 12b are 37.28 ± 1.54% (n=5) and 39.10 ± 1.84% (n=5) respectively. (H) Recovery time from inactivation is slower in LCav3-12b. (I) Deactivation kinetics are slower with LCa$_v$3-12a.

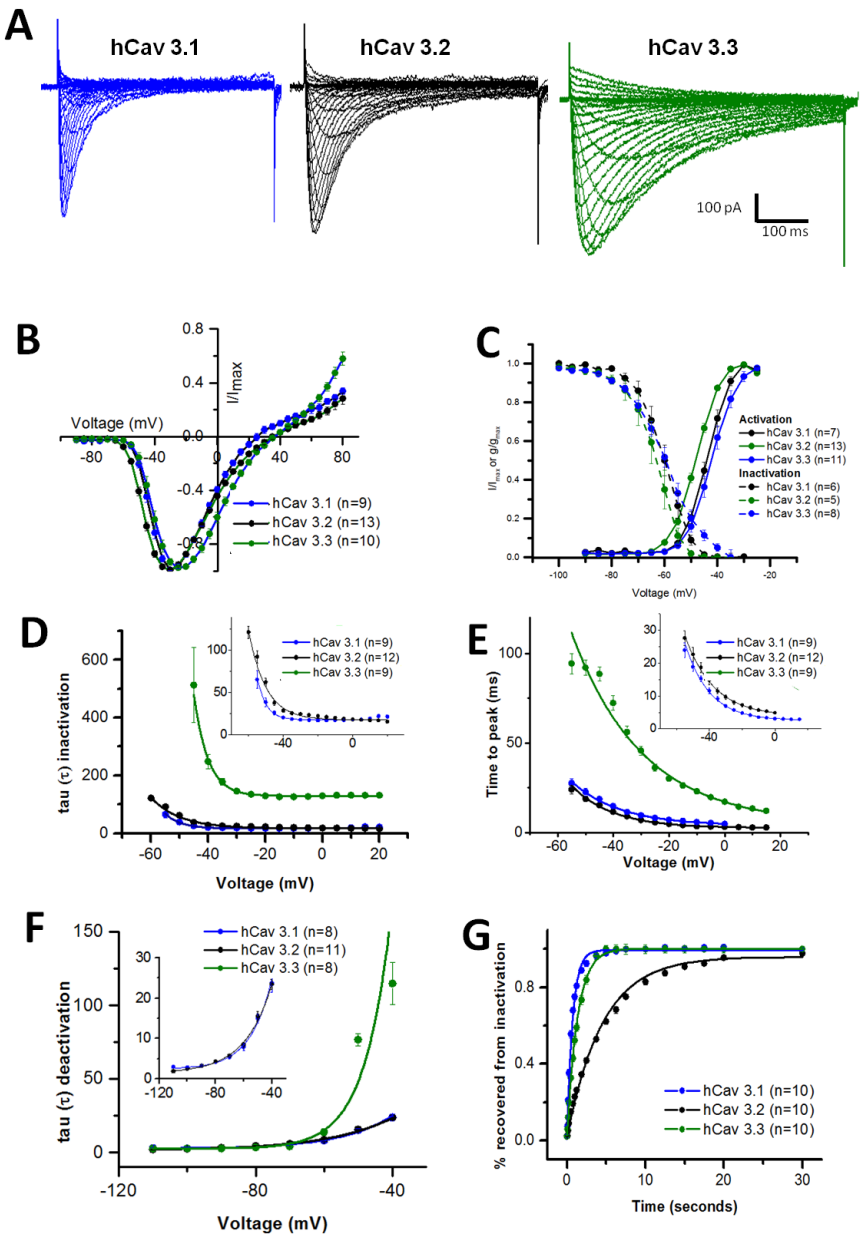

Figure 3.3. Characterization of biophysical properties of mammalian calcium channels hCav3.1, hCav3.2 and hCav3.3.

(A) Typical current recordings generated from hCav3 subunits using voltage-steps from a holding potential of -110 mV. hCav3.3 is significantly slower to activate than hCav3.1 and hCav 3.2. (B) I-V curves of human hCav3 channels, illustrating the relatively minor outward current compared to snail LCav3 channels (C) Activation and steady state inactivation curves reflect the low voltage-sensitivity of T-type channels. (D) Tau inactivation (ms) is slower in hCav 3.3 than hCav 3.1 and hCav 3.2. (E) Time to peak (ms) values are also slower in hCav 3.3 and the fastest in hCav 3.1. (F) Tau deactivation is similar between hCav 3.1 and hCav3.2, and slowest for hCav 3.3. (G) Recovery from inactivation is the fastest for hCav3.1, followed by hCav 3.3 and hCav3.2.

Table 5. A summary table of biophyical kinetics in LCav3 and hCav3 calcium channels.

	LCav3-12a	n	LCav3-12b	n	12a/12b	hCav 3.1	n	hCav 3.2	n	hCav3.3	n	3.1/3.2	3.1/3.3	3.2/3.3
Activation														
$V_{1/2}$	-53.63 ± 0.35	24	-53.48 ± 0.34	13	n.s.	-43.75 ± 0.94	7	-48.58 ± 0.54	13	-42.16 ± 1.24	11	**	n.s.	**
K	5.60 ± 0.09	29	5.46 ± 0.14	13	n.s.	3.88 ± 0.18	7	3.85 ± 0.14	13	3.95 ± 0.24	11	n.s.	n.s.	n.s.
Peak of IV	-40 mV	24	-40 mV	13		-30 mV	7	-30 mV	13	-25 mV	11			
Inactivation														
$V_{1/2}$	-70.21 ± 0.38	20	-70.89± 0.49	16	n.s.	-60.33 ± 1.71	6	-62.88 ± 2.25	5	-59.72 ± 1.42	8	n.s.	n.s.	n.s.
K	2.73 ± 0.04	20	2.93 ± 0.08	16	**	4.75 ± 0.23	6	4.78 ± 0.37	5	6.56 ± 0.38	8	n.s.	**	**
Activation kinetics														
TTP -55 mV (ms)	14.68 ± 0.63	24	12.62 ± 0.70	16	*	23.93 ± 2.27	9	27.61 ± 2.27	12	94.33 ± 5.60	9	n.s.	**	**
TTP -10 mV (ms)	3.19 ± 0.39	24	2.35 ± 0.12	16	n.s.	3.53 ± 0.19	9	5.71 ± 0.37	12	23 ± 1.39	9	**	**	**
Inactivation kinetics														
τ -55 mV (ms)	38.40 ± 1.67	24	40.07 ± 2.56	16	n.s.	64.83± 10.56	9	91.91 ± 7.27	12	-	9	**	-	-
τ -10 mV (ms)	17.20 ± 0.48	24	15.67 ± 0.56	16	**	16.99 ± 0.87	9	19.49 ± 1.50	12	125.71 ± 7.91	9	n.s.	**	**
Deactivation														
τ -100 mV (ms)	1.97 ± 0.06	12	1.37 ± 0.05	19	**	2.73 ± 0.20	8	2.45 ± 0.20	11	2.57 ± 0.060	8	n.s.	n.s.	n.s.
τ -60 mV (ms)	6.05 ± 0.30	12	5.45 ±0.52	19	n.s.	7.88 ± 079	8	8.49 ± 0.68	11	13.94 ± 2.43	8	n.s.	**	**
Recovery from Inactivation														
%recovery at 0.25s	7.81 ± 0.37	13	5.33± 0.30	13	**	35.24 ± 0.01	10	8.72 ± 0.0054	10	19.64 ± 0.0080	10	**	**	**
% recovery at 5s	65.71 ± 1.13	13	62.50 ± 1.00	13	*	97.78 ± 0.070	10	62.08 ± 0.013	10	100 ± 0.021	10	**	*	**
$T_{0.5}$ (ms)	1859.74 ± 93.14	13	2243.09 ± 82.26	13	**	337.49 ± 19.99	10	2093.79 ± 95.69	10	559.69 ± 35.57	10	**	*	**

Values are expressed as means ± standard error mean (S.E.M) and *n* denotes the number of recordings performed for each data set. Statistical comparisons of LCav3-12a vs. LCav3-12b and hCav 3.1, hCav3.2 vs. hCav 3.3 were performed using a one-way ANOVA combined with a Student-Newman-Keuls *post hoc* test in SPSS with * $p < 0.05$, ** $p < 0.01$ and n.s., not significant.

Table 6. Student-Newman-Keuls *post hoc* results on LCav3 vs. hCav3 kinetics

	12A/3.1	12A/3.2	12A/3.3	12B/3.1	12B/3.2	12B/3.3
Activation						
$V_{1/2}$	**	**	**	**	**	**
K	**	**	**	**	**	**
Inactivation						
$V_{1/2}$	**	**	**	**	**	**
K	**	**	**	**	**	**
Activation kinetics						
TTP -55 mV (ms)	**	**	**	**	**	**
TTP -10 mV (ms)	**	**	**	**	**	**
Inactivation kinetics						
τ -55 mV (ms)	**	*	-	**	*	**
τ -10 mV (ms)	n.s.	n.s.	n.s.	n.s.	n.s.	**
Deactivation						
τ -100 mV (ms)	**	n.s.	*	**	**	**
τ -60 mV (ms)	n.s.	n.s.	**	n.s.	n.s.	**
Recovery from Inactivation						
%recovery at 0.25s	**	n.s.	**	**	*	**
% recovery at 5s	**	n.s.	**	**	n.s.	**
$T_{0.5}$ (ms)	**	n.s.	**	**	n.s.	**

Statistical comparisons of LCav3-12a /12b vs. hCav 3.1, hCav3.2 and hCav 3.3 were performed using a one-way ANOVA combined with a Student-Newman-Keuls *post hoc* test in SPSS with * $p < 0.05$, ** $p < 0.01$ and n.s., not significant

3.1.2 Comparison of ion selectivity and permeability

Calcium channels have a high affinity for calcium ions, and monovalent ions are normally excluded in the presence of physiological levels of extracellular calcium due to the lack of monovalent ion permeability. The addition of physiological sodium levels (135 mM sodium) in the presence of 2 mM Ca^{2+} for snail LCav3-12a generated a >15-fold increase in peak current, whereas LCav3-12b was significantly less permeable with a ~2-fold increase compared to 2 mM Ca^{2+} and 135 mM of $NMDG^{+}$ in the external bath. $NMDG^{+}$ is a large, relatively non-permeant monovalent ion that was used in place of Na^{+} ions. The hCav3 channels produced a modest increase in current size when external Na^{+} ions replaced $NMDG^{+}$. hCav3 channels are more calcium selective with a 1.27, 1.32 and 1.45- fold increase in the presence of sodium for hCav 3.1, hCav 3.2, and hCav 3.3 respectively. See Figure 3.4 for the comparisons of increased size currents in the presence of 135 mM Na^{+} ions. The permeability of calcium selective T-type channels are hCav3.1/ hCav3.2 < hCav 3.3< LCav3 – 12b < LCav3-12a, with hCav3.1/hCav 3.2 being the most calcium selective (~~3/4 to 4/5 of ions permeating would be calcium ions) and exon 12a being the least calcium selective (>9/10 of the ions permeating would be sodium ions not calcium ions). It is important to note the extracellular turret only make up 1% of the channel's length, yet we observe significant differences in permeability between two splice variants with relatively minor effect on biophysical properties.

To quantify ion permeability differences, we measured peak sizes of T-type currents generated in bi-ionic conditions. The bi-ionic conditions has one ion (calcium in this case) at high concentrations on the outside, and another ion (in this case a monovalent ion) at high concentrations on the inside. The relative contribution of the influx of calcium versus the efflux of monovalent ion, provides a relative measure of permeability, based on their influences on where the reversal potential resides. You can also gauge the relative ionic contributions as measured in the slope conductance, which is the relative change in slope in the IV curve as the linear slope change in current size over the voltage ranges for calcium influx or monovalent ion efflux.

Bi-ionic conditions included an internal solution containing 100 mM of differing monovalent ions (Li+, Na+, K+ or Cs+) in the presence of 4 mM external calcium. Currents were elicited from a holding potential of -110 mV to steps ranging from -90mV to +80mV in 5 mV increments. The relative permeability of monovalent ions followed the ion selectivity model

of Eisenman et al. (1967), Li+ > Na+ > K+ >Cs+, where Li+ ions are the most permeable and Cs+ are the least. This is consistent with decreasing permeability as crystal radii of monovalent ions increase from Li+ < Na+ < K+ <Cs+, Å = 0.60, 0.95, 1.33 and 1.69 respectively. The change in reversal potentials contributed by each monovalent ion reflects its relative permeability to the reference external calcium ion and signifies an increase in current contribution, shifting the reversal potential to the left, see Figure 3.5. The more permeant the monovalent ion, the more the reversal potential would shift to the left for an outward monovalent ion versus the more positively shifted reversal potential for inward calcium ions. Calculating the relative permeability using the bi-ionic Nernst equation reveals a P_{Ca}/P_x average of 23, 32, 50 and 114 for Li^+, Na^+, K^+ and Cs^+ respectively for LCav3-12a and 26, 41, 78 and 114 for LCav3-12b. The relative permeability ratios for hCav3 channels are higher: Li^+, Na^+, K^+ and Cs^+, hCav3.1: 45, 89, 140, 155, hCav3.2: 45, 84, 172 and 445 and hCav3.3: 32, 55, 151 and 166. LCav3 with exon 12a are significantly more permeable than LCav3-12b and the mammalian T-type channels. Relative permeability ratios indicate that hCav3.1 and hCav3.2 have similar permeability ratios for Li^+ and Na^+ ions compared to calcium ions. L-type channels are more selective for calcium ions and their monovalent ion permeability is barely detectable in bi-ionic conditions, with relative ratios of 424, 1170, 3000 and 4200 for Li+, Na+, K+ and Cs+ respectively (Hess, Lansman & Tisen, 1986).

Another method of examining relative permeability is the linear slope conductance between voltage steps +70 to +80 mV, where the outward monovalent ion currents possesses a steeper slope conductance reflects a much greater outward monovalent current (see Figure 3.6). LCav3-12a has a greater outward slope conductance, comparing the snail Cav3 isoforms and the three hCav3 channels. One deviation between the relative permeability and slope conductance measurement is that hCav 3.3 channels has a larger outward slope conductance for Li^+ and Na^+ ions than LCav3-12b, but hCav 3.3 has a lower relative sodium and lithium permeability as reflected in their contribution to changes in reversal potential. The lower relative sodium permeability of hCav3.3 compared to LCav3-12b is consistent in the fold increase in current size of 1.45 in the presence of sodium, while LCav3-12b had a larger, two fold increase in current size in the presence of sodium ions. A potential issue with the accuracy of the slope conductance, is that the IV curves represent both the driving force and the voltage-dependence of channel opening, the latter of which can alter the relative conductance values. Cav3.3 is notably

positively shifted in its IV curve. We could have measured channel activation from protocols that generate tail currents to avoid this issue, which circumvents the voltage-dependence of channel opening. Another issue is that the relative sodium permeation in the bi-ionic experiments is a measure of the outward sodium flux instead of an inward sodium flux. The relatively high slope of outward currents at very depolarized potentials is not very physiological relevant, when sodium is usually entering as an inward ion competing with calcium entry into the pore. Values for reversal potential, relative permeability and slope conductance are summarized in Table 7.

The anomalous mole fraction effect experimental set up is used to evaluate how monovalent ions such as sodium enter from the outside of the channel through the pore and competes with calcium ions for limited pore binding sites. We measured the changing peak amplitudes of inward-permeating calcium current in 60 mM extracellular Na+ ions, in 10-fold increment doses of external calcium ions, in a range from 10^{-9} to 10^{-2} M. As calcium levels rose, there was an increased blocking of the sodium currents by calcium ions (Figure 3.7A), reflecting a decrement of the sodium current with increasing external calcium. A striking difference for channels with exon 12a is a weak calcium blocking effect (44.5 ± 4.0%) compared with a more complete block with exon 12b turret (81.2 ± 1.6%) at 10 μM of extracellular calcium ions. The mammalian T-type channels show a greater calcium block at 10μM, 96.06 ± 0.46% for hCav 3.1, 93.62 ± 2.73% for hCav 3.2 and 96.78 ± 0.34% for hCav3.3, which are consistent with the results obtained from Shcheglovitov, Kostyuk & Shuba (2007). Above 10 μM of calcium, calcium ions are more numerous and now outcompetes sodium in the pore and ion currents rise dramatically for mammalian T-type channels as calcium ions reaches physiological (millimolar) calcium levels. An increasing block of the sodium current, leads to a decrement in current size, followed by an increasing permeation of the calcium current with increasing calcium concentration as the calcium ion concentration overwhelms the sodium ion contribution. The anomalous mole fraction effect is typically represented as a "U" shaped curve in a current size versus calcium concentration graph. Typically a two Hille equation is applied to measure the rate of block for sodium ions and the saturation rate of calcium ion permeation, however, this could not be measured accurately in LCav3 channels. Current sizes through hCav 3.1 rise 9.1 fold from 10 μM to 10 mM, 7.9 fold for hCav 3.2, 5.9 fold for hCav 3.3. Whereas, from 10 μM to 10 mM, current sizes monotonically declined for snail Cav3 channels, with a 6.9 fold and

2.1fold decrease for LCav3 channels with exon 12a and exon 12b, respectively. These changes in current sizes reflect the greater calcium permeability of mammalian T-type channels and a weaker calcium permeability of snail LCav3 channels through the physiological concentration of calcium ions. The relative increase in sodium ions in the presence of calcium, the calculated relative permabilities and slope conductances from bi-ionic solution experiments and the anomalous mole fraction experiments, all demonstrate a similar trend in calcium selectivity: hCav3.1/ hCav3.2 >hCav 3.3 > LCav3-12b > LCav3-12a.

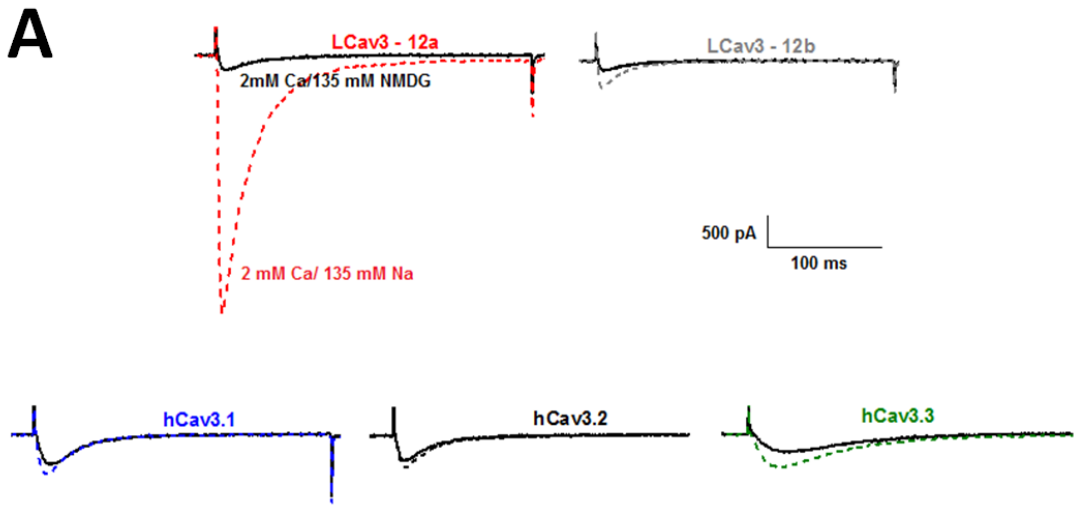

B

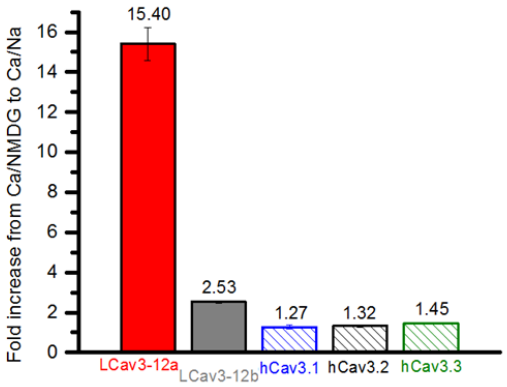

C

Channel	Increase ± S.E.M	n
LCav3- 12a	15.40 ± 0.83	5
LCav3 – 12b	2.53± 0.096	7
hCav 3.1	1.27 ± 0.092	4
hCav 3.2	1.32± 0.046	11
hCav 3.3	1.45 ± 0.076	6

Figure 3.4. Sodium ions increase overall calcium currents in Cav3 channels.

(A) T-type currents are generated from 2mM calcium and 135 mM NMDG. The addition of 135 mM sodium instead of NMDG increases the overall current. The top row are the relative fold increases in snail Cav3 channels and the bottom are the hCav3 channels. (B) Bar graph to illustrate how permeable LCav3-12a is, in comparison to other T-type calcium channels. (C) A summary table of the averages ± standard mean error (S.E.M.) of relative sodium increase, *n* is denoted as the number of recordings per data set. No statistical analysis was performed.

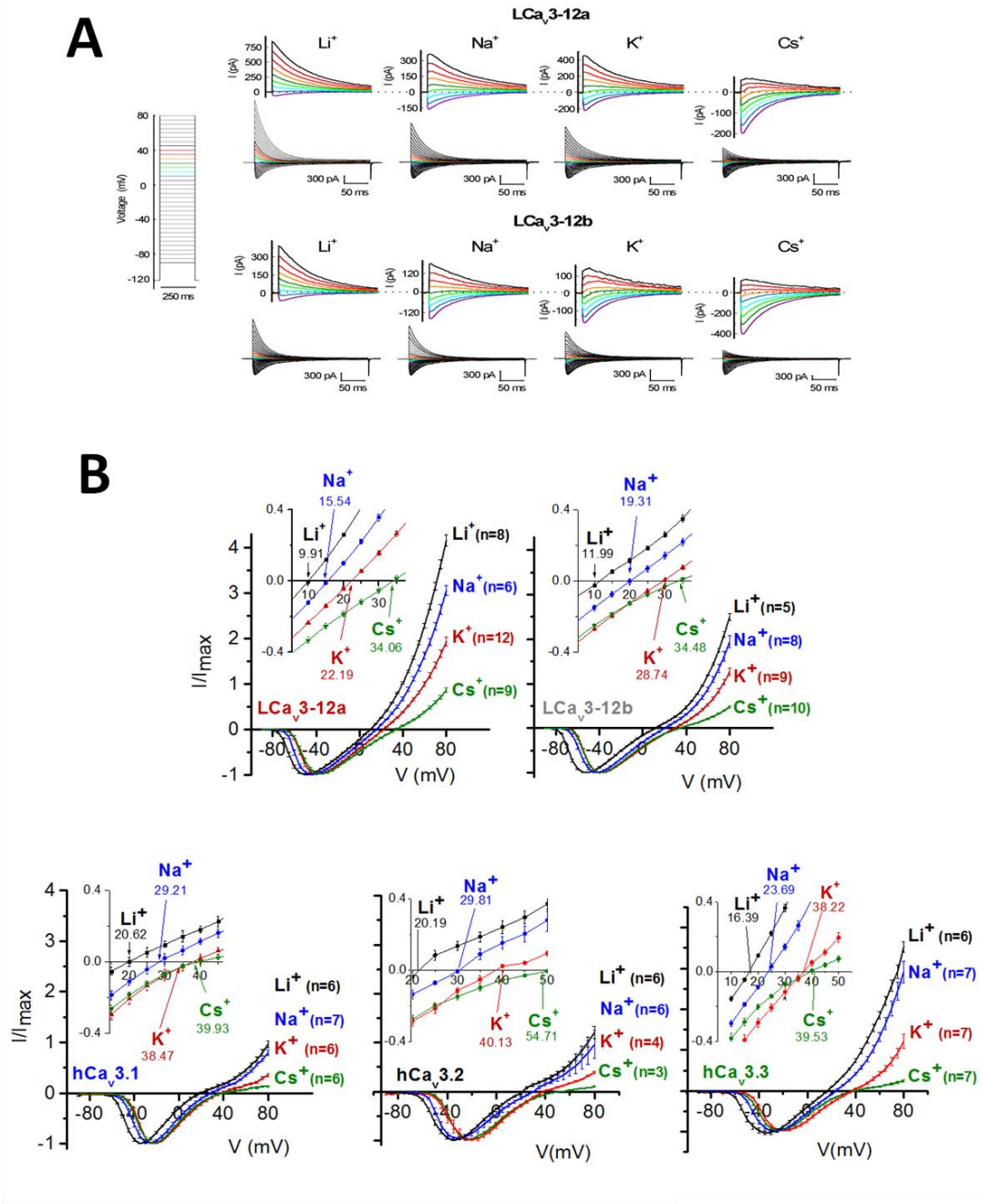

Figure 3.5. Monovalent ion (Li^+, Na^+, K^+ and Cs^+) permeability through snail Cav3 and mammalian Cav3 T-type channels.

(A) Inward calcium currents in 4 mM external calcium and outward monovalent T-type currents generated with 100 mM of internal Li^+, Na^+, K^+ and Cs^+, elicited from a -110 mV holding potential. Representative currents for LCav3-12a and 12b are shown in panel A. (B) Current-voltage relationships among all Cav3 T-type channels, *n* values are shown in parentheses. A close-up of currents crossing the reversal potentials (inset) illustrates how differing ions shift the reversal potentials.

A

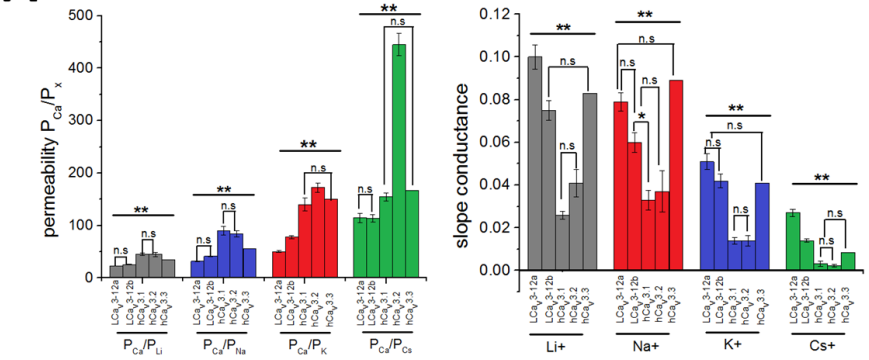

B

Relative Permeability

	LCav3-12A				LCav3-12B			hCav3.1		hCav3.2
	12B	3.1	3.2	3.3	3.1	3.2	3.3	3.2	3.3	3.3
Li+	n.s.	**	**	**	**	**	**	n.s.	**	**
Na+	n.s.	**	**	**	**	**	*	n.s.	**	**
K+	**	**	**	**	**	**	**	**	n.s.	**
Cs+	n.s.	*	**	**	*	**	**	**	n.s.	**

Slope Conductance

	LCav3-12A				LCav3-12B			hCav3.1		hCav3.2
	12B	3.1	3.2	3.3	3.1	3.2	3.3	3.2	3.3	3.3
Li+	**	**	**	*	**	**	n.s.	n.s.	**	**
Na+	n.s.	**	**	n.s.	*	n.s.	**	n.s.	**	**
K+	n.s.	**	**	n.s.	**	**	n.s.	n.s.	**	**
Cs+	**	**	**	**	**	**	*	n.s	n.s.	n.s.

Figure 3.6. Relative permeabilities and slope conductances for Cav3 T-type channels.

A one-way ANOVA was performed combined with a Student-Newman-Keuls *post hoc* test. A line over all bars represents the significance within all the groups, unless otherwise stated. * $p<0.05$, **$p<0.01$ and n.s., not significant. (A) A bar graph illustrating the relative permeabilities (P_{Ca}/P_x) amongst Cav3 T-type channels. LCav3-12a has a greater monovalent ion permeability than the other channel types. Slope conductances are compared. LCav3-12a has the greatest outward slope conductance, indicative of a more permeable channel. (B) A table to illustrate the Student-Newman-Keuls *post hoc* test results for relative permeability and slope conductance between LCav3 and hCav3 channels.

Table 7. Summarized table of values for reversal potentials, relative permeabilities and slope conductance of Cav3 channels.

Reversal Potentials (E_{rev})

	Li^+	SEM	n	Na^+	SEM	n	K^+	SEM	n	Cs^+	SEM	n
E_{rev} LCav3-12a	9.91	0.27	8	15.54	0.31	6	22.19	0.44	12	34.06	1.02	9
E_{rev} LCav3-12b	11.99	0.33	5	19.31	0.27	5	28.74	0.65	9	34.48	1.10	10
E_{rev} hCav3.1	20.62	0.72	6	29.21	1.84	7	38.47	1.82	6	39.93	1.58	6
E_{rev} hCav3.2	20.19	1.41	6	29.81	0.88	6	40.13	0.74	4	54.71	1.74	3
E_{rev} hCav3.3	16.39	0.30	6	23.69	0.58	7	39.53	0.89	7	38.22	0.68	7

Relative Permeability (P_{ca}/P_x)

	P_{Ca}/P_{Li}	SEM	n	P_{Ca}/P_{Na}	SEM	n	P_{Ca}/P_K	SEM	n	P_{Ca}/P_{Cs}	SEM	n
$P_{Ca/Px}$ LCav3-12a	22.74	0.41	8	32.01	0.71	6	50.25	1.53	12	114.51	8.85	9
$P_{Ca/Px}$ LCav3-12b	25.59	0.59	5	41.32	0.75	6	78.04	2.81	9	113.84	6.97	10
$P_{Ca/Px}$ hCav3.1	45.28	2.11	6	89.56	8.21	6	140.16	12.02	5	154.65	7.99	5
$P_{Ca/Px}$ hCav3.2	44.80	3.79	6	84.30	5.32	6	172.49	9.12	4	444.82	21.06	3
$P_{Ca/Px}$ hCav3.3	32.24	0.66	6	55.49	2.22	7	151.00	6.90	7	166.37	9.64	7

Slope Conductance

	Li^+	SEM	n	Na^+	SEM	n	K^+	SEM	n	Cs^+	SEM	n
Outward g_x LCav3-12a	0.10	0.0057	8	0.079	0.0042	6	0.0051	0.0037	12	0.027	0.0017	9
Outward g_x LCav3-12b	0.075	0.0046	5	0.060	0.0047	5	0.042	0.0032	9	0.014	0.0008	10
Outward g_x hCav3.1	0.026	0.0018	6	0.033	0.0046	7	0.014	0.0014	6	0.0033	0.0012	6
Outward g_x hCav3.2	0.041	0.0065	6	0.037	0.0097	6	0.014	0.0025	4	0.0022	0.00066	3
Outward g_x hCav3.3	0.083	0.0050	6	0.089	0.0095	7	0.041	0.0044	7	0.0084	0.00073	7

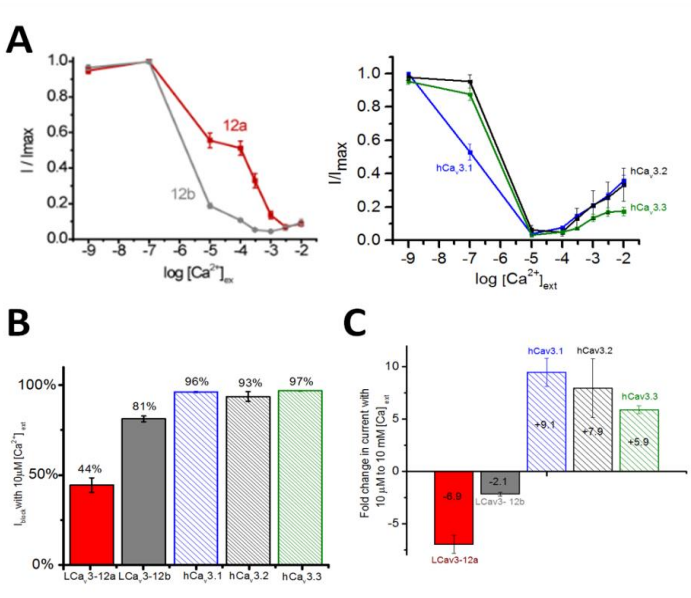

D

log [Ca2+]ext	LCav3-12a % current block	LCav3-12a SEM	LCav3-12a n	LCav3-12b % current block	LCav3-12b SEM	LCav3-12b n	hCav3.1 % current block	hCav3.1 SEM	hCav3.1 n	hCav3.2 % current block	hCav3.2 SEM	hCav3.2 n	hCav3.3 % current block	hCav3.3 SEM	hCav3.3 n
-9	5.19	1.61	7	3.47	1.6	6	0	0	4	2.3	2.01	4	4.74	1.65	5
-7	0	0	7	0.21	0.16	6	34.1	4.78	4	4.7	4.1	4	12.4	3.62	5
-5	44.46	4.03	7	81.22	1.58	6	96.06	0.49	4	93.62	2.73	4	96.78	0.34	5
-4	48.8	4.02	7	89.31	0.95	6	92.27	0.5	4	95.08	2.23	4	94.87	0.63	5
-3.52	67.08	3.99	7	94.72	0.52	6	85.15	0.88	4	86.84	6.2	4	92.72	0.83	5
-3	86.4	2.18	7	95.55	0.83	6	79.24	1.02	4	78.73	8.63	4	86.53	2.25	5
-2.25	92.94	0.95	7	93.68	1.32	6	73.11	1.8	4	74.42	9.44	4	82.9	2.44	5
-2	91.46	1.03	7	90.65	1.99	6	64.1	3.17	4	66.72	9.95	4	82.52	2.56	5

E

SNK *post hoc* for AMFE

log [Ca2+]ext	LCav3-12A				LCav3-12B			hCav3.1		hCav3.2
	12B	3.1	3.2	3.3	3.1	3.2	3.3	3.2	3.3	3.3
-9	n.s.	n.s.	n.s.	n.s.	n.s.	n.s.	n.s.	n.s.	n.s.	n.s.
-7	n.s.	**	n.s.	n.s.	**	n.s.	n.s.	**	**	n.s.
-5	**	**	**	**	**	*	**	n.s.	n.s.	n.s.
-4	**	**	**	**	n.s.	n.s.	n.s.	n.s.	n.s.	n.s.
-3.52	**	**	**	**	n.s.	n.s.	n.s.	n.s.	n.s.	n.s.
-3	n.s.	n.s.	n.s.	n.s.	*	*	n.s.	n.s	n.s.	n.s.
-2.25	n.s.	**	**	n.s.	**	**	n.s.	n.s.	n.s.	n.s.
-2	n.s.	**	**	n.s.	**	**	n.s.	n.s.	**	*

Figure 3.7. The anomalous mole fraction effect on snail Cav3 and mammalian Cav3 T-type channels.

(A) An increasing block of maximal ionic current (I/I_{max}) in 60 mM Na^+ external with increasing calcium concentration. The drop in current size with 10^{-9} to 10^{-5} M external calcium reflects the competition of calcium ions preventing sodium permeation through the pore. The left panel represents snail LCav3 exon 12a and 12b turrets and the right compares the mammalian T-type channels. (B) The percentage of calcium block is represented in a bar graph, with its standard error of mean. (C) Comparing the relative rise/decline from 10^{-5} to 10^{-2} M external calcium, LCav3-12a shows the greatest decline and hCav 3.1 exhibited the largest rise in current size. (D) A summary of calcium block at calcium concentrations ranging from 10^{-9} to 10^{-2}M with log concentration of calcium comparing all Cav3 channels. Average means of percentage current block compared to maximum current size are shown with their standard error means (S.E.M) and *n* values, the number of cells.(E) A one-way ANOVA was performed combined with a Student-Newman-Keuls *post hoc* test. * $p<0.05$, ** $p<0.01$ and n.s., not significant.

3.1.3 Investigating LCav3-12a in *Lymnaea* ventricular cardiomyocytes

We evaluated the mRNA expression density of differing extracellular turrets, exon 12a and 12b in adult and juvenile snail tissues by real-time, quantitative polymerase chain reaction (qPCR) to determine where sodium permeable channels were found. qPCR is used to quantify the quantity of cDNA template derived from the reverse-transcript of mRNA isolated from differing tissues. A fluorescent label, SyberGreen is incorporated into the DNA strands amplified in the PCR, and the amount of fluorescence as a measure of DNA synthesis is measured by a charge couple drive (CCD) camera associated with the PCR machine. A cycle threshold (CT) for PCR amplification can be extrapolated from the fluorescence curves generated during PCR amplification, which provides a quantitative measure of the amount of original cDNA template, and mRNA from the sample. Gene expression levels are compared to a control, hypoxanthine phosphoribosyltransferase 1 (HPRT1) gene, a housekeeping enzyme that is presumed to be expressed consistently in all cells and display a stable amount of expression under varying experimental conditions. The highest density of T-type channels was detected in the snail heart, where expression is exclusively the sodium-permeant LCav3-12a isoform with the absent of LCav3-12b (Figure 3.8A). Whole snail Cav3 transcript levels steeply decline during embryonic development and LCav3-12a falls from juvenile to adulthood. LCav3-12b is equally abundant in the brain as LCav3-12a but is almost exclusively expressed in secretory reproductive tissue (prostate and albumen gland), where LCav3 expression rises from juvenile to adults, potentially playing a role in sexual maturation. The relative density of mRNA for all relevant voltage gated channels comparing the heart and brain is shown in Figure 3.8C. Snail hearts express two major cation channels, L-type calcium channel (LCav1) and highly sodium permeant T-type calcium channel (LCav3-12a). While sodium channels (LNav1), and LCav2 calcium channels are abundantly expressed in the brain, mRNA transcript levels are absence for these cation channels in the heart.

We co-expressed and analyzed LCav1 (plus its required β and $\alpha_2\delta$ subunits) and LCav3-12a in HEK293T, a configuration expected to mimic the major cation channels in snail cardiomyocytes. Voltage ramps were generated from -100 mV to +100 mV to separate low voltage activated T-type and high voltage activated L-type channels in an external of 2mM barium and 100 mM NMDG as seen in Figure 3.8D-E. A sodium current is revealed through LCav3-12a when 100 mM NMDG is replaced with equimolar sodium ions, while, LCav1 current

remains unchanged when external NMDG is replaced with sodium, reflecting the lower sodium permeation of the LCav1, L-type calcium channel. Remarkably, the *in vitro* expressed subunits of LCav3-12a and LCav1 generates a similar profile of ramp currents as adult snail cardiomyocytes, with roughly an 11 fold increase in current size in external sodium and barium ions compared to NMDG and barium ions. The only major difference is that the T-type channel current in cardiomyocytes and LCav3 in HEK293T peak at different voltages in snail cardiomyocytes because LCav3 cardiomyocyte channels contain an optional exon 25c (Senatore and Spafford 2012), while the *in vitro* translated version that was recorded in Figure 3.8D, lacks optional exon 25c. Also the snail L-type channel was co-expressed with rat accessory β_{1b} subunit which has different consequences to voltage-sensitivities compared to the snail accessory β subunit *in vitro* (Dawson et al. 2014).

Comparing T-type channel voltage-ramp currents, only a 2.00 ± 0.24 (n=4) fold increase in current size in the presence of sodium ions compared to $NMDG^+$ is observed in HEK cells transfected with LCav3-12b and 1.27 ± 0.089 (n=9), 1.36 ± 0.085 (n=7) and a smaller 1.50 ± 0.17 (n=6) fold increase for hCav 3.1, hCav 3.2 and hCav 3.3 respectively, reflecting the lesser sodium permeation through human T-type channels.

To test our hypothesis that the low voltage-activated sodium currents were from T-type channels, we used 2 mM barium and 100 mM Na^+ external solution to separate the kinetics of slow barium L-type currents from fast T-type currents carried mostly by sodium ions. Snail T-type currents are mostly inactivated from a holding potential of -60 mV, so the current difference generated from holding potentials of -100 mV and -60 mV reflect the T-type calcium current with rapid kinetics (Figure 3.9). We also used pharmacology to differentiate T-type channel currents from the L-type calcium channel currents in snail cardiomyocytes. In voltage ramp currents, isradipine, a classical dihydropyridine L-type channel blocker, blocks snail L-type calcium currents at 1μM *in vitro* (Senatore et al., 2011). Isradipine blocked the high voltage-activated L-type channel current at 1μM with minimum blocking effect on T-type channel currents (n=6). Nickel (n=8) and miberfradil (n=8) similarly blocked L-type calcium channel currents and T-type channel currents (Figure 3.9, panel B,C).

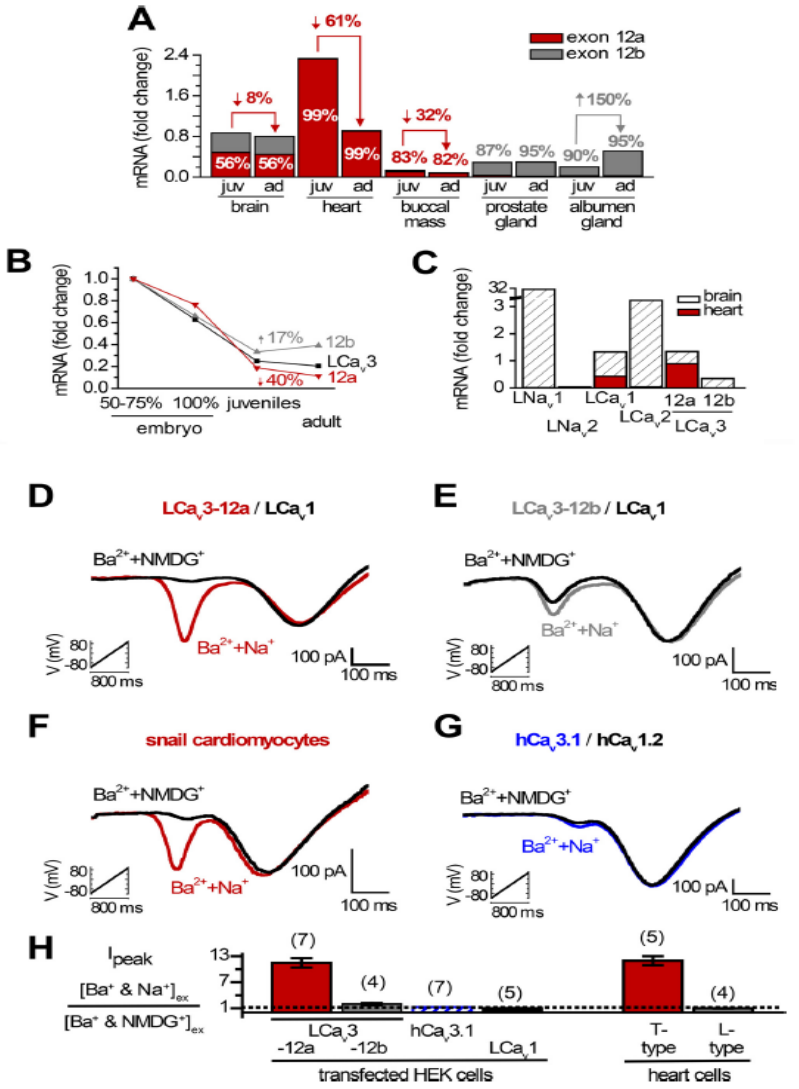

Figure 3.8. Snails express two cardiac cation currents, the highly sodium-permeant T-type channel LCav3 and the calcium-selective L-type channel LCav1.

A–C, quantitative RT-PCR standardized to *Lymnaea* HPRT1 control gene. (A) relative mRNA expression levels of exon 12a and 12b in juvenile (*juv*) and adult (*ad*) snails, reflecting the almost exclusive expression of exon12a in the snail heart and exon12b in prostate and albumen glands. (B) Dramatic decline in LCav3 channel expression in whole animals can mostly be attributed to the decline of LCav3-12a expression in the developing heart. (C) Snail hearts lack mRNA expression of any sodium channel (LNav1and LNav2).Snail hearts also lack any expression of the LCav2 synaptic non-L-type channel or the Cav3 T-type channel gene with exon 12b. Note the break in the *y* axis scale, illustrating that the range of expression of the sodium channel gene of LNav1 in the snail brain is 30-fold higher than the control HPRT1 gene, compared with the low levels of expression of the other calcium channel genes (which vary up to 3-fold higher than the control HPRT1 gene). *D–G,* ramp protocols (-110 to +100mV in 1 second) carried out in the presence of external solutions 2 mM barium and 100 mM NMDG/Na^+. (D) A sodium-permeant, T-type current is revealed and superimposed on the barium current in cardiomyocytes in the presence of a sodium-impermeant, L-type current (E) Co-transfection of LCav3 with exon 12b (F) The sodium permeant T-type currents in cardiomyocytes are indistinguishable from mammalian HEK-293T cells transfected with LCav3, exon 12a co-expressed with LCav1 and accessory subunits (β and $\alpha_2\delta$); (G) human Cav3.1 has some sodium permeability but is not as sodium permeant as the LCav3-12a variant expressed in cardiomyocytes. (H) A bar graph representing average means with standard error means (S.E.M) for relative increase of combined barium and sodium current.

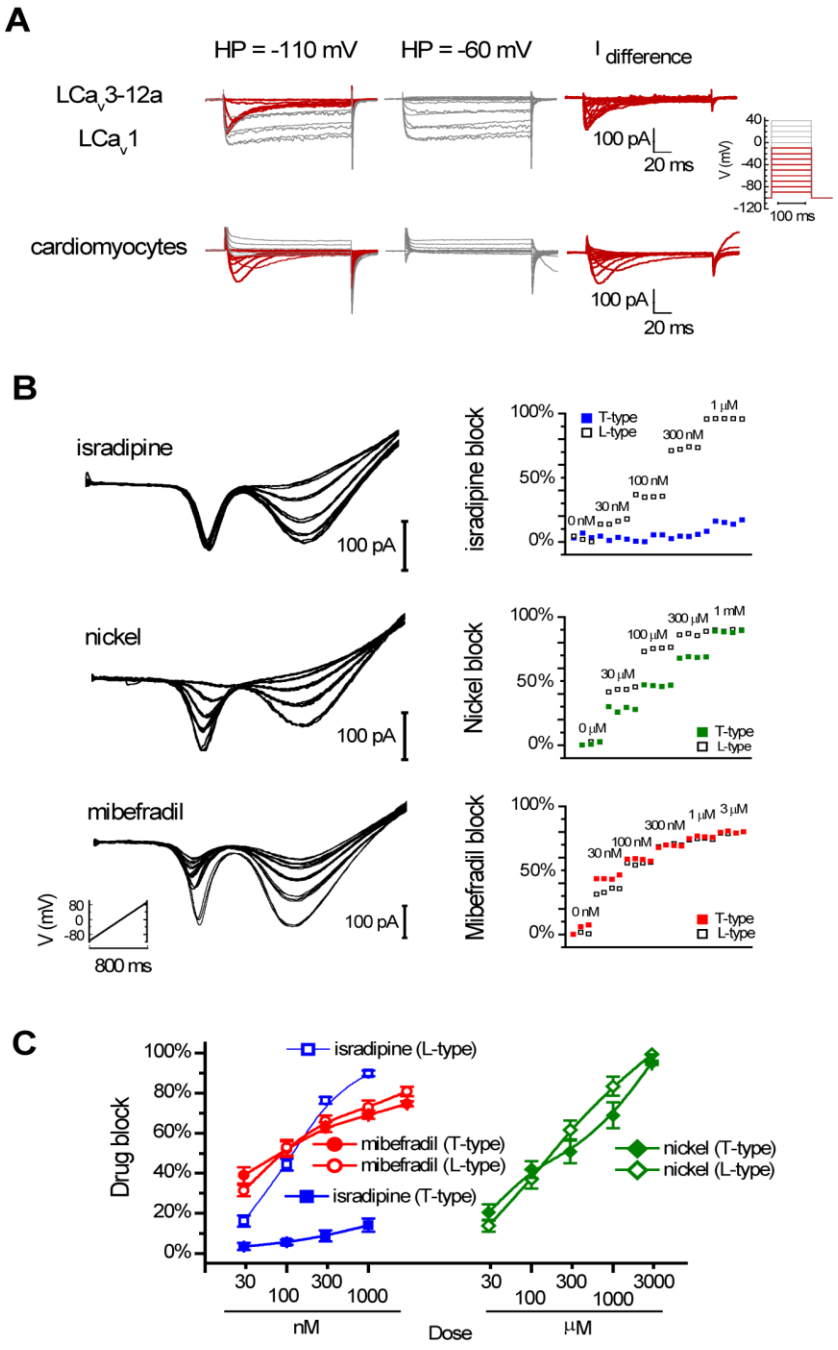

Figure 3.9. Separation of L-type and T-type currents in cardiomyocytes and drug response profiles.

(A) A fast T-type current (red) is isolated from subtracting the current at -110 mV versus -60 mV in 2 mM barium and 100 mM sodium. L-type currents are elicited from a holding potential of -60 mV shown in gray. The top panel is a co-transfection of LCav3-12a and LCav1, while the bottom panel shows a recording from a typical cardiomyocyte. (B) Ramp protocols are used to profile drug responses, sample tracings of the inhibitory effect is shown with israpidine , nickel and mibefradil on the left, along with the percentage of block relative to drug concentration on the right. (C) Dose response curves with S.E.M for israpidine, nickel and mibefradil.

3.1.4 Genomic analysis of exon 12

Analyses of Cav3 genomic sequence reveals that alternative splicing generates two forms of exon 12 (exon 12a and exon 12b). Exon 12, like in snail *Lymnaea stagnalis* is widely present but limited to protosome invertebrates (ie. non-echinoderm invertebrates), see Figure 3.10. Exon 12a is short with 38-46 amino acids long (average of 40.7 amino acids) with a conserved tri-cysteine structure , CXXC…C. Exon 12b has a penta-cysteine structure C…CXC…CXC in most protosomes or CXXC… C…CXC in some nematodes and it is always longer with a range of 48-55 amino acids (average is 52.1 amino acids). The more calcium selective mammalian T-type channels differ from exon 12 turrets with a uni-cysteine framework, suggesting that cysteines play a potential role in modulating ion permeability and selectivity. The next section examines the consequences to ion permeability and ion selectivity, and other properties of T-type channels. After substitution of all but one of the conserved tri- and penta-cysteine residues of the snail LCav3 channels with the neutral amino acid, alanine.

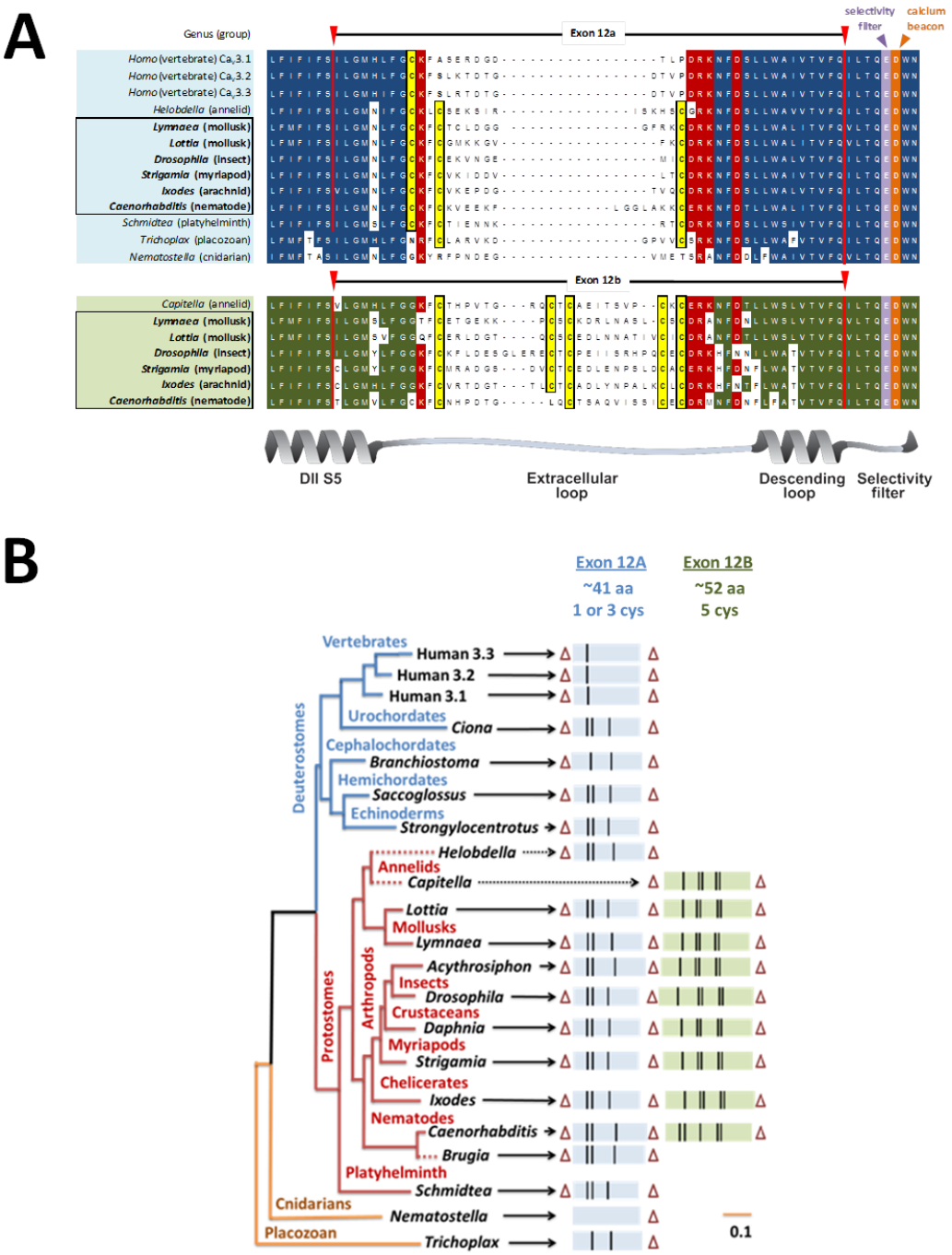

Figure 3.10. Phylogeny and sequence alignment of exon 12 across species.

(A) Aligned amino acid turret sequences for exon 12a, 12b and hCav3 turrets. Conserved cysteine residues are highlighted (B) A phylogentic tree illustrating the conservation of exon 12a (in blue exons) and 12b (in green exons), vertical black lines depict the location of cysteine residues in the exons. Triangles indicate introns.

3.2 Cysteine substitution alters LCav3 channels properties

The presence of a conserved pattern of extracellular cysteines in the Domain II turret suggests that the cysteines contribute a specifically organized structure above the membrane pore of T-type channels. Interdomain disulphides contribute to an "extracellular cap" that has been determined in the crystal structure in K_{2P} two pore potassium channels above the pore of K_{2P} channels (Miller & Long, 2012). T-type channels likely have an analogous extracellular cap structure above T-type channels. Insights into a possible turret cap structure can be inferred by the conservation pattern of cysteines in the turret domains of T-type channels. An alignment in Figure 3.11 of the four Domain turrets are shown for all snail cation channels, such as NALCN, (LNALCN), sodium channels: (LNav1, LNav2), calcium channels (LCav1,LCav2,LCav3), human T-type channels (Cav3.1,Cav3.2,Cav3.3) and the simplest unicellular eukaryotes to contain a voltage-gated cation channel are the apusozoan (*Thecamonas trahens*) and the coanoflagellate (*Monosiga brevicollis*). All cation channels in figure 3.11, including unicellular organisms, have a conserved set of cysteine residues with four cysteines in Domain I (D1-1, D1-2, D1-3, D1-4), none in Domain II, two in Domain III (D3-1, D3-2) and two in Domain IV (D4-3, D4-4), however this does not apply to T-type calcium channels. Technically the conserved cysteines in Domain IV are outside the extracellular turret, but they are conserved in all voltage-gated cation channels. The only voltage-gated cation channels that break the 4-0-2-2 arrangement of eight cysteines are some vertebrate sodium channels and all T-type channels, which have many additional cysteines. T-type channels have an extra two cysteine residues in Domain I (D1-5, D1-6), two extra cysteines in Domain III (D3-1,D3-2), and two extra cysteines in Domain IV (D4-1, D4-2). Vertebrate T-type channels have an additional cysteine in Domain II, with a 6-1-2-4 arrangement of 13 cysteines. Invertebrates have more cysteines than the vertebrate T-type channels. There are more cysteines in Domain II as a tricysteine turret (exon 12a) or pentacysteine turret (exon 12b) and two additional cysteines in Domain IV, for a 6-(3or5)-2-6 arrangement of 17 or 19 cysteines for exon 12a or exon 12b respectively. It seems conceivable that the Domain II turret cysteines interact and form an extracellular cap structure with interdomain disulphide bonds with unique T-type channel cysteines in Domain IV. Mammalian T-type channels with a unicysteine arrangement in Domain II, likely form a different folded structure than the invertebrate T-type channels.

To evaluate the role cysteine residues play in ion selectivity and permeability, novel turrets with substituted cysteines with alanines were created, with the exception of leaving a single cysteine in the position that resembled the conserved cysteine in mammalian T-type channel turret in Domain II. Mutated cysteine residues were introduced by cassette insertion of a purchased synthetic gene, insert sizes of ~200 base pairs (bp) (Biobasic) between AvrII-AfeI restriction sites introduced by Quikchange mutagenesis onto a subcloned 3kb plasmid (between BglII – SalI) restriction sites from snail LCav3 T-type channel. These mutations will be denoted as LCav3-12a ΔC and LCav3-12b ΔC, whereas the original LCav3 channels are known as wild type. It should be noted that LCav3-12a contained four cysteines in its turret region and three of these cysteines are highly conserved, however, for the mutant channel, all cysteines except the cysteine conserved in mammals were mutated. All expressed plasmids were confirmed by sequencing at TCAG DNA Sequencing Facility at Sick Kids Hospital, Toronto.

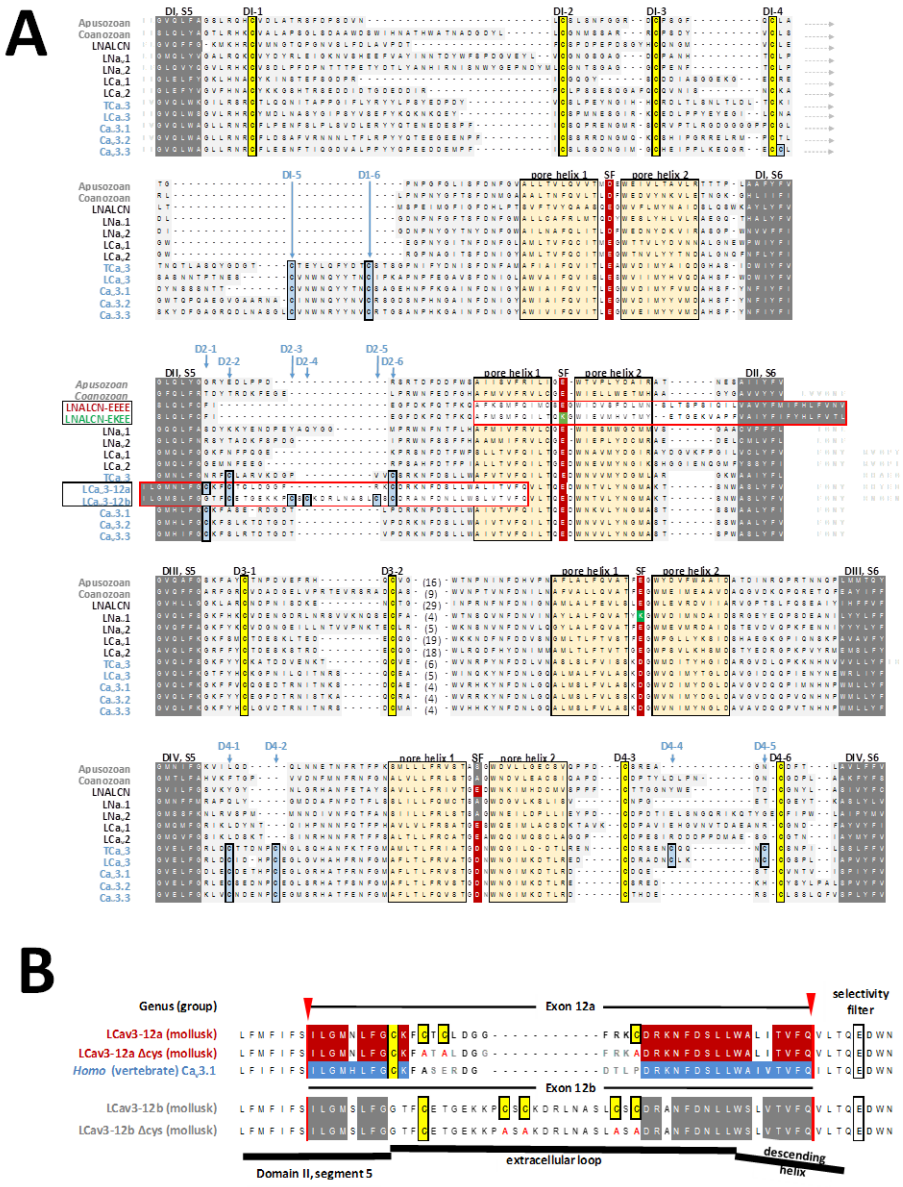

Figure 3.11. Sequence alignment comparisons of turret regions for conserved cysteines in domains I- IV.

(A) Alignments of domain I-IV showcasing S5-turret-descending helix- selectivity filter- ascending helix-S6 for four domain cation channels. Conserved cysteine residues are highlighted in yellow boxes, the conserved selectivity filter is in red/grey, and light beige boxes illustrates the descending and ascending helix. (B) Comparison of sequence alignment of LCav3-12, LCav3-12ΔC, and hCav3.1 amino acids in exon 12, cysteine residues are selected in yellow. Conserved cysteines were substituted with an alanine residue in LCav3 - 12 ΔC channels. TCav3 refers to the Cav3 channel in *Trichoplax adhaerens*.

3.2.1 Basic biophysical properties for LCav3 ΔC mutations

Identical protocols and external and internal solutions as wild types were carried out on the LCav3-12 ΔC mutations. Evaluation of biophysical kinetics revealed a statistically significant change in activation for LCav3-12a and LCav3-12a ΔC, with a 5 mV shift to the left, but not a significant change with LCav3-12b ΔC and LCav3-12b. Steady state inactivation did not change significantly between LCav3-12a and LCav3-12a ΔC but a statistically significant change was seen in LCav3-12b ΔC and LCav3-12b with a ~5 mV shift to the right. Other differences include a faster time to peak for LCav3-12a ΔC, but slower time to peak in LCav3-12b ΔC compared to their wild type counterparts. LCav3-12a ΔC has a faster inactivation than LCav3-12a. Inactivation of LCav3-12b ΔC is slower at more negative voltages but is faster at higher voltages than LCav3-12b. Deactivation kinetics are significantly faster in the mutants and the mutants take longer to recover from inactivation. Table 8 summarizes the biophysical kinetics of LCav3-12a ΔC and LCav3-12b ΔC. The kinetics changes for exon 12a and 12b in the cysteine mutants do not resemble each other, while the wild type versions do resemble each other. There are statistically significant differences in the biophysical properties of the cysteine mutants but neither are these differences are very striking and there is no obvious trend to their deviations from the wild type condition. The lack of consistency and dramatic change suggest that the changing kinetic features in the mutants is a secondary feature of dismantling the cysteine framework in extracellular turrets.

A more striking feature in these mutants are a much larger outward current with cesium as the charge carrier than their wild type counterparts. Both LCav3-12a ΔC and LCav3-12b ΔC exhibit similar large outward monovalent ion currents (Figure 3.12) suggesting they are highly permeable to monovalent ions.

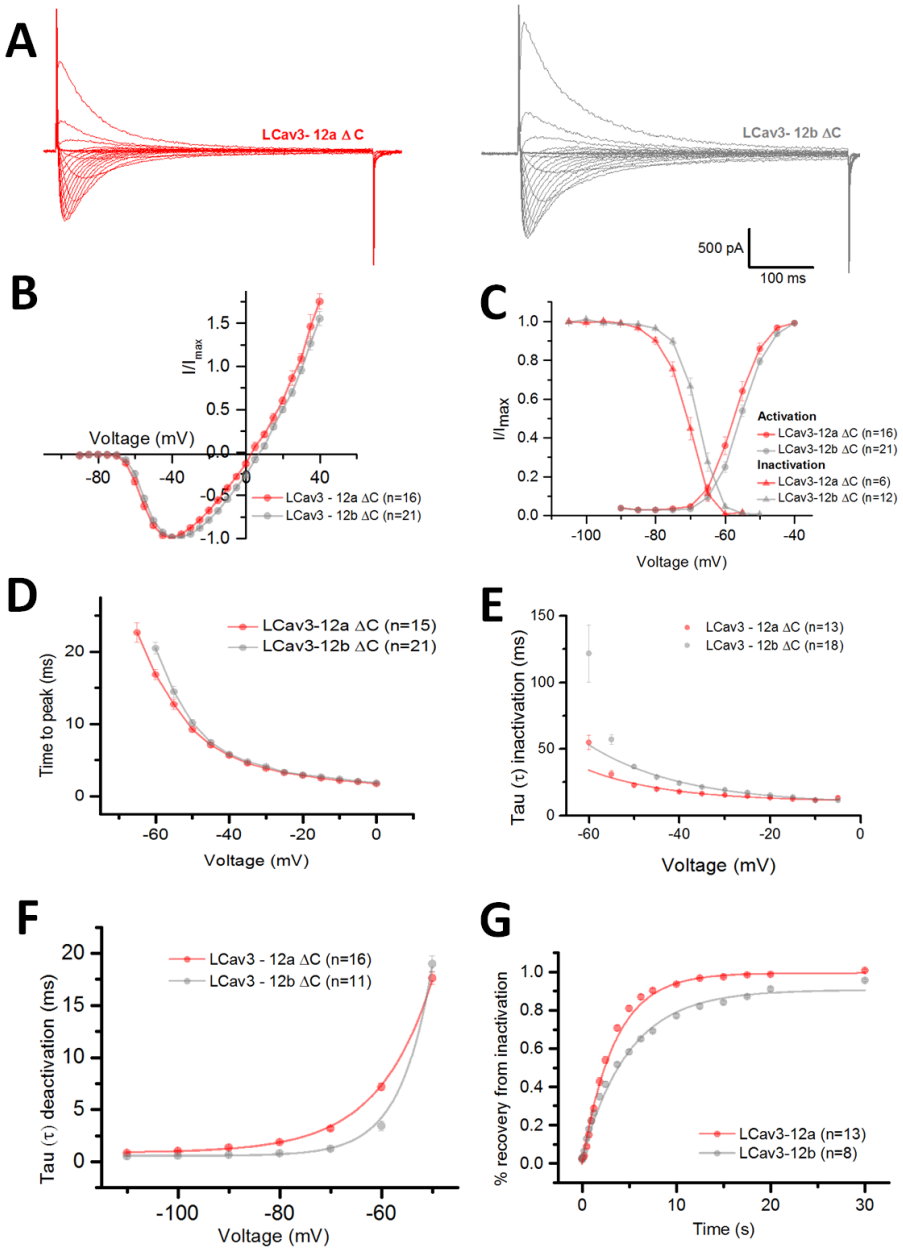

Figure 3.12. Biophysical kinetics of LCav3 mutants lacking cysteines in domain II.

(A) Representative traces of LCav3-12a ΔC and LCav3-12b ΔC from a holding potential of -110 mV. Large outward currents are elicited from both mutants indicating an increase in ion permeability. (B) Current-voltage relationship; outward currents are significantly larger than their wild types and reversal potentials are negatively shifted. (C) Activation and steady state inactivation curves; LCav3-12a ΔC is negatively shifted. (D) Time to peak in milliseconds. LCav3-12b ΔC is slower at negative voltages. (E) Tau inactivation values, LCav3-12b ΔC is significantly slower than LCav3-12a ΔC at negative voltages. (F) Tau deactivation, LCav3-12a ΔC is slower to deactivate than LCav3-12b ΔC. (G) Recovery from inactivation is slower in mutants than their counterparts, while LCav3-12b ΔC is slower than LCav3-12a ΔC.

Table 8. Biophysical kinetics of LCav3- 12 ΔC mutants

	LCav3 - 12a ΔC	n	LCav3 - 12b ΔC	n	aΔC /bΔ C	aΔC / WT-a	bΔ C/ WT-b	aΔC /WT-b	bΔ C/ WT-a
Activation									
$V_{1/2}$	-57.35 ± 0.84	16	-55.86 ± 0.51	21	n.s.	**	n.s.	**	n.s.
K	3.31 ± 0.093	16	3.25 ± 0.096	21	n.s.	**	**	**	**
Peak of IV	- 40 mV	16	-40 mV	21					
Inactivation									
$V_{1/2}$	-71.62 ± 0.78	16	-66.50 ± 0.57	12	**	n.s.	**	n.s.	n.s.
K	3.30 ± 0.068	16	2.97 ± 0.06	12	**	*	n.s.	**	**
Activation kinetics									
TTP -55 mV (ms)	12.72 ± 0.73	15	14.46 ± 0.78	21	n.s.	**	**	**	**
TTP -10 mV (ms)	2.19 ± 0.077	15	2.4 ± 0.076	21	n.s.	**	**	**	**
Inactivation kinetics									
τ -55 mV (ms)	31.14 ± 2.49	13	57.03 ± 3.51	18	**	n.s.	**	*	**
τ -10 mV (ms)	11.41 ± 0.28	13	11.6 ± 0.37	18	n.s.	**	**	**	**
Deactivation									
τ -100 mV (ms)	1.02 ± 0.050	16	0.55 ± 0.030	11	**	**	**	**	**
τ -60 mV (ms)	7.17 ± 0.37	16	3.40 ± 0.44	11	**	n.s.	**	**	**
Recovery from Inactivation									
%recovery at 0.25s	4.0 ± 0.0040	13	6.36 ± 0.0071	8	**	**	n.s.	n.s.	*
% recovery at 5s	80.85 ± 0.013	13	58.20 ± 0.010	8	**	**	*	**	**
$T_{0.5}$ (ms)	1481.19 ± 64.60	13	2492.6 ± 85.75	8	**	**	*	**	**

Values are expressed as means ± standard error mean (S.E.M) and *n* denotes the number of recordings performed for each data set. Statistical comparisons were performed using a one-way ANOVA combined with a Student-Newman-Keuls *post hoc* test in SPSS with * $p < 0.05$, ** $p < 0.01$ and n.s., not significant. It should be noted, WT stands for wild type.

3.2.2 LCav3 ΔC mutations become more permeable to monovalent ions

LCav3-12 ΔC mutations exhibit a large outward current from internal cesium, suggesting a high monovalent ion permeability for these mutants. As predicted, the mutations are significantly more permeable to sodium ions when 135 mM NMDG is replaced with equimolar 135 mM sodium in the presence of 2 mM calcium. LCav3-12a ΔC generated a 19.83 ± 0.71 fold increase in the presence of sodium compared to LCav3-12a with a ~15 fold. LCav3-12b ΔC produced a 3.42 ± 0.14 fold increase compared to a 2-fold increase of its wild type counterpart. See Figure 3.13 for comparisons of relative fold change in current sizes.

As previously shown, we can use the bi-ionic reversal potential experiments to measure the relative permeabilities of inward flow of calcium ions with respect to the outward monovalent ions. LCav3-12a ΔC has relative permeabilties of 13, 17, 19 and 39 for Li^+, Na^+, K^+ and Cs^+ respectively. LCav3-12b ΔC has higher relative permeabilities for monovalent ions of 15, 23, 26 and 34. The relative permeabilities for monovalent ions compared to calcium ions is significantly more than wild type LCav3-12a or LCav3-12b. It is interesting to note, wild type LCav3-12a is more permeable than LCav3-12b ΔC with a 15- fold increase in sodium current versus a 4-fold increase, yet relative permeabilties of LCav3-12b ΔC calculated by the bi-ionic reversal potential experiments indicates LCav3-12b ΔC is more permeable than LCav3-12a. In the native case, inward calcium and sodium currents are filtered through the cysteine turret framework from outside the channel, and then compete for inward passage for binding sites through the pore selectivity filter. A significant difference in the bi-ionic reversal experiments is that the driving force and direction for ion flow of the monovalent ion is now in the opposite directions (inward to outward) compared to the influx of calcium ions, and the outward monovalent ion currents are not encountering the extracellular turret that pre-filters their ion passage until after they pass through the ion selectivity filter. Thus the relative permeabilities calculated with the cysteine mutations using the bi-ionic reversal experiments, is likely not an accurate reflection of the relative permeability of sodium ions as an inward current competing with inward calcium ions. The calculated relative permeability change are more dramatic than expected for the cysteine mutations, which likely reflect the greater impact of the outward monovalent ion current compared to when they are inward currents competing as inward currents with calcium ions.

Another striking feature obtained is the convergence of outward slope conductance in internal Li^+, Na^+ and K^+ ions for the mutations at high voltage potentials (+80mV), showing no significant difference between LCav3-12a ΔC and LCav3-12b ΔC, with the exception of cesium, see Figure 3.14 for comparisons. Outward slope conductance for LCav3-12a ΔC is 0.090, 0.1, 0.12 and 0.048 for Li^+, Na^+, K^+ and Cs^+ respectively, similar values were observed with LCav3-12b ΔC with 0.095, 0.10, 0.096 and 0.52. Reversal potentials are negatively shifted by 5-10 mV in LCav3 channels lacking cysteines from their wild type counterparts, and the reversal potentials differ depending on the monovalent ion present, suggesting that the pore discriminates between different monovalent ions. The convergence of outward currents at high voltages, likely reflects a saturation of maximal conductances in these cysteine mutants. There is a maximal driving force for outward current flow at steps to extremely positive potentials (+80 mV) and where the outward monovalent ion currents are not competing with any inward calcium currents at these extremely positive potentials. Only the largest of the ions, cesium does not saturate their outward currents to this maximal conductance level. The saturation of conductances with Li^+, Na^+ and K^+ suggest that the cysteines in the outer turret normally limit outward monovalent ion conductances, and the removal of this outer cysteine framework allows a maximal whole cell conductance to be achieved. See Figure 3.15 for values and comparisons of mutant LCav3 channels with its wildtype.

Turrets with a reduced number of cysteines have a lowered capacity to block the sodium current with 10 μM calcium ions, where inhibition of the current drops from 44% to 21% and 81% to 72% of the total current in cysteine mutants of exon 12a and 12b, respectively in the anomalous mole fraction effect experiments (see Figure 3.16). The change in fold current from 10 μM to 10 mM external calcium ions, reflects a similar trend, where there is a more exaggerated monotonic decline in calcium current from 6.9 to 7.7 fold drop in current size and 2.1 to 2.5 fold drop in current size in LCav3 channels with cysteine mutations in exon 12a and 12b, respectively. Over the same range of calcium concentrations increasing from 10 μM to 10 mM, there is a 9.1, 7.9 and 5.9 fold increase in calcium current for human Cav3.1, Cav3.2 and Cav3.3 channels, reflecting their higher permeation rates for calcium ions at physiological mM levels, compared to the low permeability for calcium ions for snail channels, especially those with the cysteine mutations.

Most of the intervening amino residues between the cysteine framework in the extracellular turret are highly variable between species containing exon 12a and 12b. This means that the size and arrangement of cysteines are the likely critical features that are responsible for the altered monovalent ion permeation of snail T-type channels. These are critical amino acids, and there are only 7 and 8 amino acid changes that exist between the highly sodium permeable LCav3-12a with LCav3-12a ΔC channel and the calcium selective hCav3.1 channel for exon 12.

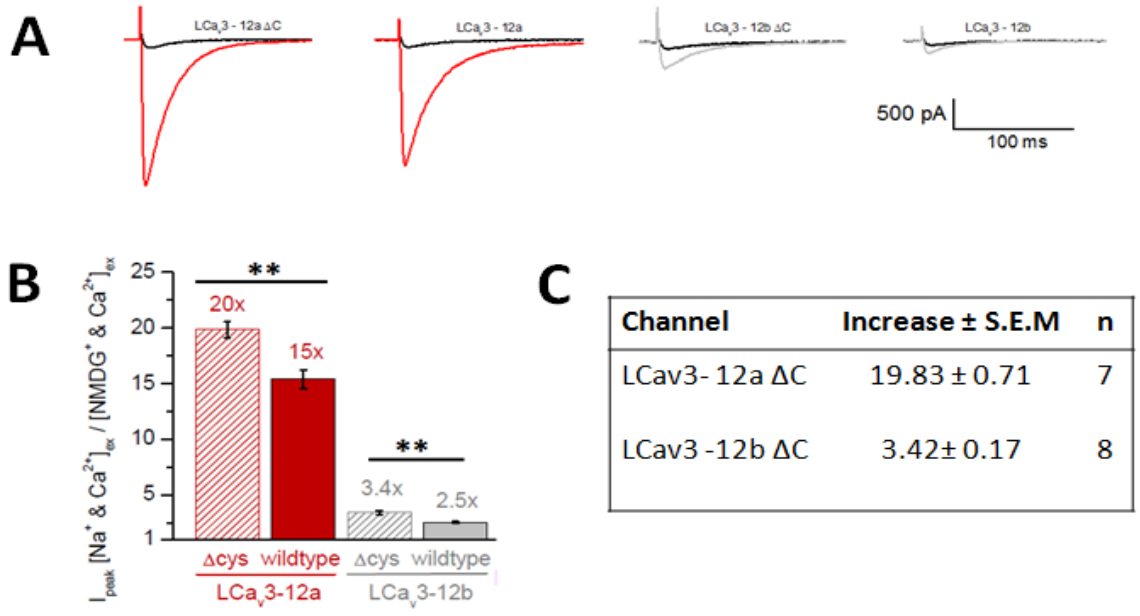

Channel	Increase ± S.E.M	n
LCav3- 12a ΔC	19.83 ± 0.71	7
LCav3 -12b ΔC	3.42± 0.17	8

Figure 3.13. LCav3-12 ΔC are more permeable to 135 mM external sodium than their counterparts.

(A) Sample traces of 2 mM calcium and 135 mM NMDG (shown in black) replaced with 2 mM calcium and 135 mM sodium (red/gray). Channels are organized from most permeable to least, LCav3-12a ΔC > LCav3-12a > LCav3-12b ΔC > LCav3-12b. (B) A bar graph illustrating the relative fold increase in current size, a Student t-test was perform between LCav3-12a ΔC and LCav3-12a, and LCav3-12b ΔC and LCav3-12b. ** p <0.01. (C) Average fold change for LCav3-12a ΔC and LCav3-12b ΔC , mean ± standard error means (S.E.M.), *n* refers to the number of recordings per set.

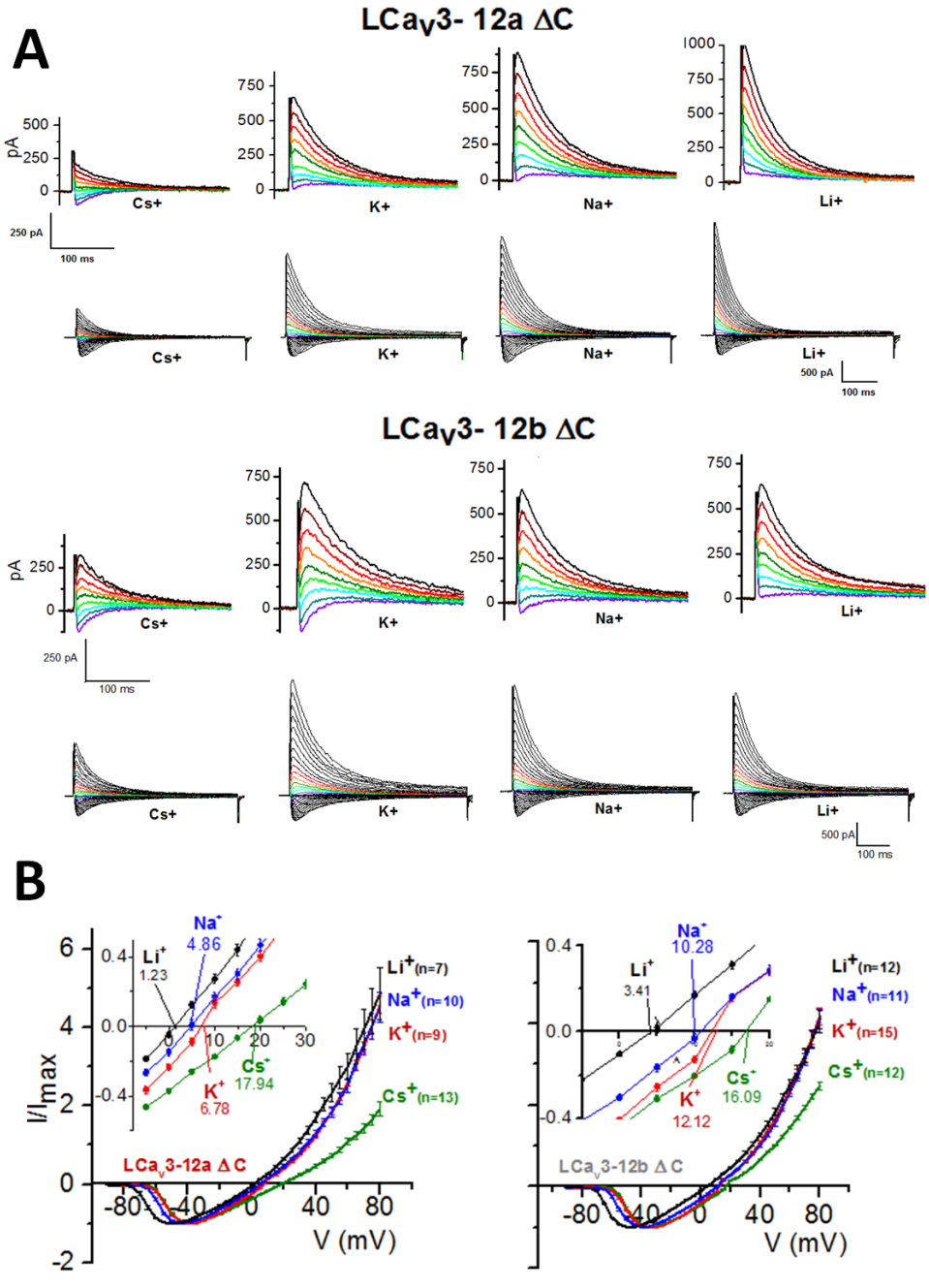

Figure 3.14. Monovalent ions are more permeable in LCav3 mutations lacking cysteines.

(A) Representative traces of 4 mM external calcium with outward monovalent T-type currents generated from 100 mM internal Li^+, Na^+, K^+ and Cs^+ ions in LCav3-12ΔC mutants (B) A current-voltage (IV) relationship, Li^+, Na^+ and K^+ ions have convergent slopes at +80 mV. *n* values are shown in parentheses. A close up of currents crossing the reversal potential is shown within the IV curve (inset).

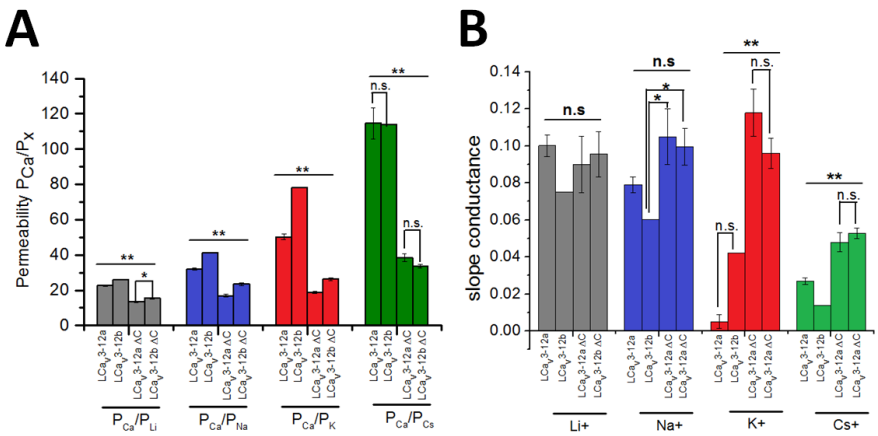

C

Reversal Potentials (E_{rev})

	Li^+	SEM	n	Na^+	SEM	n	K^+	SEM	n	Cs^+	SEM	n
E_{rev} LCav3-12a ΔC	1.23	0.53	7	4.87	0.76	10	6.78	0.55	9	17.94	0.86	13
E_{rev} LCav3-12b ΔC	3.41	0.58	12	10.28	0.65	11	12.12	0.43	15	16.09	0.55	12

Relative Permeability (P_{ca}/P_x)

	P_{Ca}/P_{Li}	SEM	n	P_{Ca}/P_{Na}	SEM	n	P_{Ca}/P_K	SEM	n	P_{Ca}/P_{Cs}	SEM	n
$P_{Ca/Px}$ LCav3-12a ΔC	13.47	0.42	7	16.87	0.77	10	18.85	0.66	9	38.60	2.15	13
$P_{Ca/Px}$ LCav3-12b ΔC	15.40	0.51	12	23.41	0.92	11	26.21	0.71	15	33.78	1.06	12

Slope Conductance

	Li^+	SEM	n	Na^+	SEM	n	K^+	SEM	n	Cs^+	SEM	n
Outward g_x LCav3-12a ΔC	0.090	0.015	7	0.10	0.015	10	0.12	0.012	9	0.048	.0052	13
Outward g_x LCav3-12b ΔC	0.095	0.012	12	0.1	0.01	11	0.096	0.008 1	15	0.052	.0029	12

Figure 3.15. Relative permeability ratios and slope conductances of LCav3-12 ΔC.

Statistical comparisons were performed using a one-way ANOVA combined with a Student-Newman-Keuls *post hoc* test in SPSS with * $p < 0.05$, ** $p < 0.01$ and n.s., not significant. A black line over the entire group set indicates the p value between each group, unless otherwise labeled differently. (A) A bar graph comparing relative permeability ratios between LCav3 channels with domain II turret cysteine mutations versus wild type. (B) Comparison of slope conductances. (C) Average values for reversal potentials, relative permeability and slope conductance for LCav3 - 12ΔC channels, with their standard error mean (S.E.M) and *n* denotes the number of recordings.

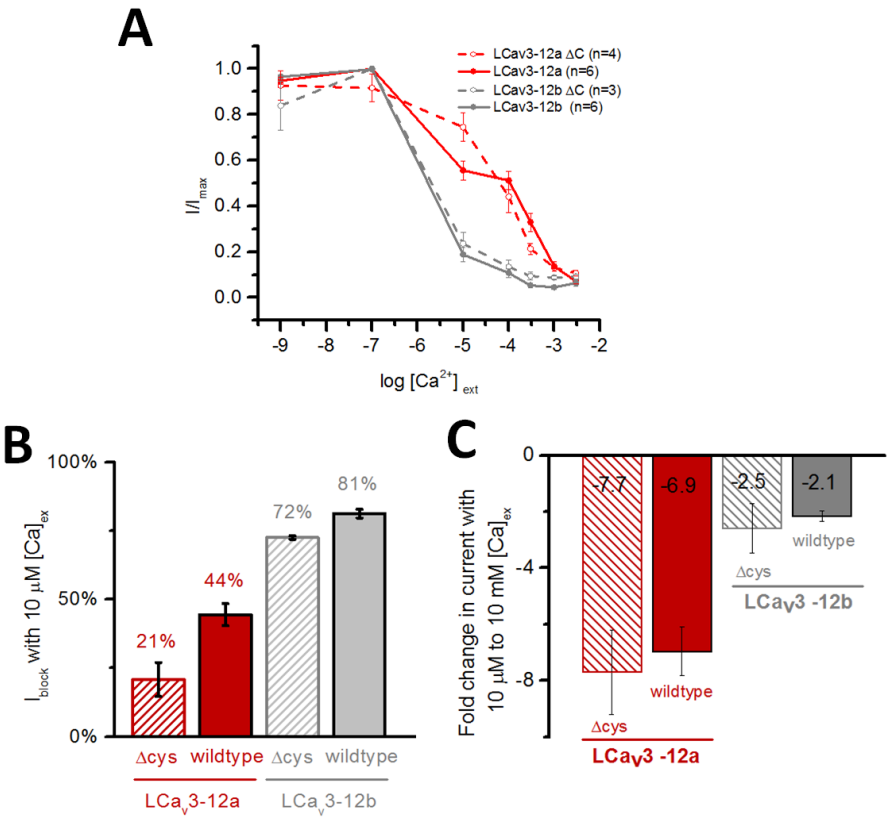

D

log $[Ca^{2+}]_{ext}$	LCav3- 12a ΔC % current block	SEM	n	LCav3- 12b ΔC % current block	SEM	n	SNK *post hoc* results 12A ΔC /12A	12B ΔC /12B	12A /12B	12A ΔC /12B ΔC
-9	1.74	2.14	4	0.92	2.61	3	n.s.	n.s.	n.s.	n.s.
-7	0	0	4	0	0	3	n.s.	n.s.	n.s.	n.s.
-5	20.81	6.22	4	72.49	0.62	3	**	n.s.	**	**
-4	48.32	2.97	4	84.23	2.05	3	n.s.	n.s	**	*
-3.52	72.25	5.71	4	90.32	3.21	3	*	n.s.	**	**
-3	86.45	1.08	4	91.88	0.51	3	n.s.	n.s.	**	n.s.
-2.25	90.38	0.80	4	91.78	1.15	3	n.s.	n.s.	n.s.	n.s.
-2	91.22	0.44	4	90.80	3.20	3	n.s.	n.s.	n.s.	n.s.

Figure 3.16. Comparison of the anomalous mole fraction effect in snail LCav3 exon 12 channels.

(A) A comparison of LCav3-12 ΔC channels with LCav3 with exon 12 with increasing block of 60 mM sodium, with increasing external calcium, ranging from 10^{-9} to 10^{-2} M. (B) A bar graph depicting the weaker block of calcium ions at 10 µM in LCav3 lacking cysteines. (C) A greater decline in current size from 10 µM to 10 mM external calcium in LCav3-12 ΔC. (D) A summarized table presenting the average block at varying calcium concentrations, with standard errors of the mean (S.E.M). *n* denotes the number of recordings. Statistical comparison using the Student-Newman Keuls (SNK) *post hoc* test was performed, * $p<0.05$, ** $p<0.01$ and n.s. is not significant.

3.2.3 Kinetic and ion permeability changes when barium is the charge carrier.

Barium as a charge carrier defines the nonmenclature system used to identify calcium channels. T-type calcium channels are known as tiny and transient in the presence of barium. Barium currents are always larger than calcium currents in high voltage-activated Cav1 and Cav2 channels (Zamponi, 2005). The sticky pore hypothesis suggest that there is a higher affinity calcium binding site in calcium channels and in the presence of barium, the rate of permeation is lower due to a weaker affinity for barium ions (Sather & McCleskey, 2003).

Current sizes with barium can be measured when 2 mM external calcium is replaced with equimolar barium. LCav3 with exon 12a and 12b have a consistent ~1.3 fold increase when barium is present. However, LCav3 with exon 12 lacking cysteines have ~0.5 fold decrease in current size, as seen in Figure 3.17A. The greater barium currents of LCav3 channels resembles hCav 3.2 T-type channels, while the larger calcium currents compared to barium currents for LCav3-12 ΔC resembles the reduced barium permeability for native hCav 3.1 channels (Shcheglovitov, Kostyul, & Shuba, 2007). Furthermore, barium ions positively shifts the peak current of LCav3-12 ΔC mutations compared to calcium currents, yet the IV curves are unchanged with barium and calcium currents in wild type LCav3 channels (Figure 3.17B).

There appears to be more at play than just a diminution of the size of barium currents relative to calcium currents when cysteines are mutated in the pore of Domain II. A major observation is that inward barium currents in cysteine mutated channels exhibit a strange behavior in the presence of monovalent ions, either in the presence of inward or outward monovalent ion currents. The monovalent ion in standard recording conditions is high cesium concentration (100 mM) in the pipette. With calcium as the charge carrier on the outside of the membrane, the inward calcium current reduces from a maximum at peak current (-40 mV) to a minimum at the reversal potential where the driving force is minimal for calcium ion entry. Beyond this, is a fluid transition to outward cesium currents increasing in size of outward currents as the driving force increases above a particular reversal potential that reflects the relative permeabilities of inward calcium and outward cesium conductances. Barium currents diminish from a maximum peak current at -40 mV, but there is very strange behavior in the transition zone approaching the reversal potential at step depolarizations starting at -20 mV. A single reversal potential point is not apparent for the combination of outward cesium and inward barium currents. As barium currents are reduced towards the reversal potential, outward currents

are observable as slower components of the recording, which grow in size from steps from -20 mV, -10mV and 0 mV as the driving force increases for outward cesium exit, see figure 3.18A. Unlike calcium as the charge carrier, inward barium flux do not impede the outward current flow in this transition of potentials where both inward barium and outward cesium currents are evident. This suggests that delta cysteine mutations have altered the channel structure to accommodate both the simultaneous flow of barium and monovalent ions at the same time, with both ions capable of transitioning almost independently through the pore.

Kinetics do not change for LCav3-12a or LCav3-12b channels when cysteines are not mutated in Domain II turret when calcium is the charge carrier. When barium is present, wild type 12a and 12b exhibit faster tau inactivation, but continue to resemble one another. Time to peak is slower in LCav12a and faster for LCav3-12b when barium is present. Mutations of cysteines in LCav3-12a or LCav3-12b channels also have altered barium current kinetics, where they assume much faster kinetics for activation and inactivation. The faster time to peak and tau inactivation are shown in Figure 3.18 B, C.

The independent flow of barium currents and monovalent ions is evident in a context where sodium currents are inward currents. We examined the permeability of sodium ions in the presence of either external 2 mM calcium or barium using a ramp starting from a holding potential of -110 mV to + 100 mV in 1 second. As expected, there was increase in current size after replacing extracellular 100 mM NMDG with equimolar extracellular sodium ions in the presence of 2 mM extracellular calcium ions, and this size increase is greater for 12a ΔC and 12b ΔC channels than their wild type channels because of the greater monovalent ion permeation of cysteine modified snail LCav3 channels.

However, when barium was the charge carrier, two humps are noticeably visible in currents elicited by ramp, that was not observed when calcium is the charge carrier, as seen in Figure 3.19A. Overlay of the calcium and sodium current in LCav3-ΔC with barium and sodium ramp recordings suggest that the difference in the ΔC channels is the presence of a rightmost, more depolarization activated hump, that contains the barium current. In 12b- ΔC, the leftmost, sodium-containing hump is smaller than the larger rightmost, barium hump, in proportion to the lowered sodium permeation of 12b channels. The 12a-ΔC channels have a larger, leftmost, sodium-containing hump than the barium containing rightmost hump, which reflects the greater permeation of sodium ions compared to barium ions in 12a- ΔC compared to 12b- ΔC channels.

See Figure 3.19B for double hump analysis. It is possible that this effect is occurring in the presence of calcium, as evident by a slight hump in LCav3-12b ΔC, but it is masked by the high affinity binding site for calcium and the large increase in current size due to high sodium permeation in LCav3-12a ΔC. The outcome of the ramps were not observed in mammalian Cav3 channels or snail LCav3 with cysteine residues present as explained in a previous section of this thesis.

The independent flow of monovalent ions in the presence of barium is evident in previous experiments (Figure 3.18) illustrating that outward cesium currents moved relatively independently from inward barium currents at potentials approaching the reversal potential when both barium inflow and cesium outflowing ions were both substantial currents. Here, in voltage ramp studies, monovalent sodium and barium ions are both inward, and the cysteine mutants reflect the observed weakened capacity for barium ions to interfere with the inflowing sodium ions, creating conditions where barium and sodium ions are transiting almost independently through the T-type channel when the cysteine residues in Domain II are modified.

The data clearly indicates that the mutations of the cysteine framework outside the Domain II turret has minor effects on the biophysical parameters. A major consequence of altered cysteine residues of LCav3 channels containing the tricysteine turrets with exon 12a and pentacysteine turrets with exon 12b, is the permeation of divalent and monovalent ions. To summarize the effect we see comparing cysteine mutated turrets with wild type LCav3 channels: 1) inward sodium currents are much larger in the presence of calcium ions; 2) The outflow of monovalent ions is so substantial through the cysteine mutated channels that the whole cell conductance can saturate with steps to very high potentials. Thus, differing sized monovalent cations such as Li^+, Na^+ and K^+ with different permeation rates, are equal and are moving through the T-type channels at a maximal set saturation rate and 3) The monovalent ion permeation is so unhampered by the presence of divalent cations, we observe the outflowing or inflowing of monovalent ions, moving semi-autonomously through the pore while barium ions are. The mechanism where alterations of the cysteine turret, increases monovalent ion permeation and weakens the ability of divalent cations (like barium ions to block the current) may reflect a much wider pore or introduction of a completely separate ion conduction pathway which would accommodate the simultaneous, independent flow of divalent and monovalent ions. The K_{2P} channels which has a similarly enlarged turret, forms an extracellular cap structure. This

cap produces side portals with charged residues that would screen and pre-filter the ions which would be accessible to the selectivity filter below (Miller & Long, 2012). Our observations from the differences in the behavior of outflowing versus inflowing monovalent ions in the presence of calcium influx, is consistent with the hypothesis that the ion pore is not symmetrical, and that the extracellular turret may bias the ion flow to alter the inward ion flux, that is not consistent with its behavior as outward ion flux.

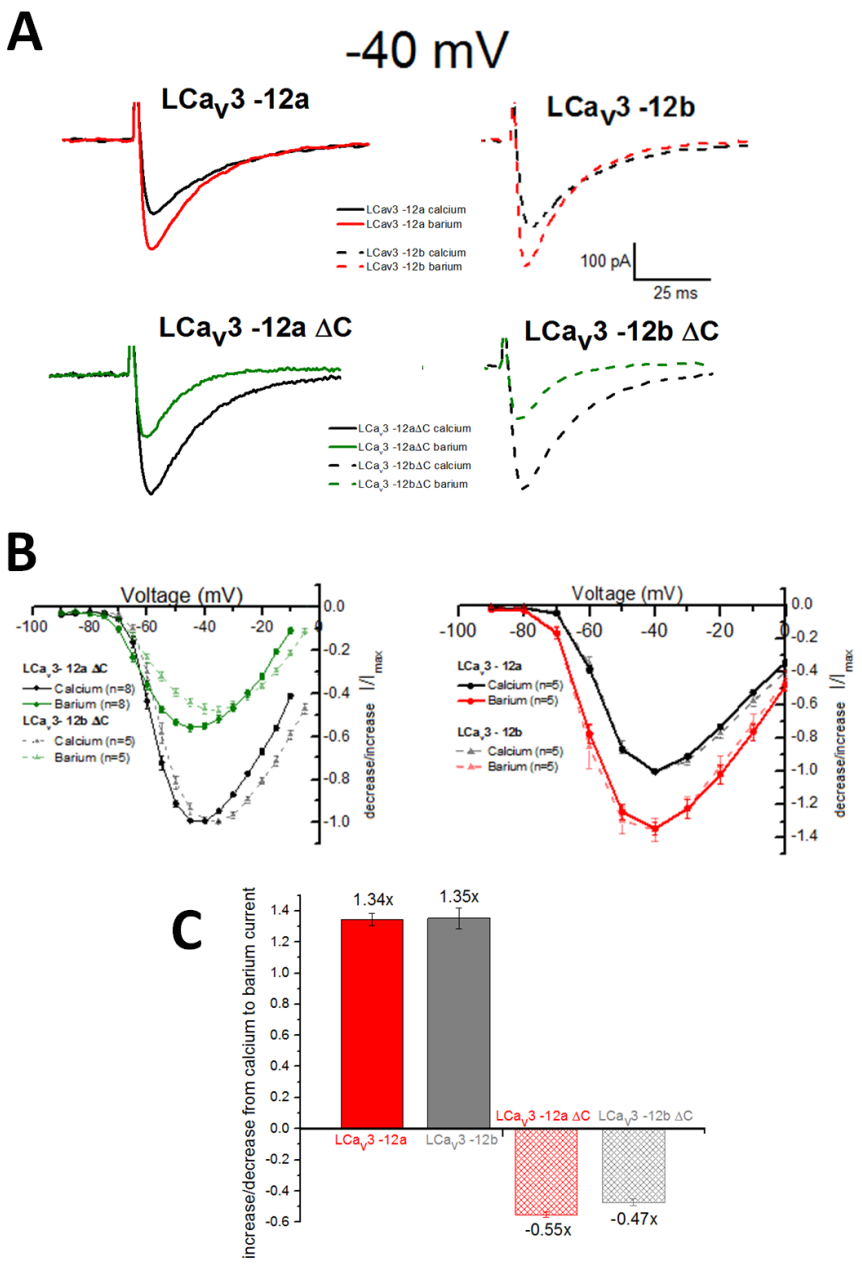

Figure 3.17. Barium currents are smaller in current size compared to calcium currents for LCav3 channels lacking cysteines in the Domain II turret.

T-type currents are generated from a holding potential of -110 mV and depolarized from -90 mV to +40 mV in 5 mV or 10 mV increments. (A) Peak current traces at -40mV increase ~1.3x for wild type LCav3 (red trace) and decrease ~0.5x for LCav3-12 ΔC (green traces). (B) Current-voltage relationships; reversal potentials cannot be accurately measured when barium is the charge carrier. (C) A bar graph illustrating the relative fold increase/decrease in current size when barium is present. No statistical analysis was performed.

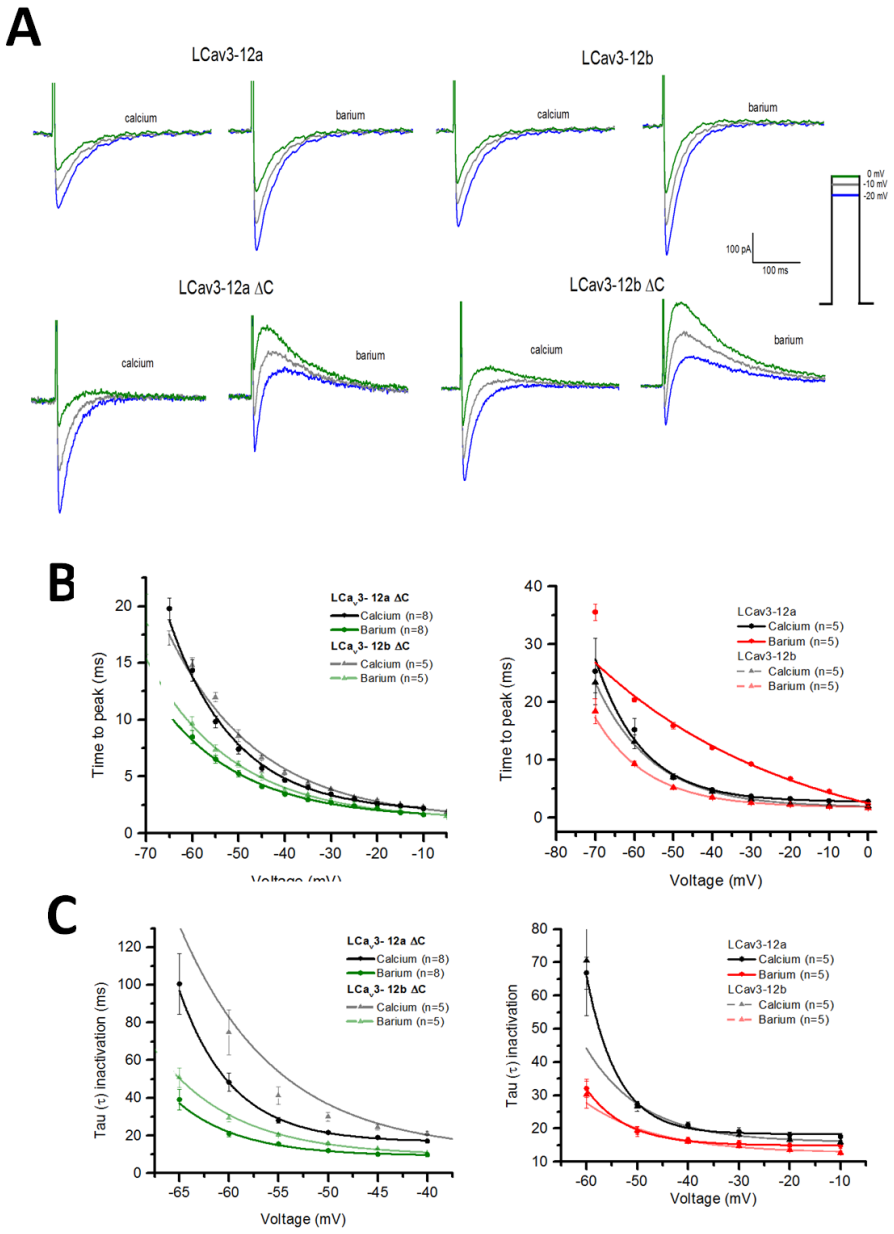

Figure 3.18. Comparison of barium and calcium inward currents and activation properties in LCav3 and LCav3-12 ΔC channels.

(A) Current traces of calcium vs. barium showing the influx of these ions in LCav3 and LCav3-12ΔC channels. LCav3-12ΔC generate a simultaneous inward and outward current in the presence of barium ions between -20 to 0 mV, this behavior is absent in wild type LCav3 channels. (B) Time to peak values in milliseconds with their standard error mean is shown for LCav3-12ΔC (left) and LCav3(right) channels in calcium or barium ions. (C) Tau inactivation in ms for LCav3-12ΔC (left) and LCav3 (right) in the presence of barium or calcium ions. All channels have faster tau inactivation in the presence of barium. No statistical analysis was performed.

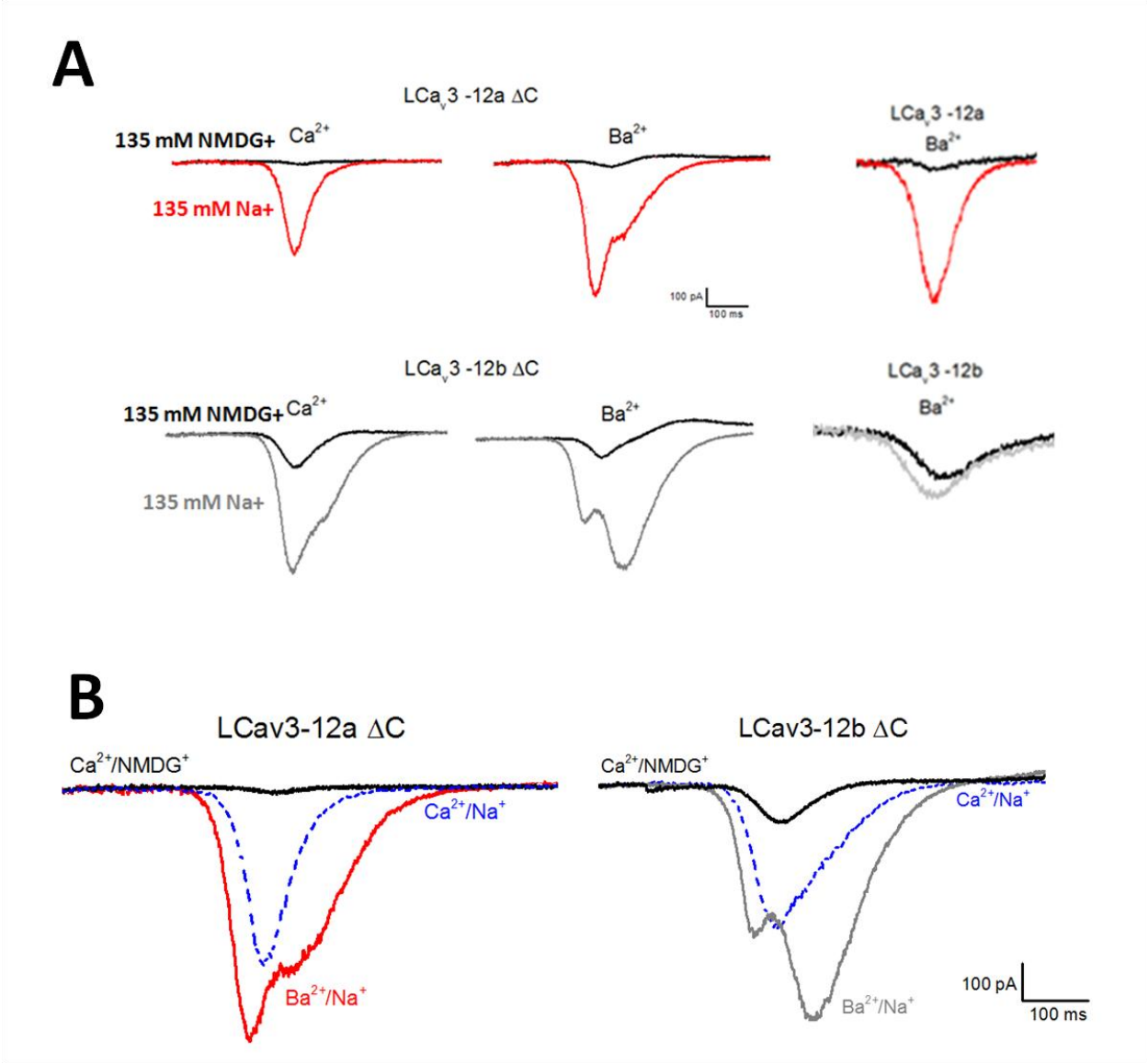

Figure 3.19. Comparison of calcium and barium humps in LCav3 channels.

(A) LCav3-12a channels (top) and LCav3-12b channels (bottom) generates a large inward ramp current when 2 mM Ca^{2+} /Ba^{2+} with 100 mM NMDG is replaced with equimolar sodium. In the presence of barium ions, LCav3 – ΔC channels produce a double hump that is not seen in wildtype LCav3 channels. (B) An overlap of LCav3 – ΔC in calcium and barium ions provides a closer inspection of the double hump behavior. The calcium/sodium hump matches the leftmost hump seen when barium is the charge carrier, suggesting it the left hump is produced by sodium ions while the right is generated by barium. No statistical analysis was performed.

3.2.4 LCav3 ΔC mutations are more sensitive to divalent metal ions

Nickel and zinc are common divalent metal cations that have affinity and discriminating power for separating T-type calcium channel currents. We investigated the inhibitory effects of these metal cations on LCav3 channels expressed in HEK293T cells. Nickel blocks LCav3 with exon 12b at a 50% inhibitory concentration (IC_{50}) of ~300 μM (Senatore & Spafford, 2010). In contrast, nickel is a ~10-fold more potent blocker of LCav3-12b channels when they lack cysteines, with an IC_{50} of ~32μM, see Figure 3.20B.

Zinc is an even more potent inhibitor of native LCav3 channels compared to nickel with a 50% blocking concentration (IC_{50}) of ~ 137 and 158 μM for LCav3-12a and LCav3-12b, respectively. LCav3-12 ΔC channels can be inhibited at a concentration 40- fold lower than their counterparts when cysteines are mutated, with an IC_{50} of 3.3 and 2.7 μM for 12a ΔC and 12b ΔC respectively (see Figure 3.21B).

The increase blocking ability of nickel and zinc is approximately equivalent for cysteine mutations of both LCav3-12a and LCav3-12b channels, suggesting that the native 12a and 12b exons contribute to a similar extracellular structure that shields snail LCav3 channels from divalent cation block. 50% block of native snail channels by nickel (~300 μM) and zinc (~140 μM) is in the hundred to low hundreds of μM, which is in the ballpark of blockade for native human Cav3.1 channels (nickel IC_{50}: 250 μM, zinc IC_{50}: 82 μM) and Cav3.3 channels (nickel IC_{50}: 216 μM and zinc IC_{50}: 158 μM) (Cataldi et al., 2007; Traboulsie et al., 2007). Cav3.2 channels are much more sensitive to divalent cation block with 50% blocking concentrations (IC_{50}) of nickel at 4.9 μM and zinc at 0.78 μM. (Diaz et al. 2005; Lee et al.,1999).

The removal of cysteines in the Domain II turret, engender LCav3 channels with a more potent nickel and zinc block that is in the single or tens of micromolar concentrations for LCav3-12bΔC, (nickel IC_{50}: 32 μM, and zinc IC_{50}: 2.7 μM) and LCav3-12aΔC (nickel IC_{50}: 68 μM, and zinc IC_{50}: 3.3 μM) that resembles the native block of Cav3.2 channels. The involvement of the extracellular turret domain as a determinant for the potency of nickel and zinc drug block is a novel finding.

There are other resemblances with the high affinity zinc block of Cav3.2 channels engendered to snail LCav3 channels when cysteine residues are mutated. One observations of zinc block is that higher concentrations are applied in mM concentrations, the peak current is increasingly blocked, but the inactivation kinetics of the T-type channels are increasingly slowed

down. At higher concentrations, LCav3 containing exon 12 has a slower inactivation current. LCav3-12b has a tau inactivation that increases from 20.31 ± 3.188 ms at 10 μM to 69.50 ± 1.90 ms at 1 mM. LCav3-12a has an even slower inactivation kinetic when 1 mM zinc is applied, with a tau inactivation of 81.29 ± 4.55 ms compared to 17.02 ± 0.34 ms at 10 μM. In comparison, LCav3 lacking cysteines show a negligible difference in their tau inactivation as channel block increases, with a 21.56 ± 0.58 ms at 100 nM to 29.59 ± 3.28 ms at 30 μM for LCav3-12b ΔC and 13.70 ± 0.71 ms to 22.64 ± 2.97 ms for LCav3-12a ΔC, see Figure 3.21D. This zinc effect on slowing inactivation kinetics is not apparent in LCav3-12a and -12b channels when the cysteines in the extracellular turrets are mutated. This absence of zinc effects on inactivation kinetics is also common to Cav3.2 channels, but not for the more weakly blocked channels by zinc (Cav3.1 and Cav3.3) (Traboulsie et al., 2007). It is important to note that zinc is a complex modulator of T-type channels and has other known effects such as shifting the voltage-sensitivities for activation and inactivation and changes to deactivation kinetics.

The high zinc and nickel sensitivity for Cav3.2 channels has been previously explained by an interaction site in the voltage-sensor domain rather than the pore domain. A key residue is histidine (H191) in the extracellular loop in Domain I connecting S3-S4 segments, which is a glutamine in Cav3.1 and Cav3.3 channels (Kang et al., 2006). Snail LCav3 channels also lack a histidine residue at position 191, but clearly this may not be a critical contributing factor of metal binding to the snail channel as the extracellular turret is in the Domain II pore.

The resemblances of cysteine mutations in snail LCav3 channels changing both the drug binding affinity and kinetics of drug block for divalent cations, from a channel that highly resembles Cav3.1/Cav3.3 channels to Cav3.2 channels, is consistent with the extracellular turret playing a role in differing affinities of mammalian T-type calcium channels (Broshawn, del Marmol, MacKinnon, 2012).

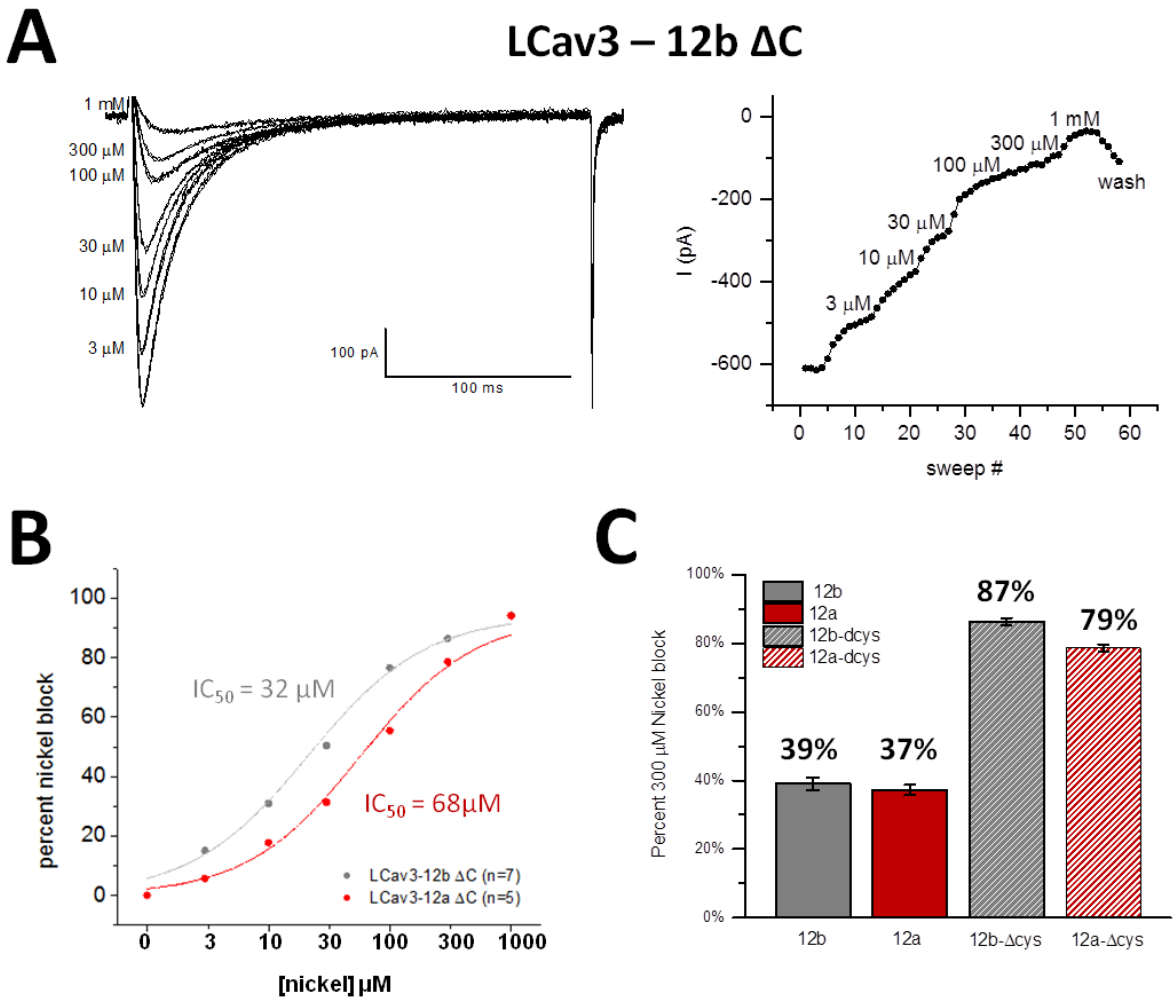

Figure 3.20. Nickel drug response profile for snail LCav3 channels.

(A) Representative current traces of nickel block in LCav3-12b ΔC on the left. The right panel shows the rate of block of nickel over time, each sweep lasting 10 seconds. (B) Drug response profile of LCav3-12b ΔC with an IC_{50} of 32 µM and LCav3-12aΔC with an IC_{50} of 68µM. LCav3-12 ΔC channels are fully inhibited at 1 mM. (C) A bar graph comparing the percentage of nickel block at 300 µM between LCav3-12 and LCav3-12 ΔC channels.

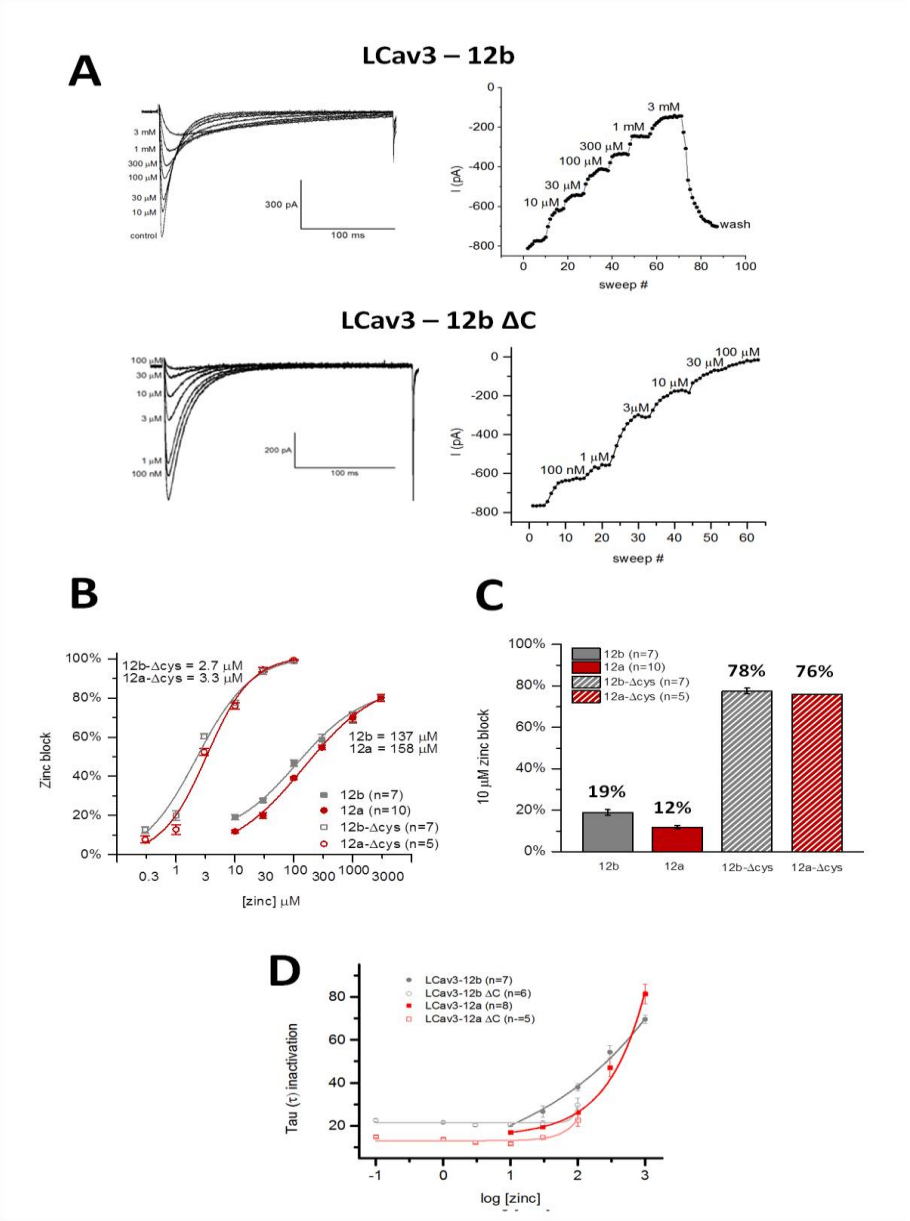

Figure 3.21. Zinc drug response profile.

(A) Sample current traces of zinc block in LCav3-12b ΔC on the left side. The right panels illustrate zinc block over time, with each sweep lasting 10 seconds. LCav3-12b shows a flatter decay in current indicating a slower inactivation at higher concentrations of zinc. (B) Drug response profile of zinc for LCav3-12a ΔC, LCav3-12b ΔC, LCav3-12a and LCav3-12b with IC_{50} effects at 2.7 µM, 3.3 µM, 158 µM and 317 µM respectively. Full blocks occur at 100 µM and 1mM for LCav3 lacking cysteines and wild type channels respectively. (C) A bar graph comparing percentage of zinc block at 10 µM. (D) Tau inactivation of all LCav3 channels at differing zinc concentrations.

3.3 Effects of Cav3.2 (α1H) exon 12 in LCav3 (LCav3-α1H)

Snail LCav3 channels, like other invertebrate protostomes, utilize an exon 12a switched in replacement of exon 12b to generate highly sodium permeable T-type channels. Human T-type channels like Cav3.1 and Cav3.2, are much more calcium-selective channels. We introduced exon 12 from Cav3.2 (α1H) into the snail LCav3 background (creating LCav3-α1H) to address whether the human exon 12 from human Cav3.2 is enough to confer calcium-selectivity to the snail LCav3 channel. Exon 12 of hCav 3.2 turret was purchased as a synthesized gene insert of 207 bp (Biobasic) that was flanked by restriction enzymes, AvrII and Eco47III (AfeI). The synthetic gene insert was cloned into a subclone of LCav3-12a using AvrII and Eco47III, and then this subclone was introduced into the full length expressible LCav3 construct in pIRES2-EGFP vector. All plasmid constructs were confirmed by DNA sequencing at TCAG DNA Sequencing Facility at Sick Kids Hospital, Toronto.

It is clear from an examination of sequence alignments of exon 12, that exon 12 is not the only structural feature that confers the differences between the high sodium permeability of snail LCav3 and the more calcium selective human Cav3.1 and Cav3.2 channels. First, exon 12 of the human channels Cav 3.1 hardly differ between Cav3.2 and Cav3.3 channels, but their sodium permeation varies from 25% to 40% of the total channel current, respectively. Second, the highly sodium permeant variant of the snail channel, exon 12a is closest in sequence to the human exon 12. Human Cav3.2 in exon 12 differs from LCav3-12a by only twelve amino acids and is 39 amino acids, the same length as LCav3-12a. Human Cav3.2 is dramatically different in sequence from LCav3-12b, which supports the more calcium permeant snail LCav3 channel. Cav3.2 differs from LCav3-12b by thirty amino acids, eleven of which add to the length of exon 12b to its longer length of 50 amino acids.

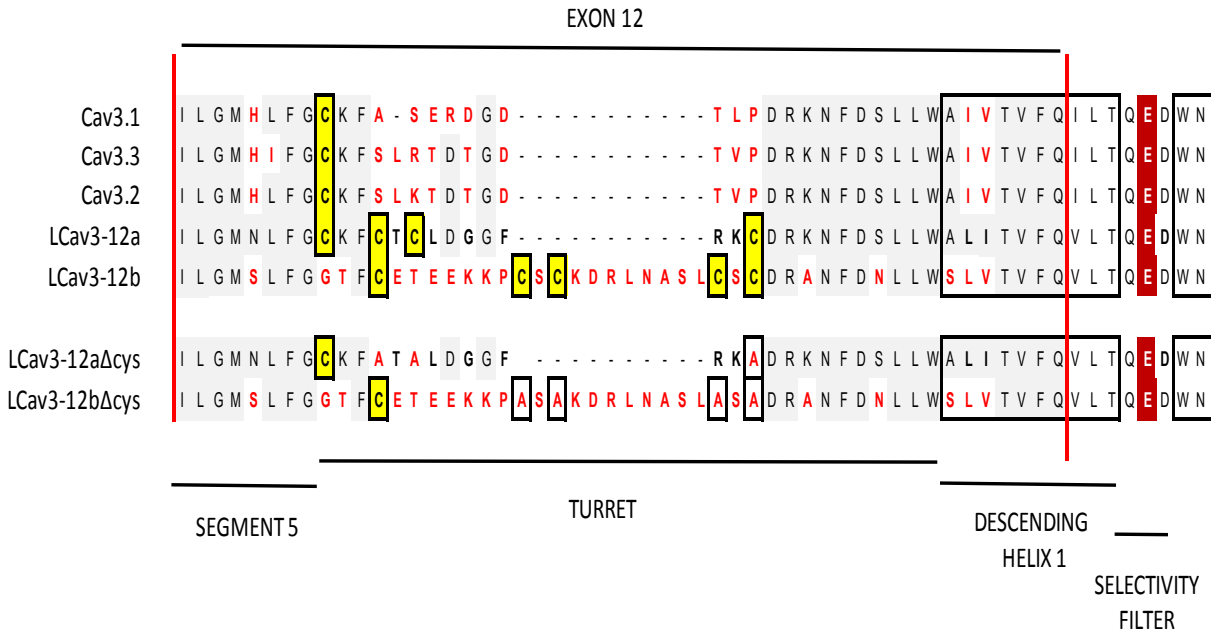

Figure 3.22. Sequence alignment of domain II turret regions in LCav3 channels and mutants.

Amino acid sequences are aligned for human, snail and snail mutant T-type calcium channels. Conserved cysteine residues are highlighted in yellow and differences in amino acids changes are indicated in red.

3.3.1 Biophysical kinetics of LCav3-α1H

A large outward current is present for LCav3-α1H turret channels, similar to the current observed in LCav3-12a, see Figure 3.23B. A comparison of current voltage curves reveals that LCav3- α1H has a sodium permeability between LCav3-12a and LCav12b.

Remarkably, snail LCav3-12a and LCav3-12b channels barely differ in biophysical properties and drug block with nickel and zinc, even with their dramatic difference in sodium permeation. The high similarity of LCav3 channels with exons 12a and 12b suggest they are both optimized structures to maintain common electrophysiological properties outside of their differing sodium permeabilities. LCav3-α1H has fewer differences in amino acid sequence compared to LCav3-12a, yet there are much larger changes to biophysical properties outside of ion selectivity. The much larger biophysical differences indicates that the exon 12 region can modify biophysical properties, and that an artificial construct with a human Cav3.2 exon 12 is not optimized for the snail LCav3 background.

LCav3- α1H generates a significant negative shift in $V_{1/2}$ activation by 8 mV compared to LCav3 and 13 mV for hCav 3.2. Inactivation at $V_{1/2}$ occurred at -75 mV, a 5 mV and 10 mV negative shift for LCav3 and hCav 3.2 channels respectively. Furthermore, LCav3- α1H has faster time to peak and tau inactivation than LCav3 and hCav3.2. Deactivation kinetics are faster at negative voltages (-100 mV) but are significantly slower at depolarized membrane potentials (-60 mV). No significant changes were observed for recovery from inactivation between LCav3-α1H and LCav3-12a and hCav 3.2. Table 9 summarizes the biophysical kinetics of LCav3- α1H and a one-way ANOVA was performed combined with a Student-Newman-Keuls *post hoc* test.

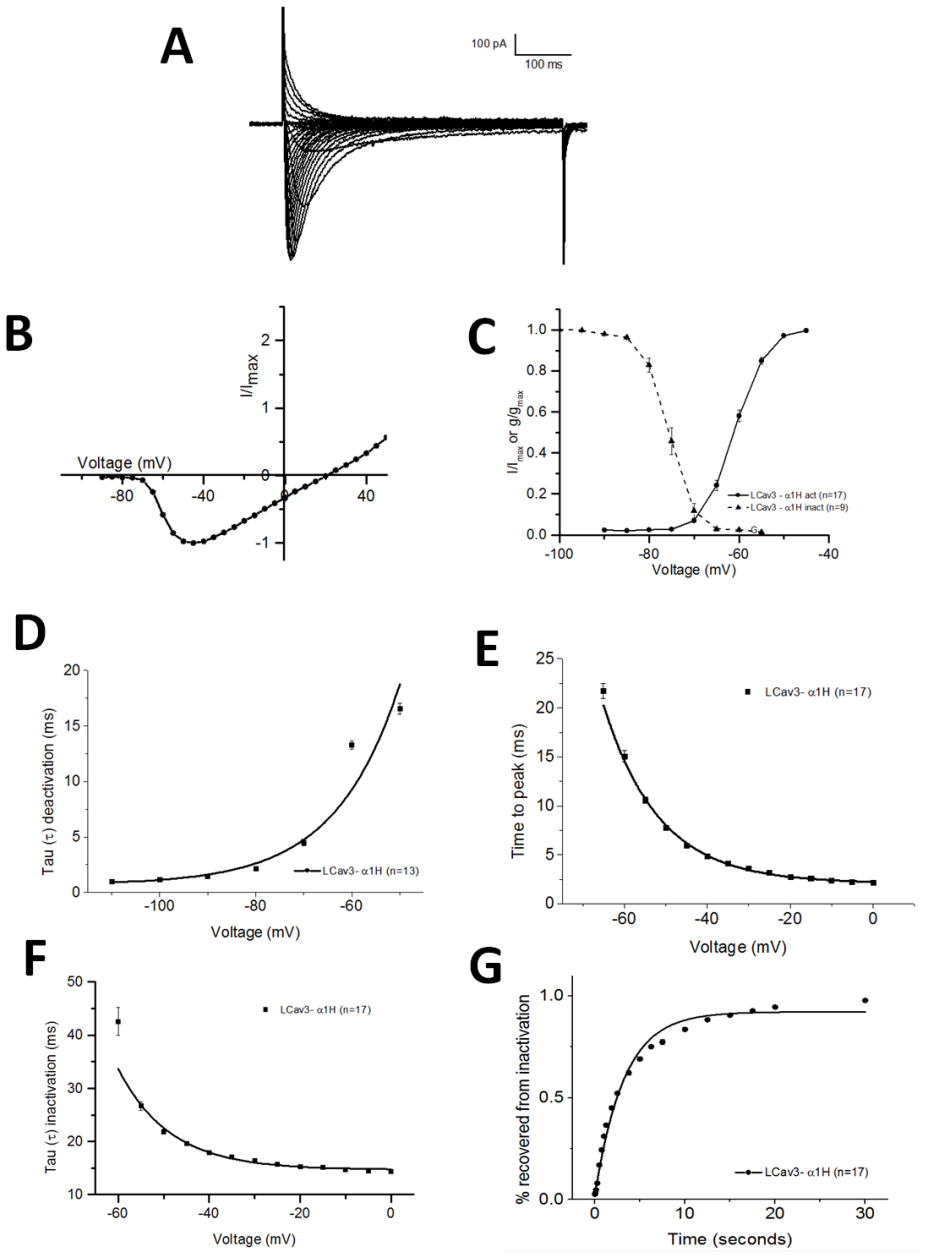

Figure 3.23. Biophysical kinetics of LCav3- α1H.

(A) Currents are generated from a holding potential of -110mV and depolarized from -90 to +80 mV in 5 mV increments. (B) Current voltage relationship (C) Activation and steady state inactivation (D) Tau inactivation in milliseconds (E) Time to peak in milliseconds (F) Tau deactivation in milliseconds (G) Recovery from inactivation in seconds.

Table 9. Biophysical kinetics of LCav3- α1H compared to LCav3 isoforms and hCav 3.2.

	LCav3- α1H	n	LCav3-α1H / LCav3 -12a	LCav3-α1H / LCav3 -12b	LCav3-α1H / hCav3.2
Activation					
$V_{1/2}$	-61 ± 0.42	17	**	**	**
K	3.10 ± 0.081	17	**	**	**
Peak of IV	- 45 mV	17			
Inactivation					
$V_{1/2}$	-75.57 ± 0.71	9	**	**	**
K	2.41 ± 0.051	9	n.s.	**	**
Activation kinetics					
TTP -55 mV (ms)	10.58 ± 0.32	17	**	**	**
TTP -10 mV (ms)	2.34 ± 0.071	17	**	**	**
Inactivation kinetics					
τ -55 mV (ms)	26.72 ± 0.81	17	*	*	**
τ -10 mV (ms)	14.73 ± 0.30	17	**	n.s.	n.s.
Deactivation					
τ -100 mV (ms)	1.18 ± 0.059	13	**	n.s.	**
τ -60 mV (ms)	13.27 ± 0.37	13	**	**	**
Recovery from Inactivation					
%recovery at 0.25s	7.96 ± 0.0056	12	n.s.	**	n.s.
% recovery at 5s	69.05 ± 0.010	12	*	**	**
$T_{0.5}$ (ms)	1631.26 ± 46.94	12	*	**	**

Values are expressed as means ± standard error mean (S.E.M) and *n* denotes the number of recordings performed for each data set. Statistical comparisons were performed using a one-way ANOVA combined with a Student-Newman-Keuls *post hoc* test in SPSS with * $p < 0.05$, ** $p < 0.01$ and n.s., not significant

3.3.2 Ion selectivity and permeability of LCav3-α1H

LCav3- α1H generates an 8.09 ± 0.80 (n=7) fold more permeant sodium current in 135 mM sodium compared to NMDG in the presence of 2 mM extracellular calcium ions. LCav3- α1H is less sodium permeant than the 15 fold sodium permeant channel, LCav3-12a but greater than the 2-fold sodium permeation of LCav3-12b. Figure 3.24A illustrates the permeability range between LCav3-12a, 12b, hCav 3.2 and LCav3- α1H, with LCav3-12a being the most sodium permeable and hCav 3.2 being the least. Evaluation of relative permeability ratios in the bi-ionic reversal experiment reveals an overall similarity of relative monovalent ion permeabilities compared to calcium ions and slope conductances of LCav3- α1H which is more like LCav3-12a than Cav 3.2, see Figure 3.25.

LCav3- α1H has a higher relative permeability for cesium ions than LCav3-12a and 12b, which could be responsible for the observed 5mV hyperpolarizing shift in the voltage-sensitivity of activation for LCav3- α1H. Slope conductance values for LCav3- α1H fall between LCav3-12a and 12b. This is consistent with the LCav3- α1H having a sodium permeability between LCav3-12a and LCav3-12b. See Figure 3.26 for a comparison of relative sodium permeabilities and slope conductances. The anomalous mole fraction effect followed the same trends, exhibiting a calcium block of 66% at 10 μM, a value in between LCav3-12a and LCav3-12b, see Figure 3.27. Also a 6.6 –fold drop in current size when external calcium rises from 10 μM to 10 mM, which lies in between the 6.9 fold and 2.1 fold drop in current size for LCav3-12a and LCav3-12b, respectively.

Notably LCav3- α1H generates typical T-type currents, that do not display a concurrent outward cesium conductance observed with inward barium currents at step voltages that promote current openings when both inward and outward currents are visible (such as -20 to 0 mV). There is also no separate barium current hump in voltage-ramp experiments suggesting that inward barium currents are not superimposable on concurrent inward sodium currents (data not shown). In conclusion, LCav3- α1H has a sodium permeability that is less than LCav3-12a and LCav3-12a ΔC mutations, but is more sodium permeable than LCav3-12b and LCav3-12b ΔC . The level of sodium permeation does not reach the maximal saturation levels evident with LCav3-12a ΔC and LCav3-12b ΔC where Na^+, Li^+, and K^+ currents are equivalent at steps to high voltages +80 mV when driving force

is highest and currents are greatest. Another feature lacking compared to LCav3-12a ΔC and LCav3-12b ΔC is the weakening of the divalent block of the sodium current, when concurrent monovalent ion and divalent ion conductances are observed in ramp currents.

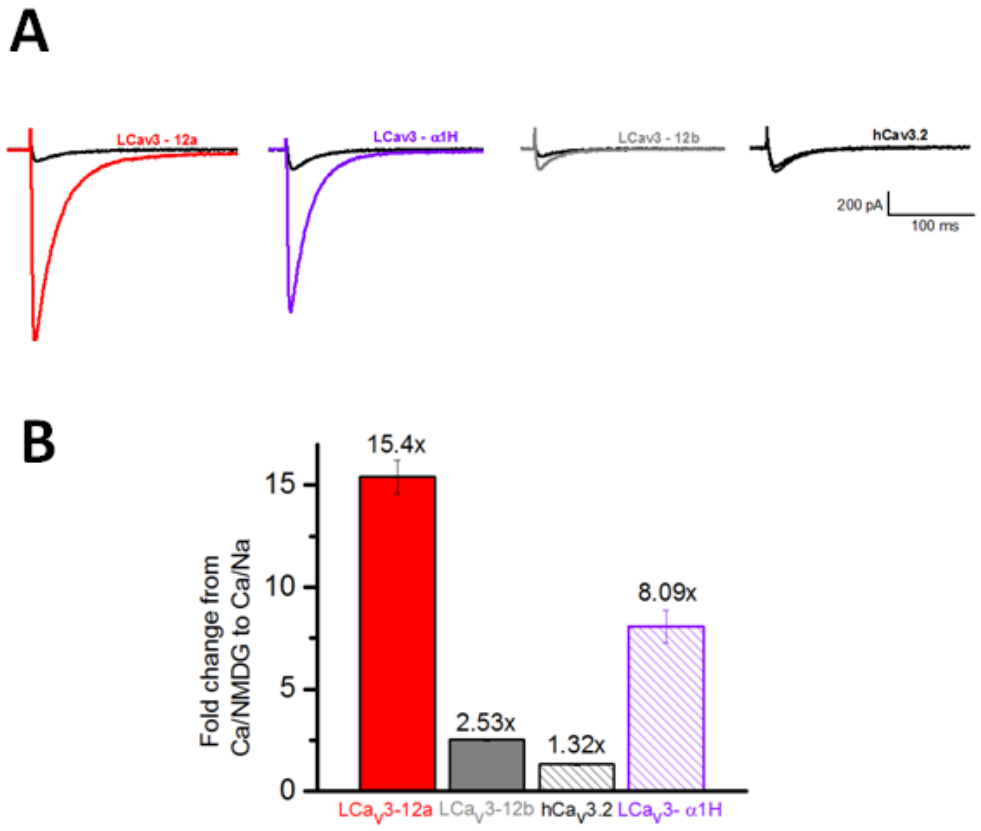

Figure 3.24. A 135 mM sodium current is permeable in LCav3- α1H.

(A) Sample tracings in 2 mM calcium and 135 mM NMDG (shown in black) replaced with equimolar sodium (red, purple, and gray). LCav3- α1H has a permeable that lies in between LCav3-12a and LCav12-b. (B) A bar graph illustrating the relative fold increase in the presence of sodium.

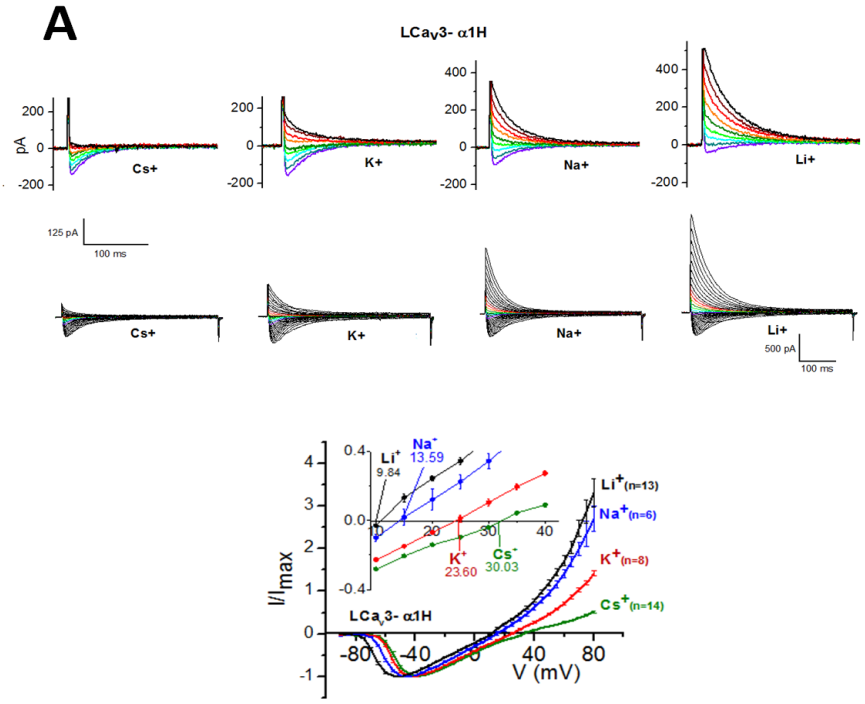

B

	Li^+	SEM	n	Na^+	SEM	n	K^+	SEM	n	Cs^+	SEM	n
E_{rev} LCav3- α1H	9.85	0.54	13	13.59	1.00	6	23.60	0.80	8	30.02	1.43	14
Slope conductance Outward g_x LCav3- α1H	0.082	0.012	13	0.075	.1005	6	0.47	.0064	8	0.014	.00097	14

	P_{Ca}/P_{Li}	SEM	n	P_{Ca}/P_{Na}	SEM	n	P_{Ca}/P_K	SEM	n	P_{Ca}/P_{Cs}	SEM	n
$P_{Ca/Px}$ LCav3- α1H	22.77	0.78	13	28.99	1.82	6	55.66	2.88	8	89.71	8.09	14

Figure 3.25. Bi-ionic reversal potentials with internal Li+, Na+, K+ and Cs+ conducted on LCav3- α1H.

(A) Current traces of LCav3- α1H; a close-up of currents crossing the reversal potential is highlighted by multiple colours in the top panel. In the bottom panel, a current-voltage relationship depicts the permeability of monovalent ions. The inset shows a close-up of the reversal potentials, with *n* denoted in parentheses. (B) Summary chart of LCav3- α1H reversal potential, outward slope conductance and relative permeability ratios for Li^+, Na^+, K^+, and Cs^+. Average means are shown with standard error means (S.E.M) and *n* refers to the number of recordings.

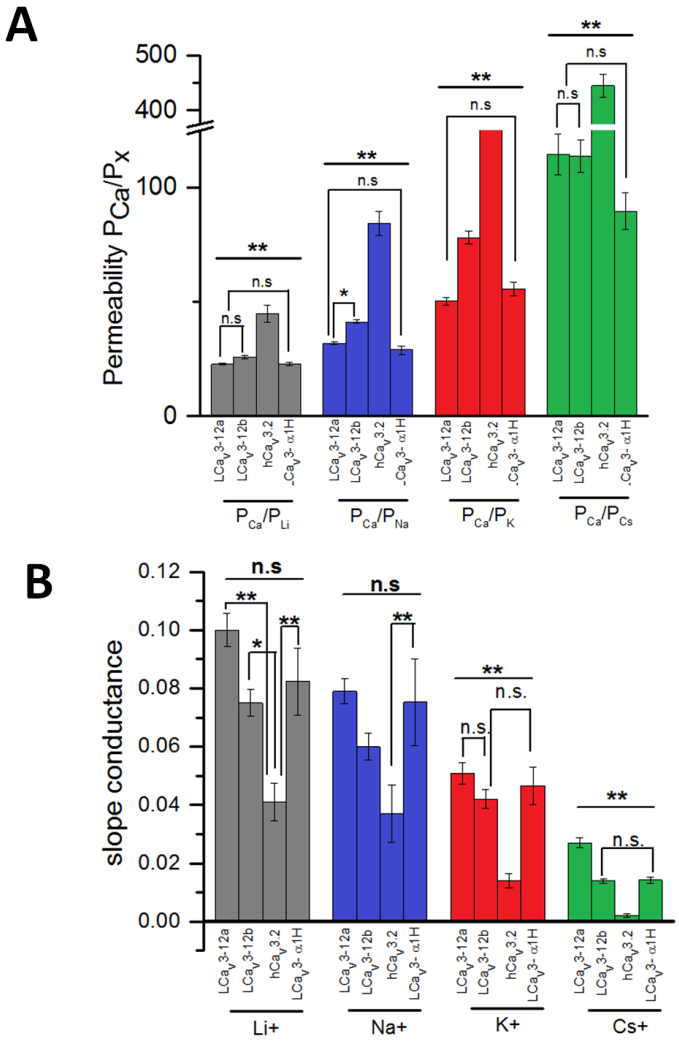

Figure 3.26. Relative permeability ratios and slope conductances comparing LCav3-α1H to LCav3 channels and hCav3.2.

A line spanning all bars indicate all pairs within the group have the same significance, unless otherwise stated. Statistical comparisons were performed using a one-way ANOVA combined with a Student-Newman-Keuls *post hoc* test in SPSS with * $p < 0.05$, ** $p < 0.01$ and n.s., not significant (A) Relative permeability ratios of LCav3- α1H, LCav3-12a, LCav3-12b and hCav 3.2. LCav3- α1H is not statistically significant from LCav3-12a across all monovalent ions. (B) Slope conductances comparing LCav3- α1H to LCav3 and hCav 3.2 channels. LCav3- α1H have slope values that lie in between LCav3-12a and LCav3-12b and it is not statistically significant from LCav3-12b with any internal monovalent ion.

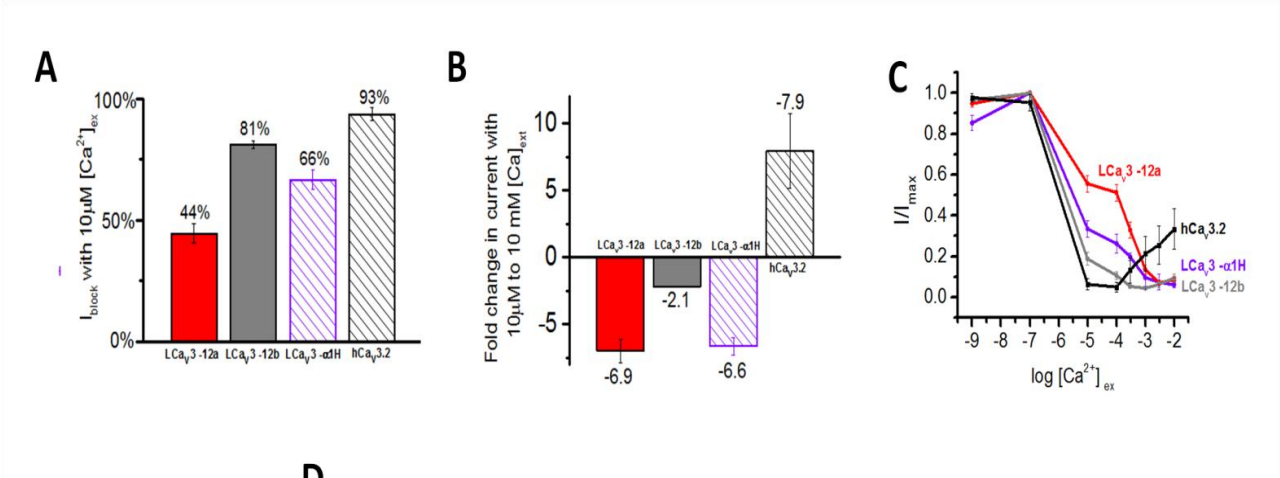

D

log $[Ca^{2+}]_{ext}$	% current block	SEM	n	SNK *post hoc* for AMFE: LCav3-α1H vs LCav3-12a	vs LCav3-12b	vs hCav3.2
-9	14.69	3.63	4	*	**	**
-7	0	0	4	n.s.	n.s.	n.s.
-5	66.52	4.02	4	**	*	**
-4	73.73	4.66	4	**	*	**
-3.52	80.21	1.74	4	n.s.	*	n.s.
-3	90.35	6.09	4	n.s.	n.s.	n.s.
-2.25	92.62	3.81	4	n.s.	n.s.	*
-2	94.03	1.17	4	n.s.	n.s.	**

Figure 3.27. Anomalous mole fraction effect on LCav3- α1H.

(A) The percentage of calcium block at 10 μM is compared among LCav3, LCav3- α1H and hCav 3.2 channels. LCav3- α1H has a 66% calcium block which is less than LCav3-12b and higher than LCav3-12a. (B) Current size changes from 10 μM to 10 mM; all LCav3 exon 12 turrets and LCav3- α1H show a decline in current size indicating a weaker calcium block at higher calcium concentrations. The data is consistent that LCav3- α1H has a permeability that lies in between LCav3-12a and 12b. (C) 60 mM of external sodium is combined with varying calcium concentrations ranging from 10^{-9} to 10^{-2} M, this graph depicts the block of current as calcium concentrations increase. Current block occurs at 10^{-5} M for hCav 3.2, but not for LCav3 channels. (D) A chart outlining the current block by varying calcium concentrations in LCav3- α1H. Average means are shown with standard error means (S.E.M) and *n* refers to the number of recordings. A one-way ANOVA was performed combined with a Student-Newman-Keuls *post hoc* test. * $p<0.05$, ** $p<0.01$ and n.s., not significant.

Chapter 4
Discussion

4.1 Unique splicing of exon 12 in invertebrate channels

The Spafford laboratory cloned and characterized the first *in vitro* expression of a non-vertebrate T-type calcium channel. This invertebrate T-type channel reveals a high conservation of quintessential features of mammalian T-type channels (Senatore & Spafford, 2010). These features include, a low voltage range with a peak current at -40 mV, with similar rapid activation and inactivation kinetics and slow deactivation kinetics. The characterized biophysical features of mammalian T-type calcium channels carried out for this thesis are similar in terms of the approximate voltage range of operation and time constants for kinetics as described by Chemin et al. (2007).

In addition, there are developmentally conserved and regulated splicing in snail T-type calcium channels, such as exon 25c and exon 8c that is regulated in the same fashion as vertebrate T-type channels. T-types calcium channels that lack exon 25c are highly expressed in the embryo and are down-regulated in adult animals leading to biophysical changes in snail LCav3, and human hCav 3.1 and hCav3.2 T-type channels (Senatore & Spafford, 2012). The presence of optional exon 8b is also down-regulated from embryo to adulthood, and regulates the level of protein expression in T-type channels (Senatore & Spafford, 2012). We have described a unique exon splicing that generates highly sodium permeant T-type channels, exon 12a, which spans the extracellular turret and descending pore helix of Domain II upstream of the highly conserved EEDD selectivity filter of T-type calcium channels.

4.2 Differing ion permeability and selectivity between exon 12 variants and mammalian Cav3 channels

The invertebrate LCav3 channels will generate large outward currents in the presence of 100 mM intracellular monovalent ions due to the large driving force at high voltage steps compared to mammalian T-type calcium channels. Permeability of monovalent ions

decreases with increasing ion diameter size Li+ >Na+ >K+ > Cs+, where Li+ ions are the most permeable due to their smaller crystal radii for LCav3 and mammalian T-type channels. These results follow the Eisenman's ion selectivity model (Eisenman et al, 1967).

All T-type channels will pass monovalent ions at low levels of external calcium (<10 μM external calcium ions). Above 10 μM of external calcium, vertebrate T-type calcium channels increasingly pass more current conducted by calcium ions as calcium concentration rises. This low sodium permeability and high calcium permeation of mammalian channels confirms what has been reported by Shcheglovitov, Kostyul, & Shuba (2007). The snail T-type channel isoforms, particularly exon 12a are not very calcium selective like their mammalian counterparts. Calcium ions are not effective at blocking the sodium current at 10 μM of external calcium, with snail LCav3 calcium channels bearing exon 12a being blocked at 44% compared to exon 12b at 81%. Sodium currents in human T-type channels are >90% blocked by10 μM external calcium. Increases to physiological levels does not produce a classical "U" shape calcium dose dependent response curve for snail LCav3 as it does for mammalian T-type channels. Instead, the total current size continues to decline, monotonically at higher calcium concentrations for LCav3 channels, reflecting their reduced affinity for Ca^{2+} in the pore and much higher permeability for sodium ions.

The sodium permeability of LCav3-12a is evident in voltage steps to their peak conductances. When 135 mM sodium ions replace the impermeant cation NMDG, currents are increased 15-fold in exon 12a compared to a 2-fold increase in exon 12b. qPCR detection of various cation ion channels revealed that *Lymnaea* heart expresses a T-type and L-type calcium channel but lacks the expression of the snail Nav1 sodium channel. Ionic currents in snail ventricular cardiomyocytes elicited by voltage ramps generated a low voltage and high voltage activated channels in the presence of external barium ions and NMDG, similar to snail heart currents documented by Yeoman & Benjamin (1999). Replacement of 100 mM external NMDG with sodium produced a 11-fold current increase in the size of low voltage-activated current, reflecting the high sodium permeation of the snail T-type current in snail hearts. A similar profile of currents is evident in the results of voltage

ramps of co-expressed recombinant snail sodium permeable T-type channel possessing exon 12a and the snail L-Type calcium channel in mammalian HEK293T cell lines. Cardiomyocyte currents resemble recombinant T-type calcium channel harbouring exon 12a with fast kinetics, low voltage of activation, a fully inactivated current at holding potential of -60 mV, and nickel and mibefradil sensitivity (Senatore and Spafford 2010), and insensitivity to isradipine, which is a potent blocker of the snail LCav1, L-type calcium channel (Senatore et al. 2010).

4.3 Physiological relevance of alternative splice variants exon 12a and 12b

The distinct tissue expression patterns of exon 12a in the heart and muscle and exon 12b in secretory glands suggest a specialized roles of different permeable T-type channels in different cell types. T-type channel transcript levels steeply decline during embryonic development through adulthood, reflected by the sharp decline in LCav3-12a expression in juvenile to adult hearts. The down regulation of LCav3-12a may relate to allometric scaling during development, where prominent LCav3 currents are found in smaller animals (or non-adults) coinciding with faster heart rhythms (Ono & Iijima, 2005). LCav3-12a isoform possess a slower deactivation rate and faster recovery from inactivation compared to exon 12b. This is consistent with the LCav3-12a adaptations in snail heart, where a slower deactivation serves to prolong the repolarization phase of the cardiac action potential and a faster inactivation prevents run down between heart beats due to cumulative inactivation. The absence of a voltage gated sodium channel in the snail heart indicates that LCav3-12a is the only channel sodium ions are conducting through to generate a pacemaker current in ventricular cells for the fast conduction of heart rhythms.

The more calcium selective isoform, LCav3-12b is in equal abundance in the brain with LCav3-12a, and is the more abundant isoform expressed in the reproductive tissue (albumin gland and prostate gland) of the hermaphroditic freshwater pond snail. The rise in transcript levels from juvenile to adult in LCav3-12b coincides with sexual maturation where albumen gland takes up a role secreting factors that facilitate egg mass formation (Nagle et al., 2001). A faster deactivation rate and slower recovery from inactivation in LCav3-12b

promotes typical burst firing of vertebrate T-type channels, where the rise in intracellular calcium may contribute to pacemaking and possible roles in excitation and secretion coupling (Senatore & Spafford, 2012).

4.4 Evolutionary adaptation of exon 12

An evolutionary pattern of the extracellular turret in domain II of T-type channel is evident in their phylogeny. The copy of a single gene for T-type channels is apparent in the most primitive multi-cellular animals, such as *Trichoplax adhaerens*. All basal animals with T-type channels have a short exon 12 turret with a small number of cysteines ranging from zero to two. An insertion of an intron between exon 11 and exon 12 is found in the simplest protosomes, the flatworms (acoelomates) which allowed for a duplication of exon 12 to generate dual turrets, a highly sodium permeant exon with a tri-cysteine structure (12a) and a more calcium-selective exon with a penta-cysteine structure (12b) in ecdysozan protosomes (eg. nematodes and arthropods) and lophotrochozoan protozoans (eg. molluscs and annelids), see Figure 4.1. Associated with protostomes is the appearance of coelom and internal organs such as the heart which require a fast sodium-dependent spike to coordinate activities in their body. Nav1 sodium channels diverged into 10 different Nav1 sodium channel genes fulfilling roles inside and outside the central nervous system. Invertebrates have a single gene coding for Nav1, which is absent in many species and not abundant outside the central nervous system (ex. *Lymnaea stagnalis*). Sodium-permeable T-type channels are potentially adapted in invertebrates to generate sodium spikes in the absence of voltage gated sodium channels.

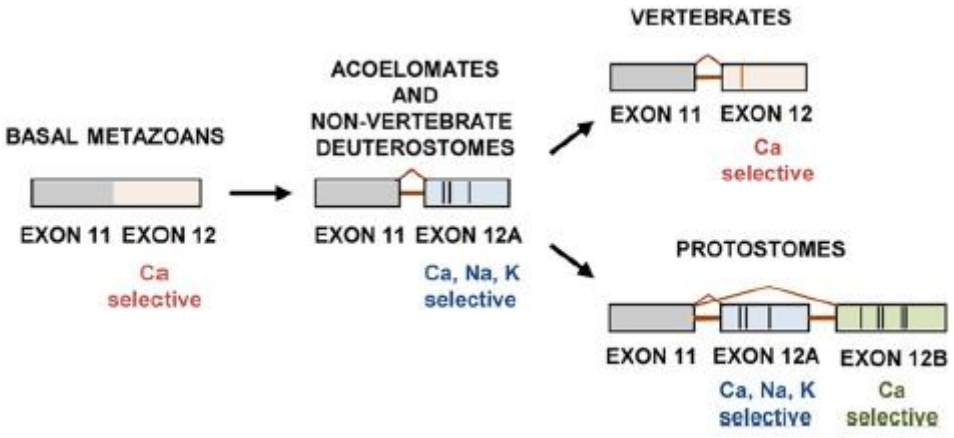

Figure 4.1. Proposed evolution for exon 12.

An intron separates exon 11 and 12 to give rise to a sodium permeable channels with a tri-cysteine (12a) and penta-cysteine (12b) structure. Evolution of a uni-cysteine motif in exon 12 of vertebrate Cav3 supports a more calcium selective channel. (Reproduced from Senatore, A, 2012)

4.5 Changes in biophysical kinetics with turret mutations

LCav3 domain II turret lacking all but one cysteine and LCav3 with the α1H unicysteine turret showed a statistical significant change in biophysical kinetics from their original counterparts. These changes include a shift to the left in activation and inactivation curves, faster recovery from inactivation and deactivation. Modification in kinetics suggests that the extracellular turret between S5 and S6 in domain II have contributions to gating changes. Ion conduction and gating can be envisioned as two separate entities controlled by the separate pore domain (consisting of S5-pore loop-S6) and the voltage sensor domain (S1-S4) respectively. Evidence from HERG voltage-gated potassium channels indicate that the turret region has influences on both gating properties and ion selectivity changes, like the T-type calcium channels.

hERG (or Kv11.1 coded on the KCNH2 gene) is the human homolog of the *Drosophila* ether-a-go-go gene, within the family of voltage-gated potassium channels. hERG is responsible for the rapid component of the delayed rectifier K+ channel current (I_{KR}) for mammalian atrial and ventricular myocytes. Mutations in hERG contribute to

Long-QT Syndrome (LQTS), the inherited heart condition in which repolarization is delayed and the duration of action potential is prolonged (Vandenberg et al., 2012). A key biophysical feature of hERG channels is that they functionally resemble an inward rectifier potassium channel, passing little inward current during the depolarized plateau phase of a heart action potential and producing an outward current during repolarization. They have a very slow rate of activation and deactivation, and are inactivated at depolarized potentials (Shi et al., 1997; Vandenberg et al., 2012). The inactivation of hERG channels is relieved by hyperpolarization and thus they contribute to the rapid component of repolarization. These channels possess a very quick and voltage-dependent, C-type inactivation essential for normal cardiac regulation. It is expected that inactivation causes a collapse of the pore structure, the presence of external TEA can occupy the selectivity filter to prevent the pore from "collapsing" (Choi et al.,1991; Vandenberg et al, 2012).

hERG channels resemble other voltage-gated potassium channels but are uniquely different in possessing an extended turret region (S5-P loop) that is 40 amino acid long, compared to 10 to 15 amino acids for other voltage-gated potassium channel types (Torres et al., 2003). Substituting cysteines and probing for their accessible for thio-modifying methanethiosulphonate (MTS) modification, reveal that the middle (15 amino acid) fragment of the S5-P linker is exposed to the extracellular environment along its length. This middle fragment, appears to form an amphipathic helical structure that runs parallel to the membrane, and many of these substituted cysteines appear to form disulphide bonds with indeterminant partners between subunits in hERG channels (Torres et al., 2003; Liu et al., 2002). Nuclear magnetic resonance (NMR) studies show that the S5-P domain is dynamic and may switch between helical and unstructured conformations, depending on their interactions with hydrophobic or hydrophilic environments (Jiang et al., 2005). This flexibility is considered to contribute to the unusually rapid, C-type inactivation, and the sensitivity to change that leads to altered ion selectivity and drug block. hERG channels noticeably lack the three major amino acids glutamate (E), tryptophan (W) and tyrosine (Y) which are well conserved in typical potassium channel turrets. These amino acids are known

to form hydrogen bonds and stabilize the outer mouth of typical voltage-gated potassium channels, like in the *Shaker* potassium channel (Fan et al., 1999). These hydrogen bonds around the outer mouth of the pore contribute to the slow kinetics and the lack of voltage-dependence in *Shaker* potassium channels (Vandenberg et al., 2012).

The functions of the extended turret region (S5-P loop) in hERG influences ion selectivity, biophysical features and drug block of specific toxins. Swapping in S5-P turret domains between closely-related Kv11.1 (hERG) with other homologs with extended turrets such as Kv12.2 (hELK-2) and Kv10.1 (hEAG), confer a dramatic change in the voltage-dependence of inactivation, which is consistent with the S5-P region substantially contributing to voltage gating (Jiang et al., 2005). Individual mutations in the middle part of the S5-P loop, produce a common mutant phenotype which disrupts the characteristic rapid, strongly C-type, voltage-dependent inactivation of hERG channels and a dramatically lowered ion selectivity of these channels for potassium ions over sodium ions (Jiang et al., 2005; Dun et al., 1999). hERG channels are the only voltage-gated potassium channels with an extended turret and is the only potassium channel where S5-P loop mutations cause such dramatic change in biophysical differences and dramatic changes to ion selectivity (Liu et al., 2002). Mutated S5-P turrets with reduced potassium selectivity also have altered drug binding properties.

Toxin sensitivity has been reported in various classes of potassium channels. For example, agitoxin 2 (AgTx2) and charybdtoxin (ChTx) are a well known scorpion toxins that can bind to the pore of Shaker potassium channels, yet it fails to adequately block hERG channels (Jimenez-Vargas et al., 2012). Other scorpion toxins such as BeKm-1 and Ergtoxin (ErgTx-1), are part of the γ-KTx toxin family. These toxins can sufficiently inhibit hERG channels that do not bind to other members of the voltage gated potassium channel family (Torres et al., 2003;Jimenez-Vargas et al., 2012). The S5-P loop is a critical region for γ-KTx toxin binding and confers the difference in toxin sensitivity between members of the potassium channel. The longer turret region in hERG acts as a binding surface for γ-KTx toxins, whereas ChTx blocks deep within the pore of Shaker channels to plug the selectivity

filter and prevent conduction of potassium ions (Xu, et al.,2003; Vandenberg et al., 2012). Mutagenesis studies indicate that the external binding site for γ-KTx toxins involves the outer pore including the S5-P linker, and critically involves hydrophobic residues that occupy the high impact positions, whose mutation can decrease toxin binding by ~200 fold and weaken potassium ion selectivity and the rapid voltage-dependent inactivation of hERG channels (Xu et al., 2003; Jimenez-Vargas et al., 2012).

Invertebrate T-type calcium channels confer similarities to hERG channels, demonstrating changes in biophysical properties and reduced ion selectivity when mutations in the turret occur. While, hERG channels provide insight into turret mutations and their effects, it is still uncertain what is happening to snail T-type calcium channels at a mechanistic level.

4.6 Altered ion permeability and selectivity in turret mutations

The S5-P region that confers the relative sodium or calcium ion selectivity in T-type channels has variable sequences but the size of the turrets and the number of cysteines are highly conserved. Pairs of cysteines can form disulfide bridges in proteins that are known to help stabilize protein conformations in tertiary and quaternary structure. Cysteine residues that are not involved in a disulfide bond can also help to stabilize alpha helices.

The loss of cysteine residues in the LCav3 domain II turret probably disrupted disulfide bonds that act as bridges to form a defined extracellular structure above the T-type channel pore. Extracellular structures formed by extended S5-P regions that alter the external landscape above ion channels is common for hERG type channels, eukaryotic inward rectifying potassium channels (K_{IR}) and two pore leak potassium channels (K_{2P}) (Torres et al., 2003; Brohawn, del Marmol & MacKinnon, 2012; Miller & Long, 2012). In K_{IR} channels, the larger S5-P turret region brings the turrets from all four domains closer together and the pore entryway is much narrower, creating an external landscape that is responsible for the insensitivity of K_{IR} channels to toxin block (Tao et al., 2009). K_{2P} have an even larger turret, and a cysteine disulphide bond in the two opposing turrets form a helical cap above their pore to prevent ions from entering above and acts as a pre-filter for incoming ions, see

Figure 4.2 (Tao et al., 2009; Brohawn, del Marmol & MacKinnon, 2012). The T-type channel with Domain II cysteines likely forms an external structure that regulates ion selectivity, drug binding and contribute to gating changes.

Snail T-type channels with altered turrets (LCav3-12a ΔC and LCav3-12b ΔC) generate outward monovalent ion currents that are larger than their wild type counterparts. Outward currents for monovalent ions converge in the bi-ionic reversal experiment to saturating levels of maximal conductances elicited at high voltage potentials despite the differing monovalent ions (Na^+, K^+, and Li^+) which have differing ionic radii. The saturating level of conductance is a maximum rate limited by the diffusion forces for outflow of internal ions at high voltages, where the driving force for outflow of monovalent currents is maximal and outward currents are no longer competing with inward sodium ions. Cesium, the largest of the four ions does not have a converging outward current with the other ions (Na+, K+, and Li+), indicating that its larger size than the other ions puts a constraint on its maximal conductance. This most likely indicates a size threshold that limits its maximal conductance. The saturation of maximal conductance may suggest that the ion diameter of the pore is larger, thereby it cannot discriminate the permeability of differing monovalent ions of differing sizes below the ionic radius of Cs+ (ie. Na^+, K^+, and Li^+).

Despite the lack of cysteine residues in LCav3-α1H, we did not observe a convergence of outward currents in the bi-ionic experiments suggesting it does not reach a maximal rate of saturation with differing ions. LCav3-α1H encompasses all of exon 12 from Cav3.2 which notably includes the descending helix from hCav3.2 in addition to the extracellular turret. Potential changes in the descending helix taken from hCav 3.2 may have influenced the pore diameter for monovalent ion passage. It is known that negatively charged residues within the selectivity filter form transient binding partners outside the selectivity filter in structural intermediates of the calcium channel pore (Senatore et al., 2014). Changes in the descending helix may be sufficient to reorient a selectivity filter residue, altering the relative permeation of sodium and calcium ions.

4.7 Calcium versus barium in turrets lacking cysteines

Similar diameter divalent cations, barium and calcium generate macroscopic currents with varying permeabilities among vertebrate T-type calcium channels. For example, barium currents are smaller than calcium currents for hCav 3.1 channels, and larger barium currents than calcium currents for hCav 3.2 channels (Shcheglovitov, Kostyuk & Shuba, 2007). .Differences in divalent ion currents may be a reflection of differences in channel gating, such as their open channel probability (Shcheglovitov, Kostyuk & Shuba, 2007). Divalent ions alter gating kinetics, where channels are open less often in hCav 3.1 in the presence of barium, and open for an overall longer time period as calcium currents at a single channel level (Shcheglovitov, Kostyuk & Shuba, 2007).

Snail T-type calcium channels, LCav3-12a and 12b exhibit a similar barium permeability to one another and to mammalian Cav3.2 channel. LCav3 lacking cysteines generate a smaller current in barium than calcium ions, which resembles the behavior of hCav 3.1 channels. During current-voltage steps with the major ions being high cesium ion concentrations on the inside (100 mM) and high external barium concentration on the outside (2 mM), there is a large driving force for barium entry at more negative membrane potentials and a large driving force for outward monovalent ion currents at highly depolarized potentials. In between these two extremes, at potentials like (-20 mV to -10 mV), there are small measureable inward barium currents that also overlap, with a noticeably delayed outward cesium current. LCav3 channels appears to accommodate both monovalent and divalent ions traversing across the channel pore at once in cysteine mutated LCav3 channels where cesium currents pass, but is delayed in time after the barium current has entered. Normally in non-cysteine mutated channels, this behavior does not exist. It appears to lack a mixed current, where both currents pass at the same time. Barium currents are diminished almost completely towards its particular reversal potential, and at more depolarized potentials above this, outward currents are elicited in the absence of barium entry by cesium ions. When both sodium and barium ions are concentrated outside, inward currents generated also reflect an accommodation of both ions at once for cysteine mutated LCav3 channels.

Currents elicited by ramp protocols generate a double hump, the first hump being a rapid sodium ion entry followed by a barium current. The sodium current is much larger than the barium current in more highly sodium permeant channel, LCav3-12a ΔC than the lesser sodium permeant, LCav3-12b ΔC channel.

The concurrent divalent and monovalent ion currents through cysteine mutated channels applies to barium as the divalent cation, but not to calcium, the physiologically relevant ion. Calcium likely has a stronger affinity for the cysteine mutated channels than barium which serves to prevent the concurrent passage of a permeant monovalent ion, such as sodium.

Another unusual finding is the lack of concurrent barium and monovalent ion passage in LCav3 channels when the whole exon 12 from Cav3.2 was replaced for the S5-P region in LCav3 (LCav3-α1H). LCav3-α1H comprised of the turret and descending helix of domain II from hCav3.2. The differing descending helix of hCav3.2 may be one of the factors that may contribute to the observed differences in LCav3- 12ΔC channels. The descending helix of hCav3.2 differs from LCav3-12a in three amino acids, and these may contribute to a pore structure that does not enable the concurrent passage of barium and monovalent ions.

4.8 Nickel and zinc block is more sensitive in turrets lacking cysteines

Drug profiles for nickel and zinc greatly enhanced sensitivity to divalent metal ion block for LCav3 channels lacking cysteines in their domain II turrets. LCav3-12b ΔC displays a ~10-fold increase in sensitivity to nickel and LCav3-12a ΔC has roughly a ~5-fold increase in sensitivity to nickel compared to their wildtype counterparts. Nickel blocks at an IC_{50} ~300 μM for LCav3 channels with an exon 12b turret (Senatore & Spafford, 2010). And nickel block is similar between the native variants, LCav3-12a and LCav3-12b which have a 37% and 39% block of nickel at 300 μM concentration. The removal of cysteines (LCav3-12b ΔC and LCav3-12a ΔC) leads to nickel sensitive channels with an IC_{50} for nickel block that is, 32 μM and 68 μM, respectively. The mutations in cysteines generates snail Cav3 channels that approach the high nickel selectivity of the more nickel sensitive

Cav3.2 channel in mammals. Nickel will block Cav3.2 channels at concentrations of 5-10 μM in comparison compared to hCav 3.1 and hCav3.3 which require a concentration between 100-300 μM (Kang et al. 2006).

There is also a ~50-fold increase in zinc block in LCav3 channels lacking cysteines. Zinc inhibits the native snail Cav3 channels at a similar 50% blocking concentrations of 138 μM and 158 μM for exon 12b and 12a containing S5-P regions, respectively. The range of block for zinc to the native snail channel resembles the weaker zinc block of ~ 82 μM and 158 μM for hCav 3.1 and hCav 3.3 channels respectively (Cataldi et al, 2007; Traboulsie et al., 2007). Mutations of cysteines, generates channels with a high affinity zinc block that resemble the highly sensitive hCav3.2 channels with a IC_{50} of 3 uM in LCav3-12ΔC (Kang et al., 2006).

Normally high concentrations of zinc will slow down inactivation kinetics, which is a feature that has been reported for hCav 3.1 and hCav 3.3 channels, channels that lack a high affinity zinc site (Cataldi et al, 2007; Traboulsie et al., 2007). Both the snail channel lacking domain II turret cysteines and the more high affinity zinc binding channel, Cav3.2 do not have slowed inactivation kinetics in response to application of high concentrations of zinc (Traboulsie et al., 2007). The removal of cysteines in snail channels appears to resemble a switch of these channels from hCav 3.1 and hCav 3.3 channels to the hCav3.2 channels both in the range of higher nickel and zinc sensitivity and conferring the quality of its zinc block (loss of slower inactivation kinetics in hCav3.2 channels) that is present in hCav 3.1 and hCav 3.3 channels. The slow inactivation with zinc for hCav 3.1 and hCav 3.3 channels is believed to be caused by the conformational change of the pore selectivity filter during channel opening that allows zinc to bind to a pore site for these channels and blocking the inactivation gate from closing. An analogous "foot in the door" mechanism has been proposed to explain the dramatically slowed C-type inactivation when extracellular permeant ions, such as rubidium (Rb+) are applied to *Shaker* K+ channels (Lopez- Barneo et al, 1993; Hille, 2001).

Nickel and zinc are considered to interact with histidine (H), cysteine (C), glutamate (E) and aspartate (D) at an extracellular metal binding site formed by the extracellular loop connecting S3 and S4 in domain I (Kang et al., 2006; Van horn, 2003; Shuba, 2014). The most critical of these residues for nickel sensitivity of hCav3.2 has been attributed to the histidine residue (His-191). Point mutations of His-191 to glutamine in hCav3.2 diminishes nickel sensitivity to high concentrations similar to hCav 3.1 (Kang et al., 2006).

While His-191 and other residues within Domain I, S3-S4 contribute to a nickel and zinc binding site, it is clear that the external turret also play a role, which may contribute to two distinct or overlapping binding sites for T-type channels that has been suggested by others . Nosal and researchers (2013) postulated there was another binding site for nickel blockade by the P-regions, known as the intrapore binding site. This binding site is believed to limit the conduction of divalent ions such as calcium, barium and strontium and the higher affinity for a certain ion will limit the permeation of others. Depending on the divalent charge carrier, the sensitivity of nickel block can increase by 2.5-3.5 fold in hCav3.1(Nosal et al. 2013). It is possible that snail T-type calcium channels contain an intrapore binding site, located by the turret region which contains a high affinity binding site for calcium ions .The mutant channels lacking cysteine residues disrupted the affinity for calcium ions and allowed for high affinity binding of nickel/zinc to occur.

4.9 Physiological consequences of turret mutations

Long QT syndrome (LQTS) is a heart disorder characterized by delayed repolarization of cardiac action potentials that can lead to palpitations, fainting and sudden death due to ventricular fibrillation (Fougere et al.,2011; Vandenberg et al., 2012). LQTS type 2 is caused by mutations in human ether-a-go-go related gene (hERG) in delayed rectifier potassium channels (I_{Kr}) and can lead to increase arrhythmias. Single amino acid mutations occur more frequently in the turret (S5-P) region of the hERG channel than S1-S4 transmembrane domains (Fougere et al.,2011). In hERG channels, it is speculated that the turret acts as a bridge between the voltage sensor in S4 transmembrane segments and the pore where inactivation takes place. Point mutation of arginine in position 582 to cysteine

(R582C) demonstrated deficient membrane trafficking and could not be recorded unless the experiments were conducted at a reduced temperature (from 37°C to 30°C). Deficient trafficking reduces the number of channels available at the plasma membrane, and lowers the number of hERG channels available for repolarization of cardiac action potentials (Liu et al., 2002; Fougere et al.,2011). Another mutation close to the selectivity filter alters asparagine (N) to asparate (D) in position 629 (N629D). This point mutation caused kinetic changes and a decrease in potassium selectivity (Lees-Miller et al.,2000). The N629D mutation generates outward current during the plateau phase and an inward current during phase 3 repolarization in cardiac action potentials (Lees-Miller et al.,2000). This suggests that the reduction in potassium selectivity is causing an inward current (which is produced by inward sodium ions) during terminal repolarization and this is the cause of prolonged repolarization seen in LQTS (Lees-Miller et al.,2000; Vandenberg et al., 2012).

Similar to LQTS, T-type mutations to the turret can have drastic effects on physiology. Our mutant results demonstrate that point mutations of cysteine residues can significantly reduce calcium selectivity allowing for the passage of sodium ions and also altered channels kinetics. Increased sodium permeability can be fatal when the flow of sodium ions is not normal such as in the heart. Sodium ions permeable through T-type calcium channels will allow for quicker depolarization of the membrane and increase heart rate (Silverthorn, 2007). Increased heart rate could cause fatal cardiac arrhythmias.

Another known mutation in the turret region replaces a tryptophan residue with a cysteine in position 962 (W962C) in human Cav3.2 channels and it has been associated with autistic patients. Splawski and colleagues (2006) analyzed genomic sequences of patients with autism and expressed the wildtype Cav3.2 and mutants in recombinant human embryonic kidney cells (HEK293T) and perform electrophysiological recordings. Their results showed that the W962C mutant conducted less current, but did not differ from the wildtype Cav 3.2 in terms of activation and inactivation kinetics. However, there is a dramatic reversal potential change which is suggestive of reduced T-type channel selectivity for calcium ions and a greater monovalent ion permeability (Splawski et al 2006). The

autism phenotype caused by W962C may be associated with a reduction in functionally expressed Cav3.2 channels and/or the increase in sodium permeability of Cav3.2 channels.

4.10 Possible structural similarities between K_{2P} and K_{IR} and T-type calcium channels.

There are possible analogies between domain II of T-type calcium channels and the crystal structures of turret regions from two-pore potassium leak channels (K_{2P}) channels. K_{2P} channels comprises of two pore domains (P1 and P2) and four transmembrane segments (M1-M4) to form a dimer (Mathie, Al-moubarak & Veale,2010; Brohawn, del Marmol & MacKinnon, 2012). The turret on P1 contains ~56-60 amino acids on the extracellular side that forms an extracellular cap, known as the helical cap, it lies 35 Å above the extracellular side of the selectivity filter, resembling an A-frame structure. The cysteine residue located in P1 form a disulfide bond that links the two subunits together to form this cap, see Figure 4.2 (Miller & Long, 2012). Ion permeation is accessed from the two sides of the channel, preventing ions from entering from above due to the helical cap (Brohawn, del Marmol & MacKinnon, 2012; Miller & Long, 2012). The helical cap acts as a protective shield that prevents drug toxins from entering the pore. Similar to K_{2P} channels, eukaryotic inward-rectifying potassium channels (K_{ir}) possesses a smaller extended turret region that is enough to alter the external surface (Tao et al., 2009). K_{ir} and K_{2P} channels are resistant to classical invertebrate toxins that normally block voltage-gated potassium channels when applied externally and is likely caused by the helical cap (Tao et al., 2009; Brohawn, del Marmol & MacKinnon, 2012).

Vertebrate T-type calcium channels contain a uni-cysteine framework, in contrast to their invertebrate counterparts having either a tri- or –penta-cysteine structure in their turret regions. It is possible these cysteine residues in *Lymnaea* T-type channels play a role in creating disulfide bonds that form a helical cap similarly seen in $K_{2P.}$ We speculate that the course of evolution has altered the kind of extracellular structure for mammalian T-type calcium channels. Exon 12a is made up of fewer amino acids than exon 12b, and somehow changes to the turret and the descending helix confers a greater monovalent ion permeability.

The unique extracellular turrets forming a helical cap in T-type calcium channels may explain why there are no invertebrate pore-blocking toxins from cone snail, spider and snake venom that have been shown to block mammalian L-and N-type channels (Dorering & Zamponi, 2003). It is only in T-type channels (invertebrate and vertebrate) that have a consistent increase in the number of cysteine residues in extracellular turrets. NALCN, Cav1, Cav2 and Nav channels have six cysteines with a 4-0-2-0 configuration in turrets of Domains I-II-II-IV. This number of cysteines varies from 8 to 12 in some mammalian sodium channels. But this standard number of cysteines rises from a minimum of 13 to 19 cysteines in T-type channels. These larger number of cysteines in T-type channels reflects a unique adaptation for T-type channels within the four domain cation channels including NALCN, calcium channels and sodium channels.

Cysteine mutations in turrets of LCav3 channels have likely disrupted disulfide bonds thereby preventing proper conformation of an extracellular structure resembling the helical cap of K_{2P} channels. The disruption of the extracellular structure allows greater access to the selectivity filter because ions can enter from above without being pre-filtered through analogous side portal lined with charged residues observed for of K_{2P} channels. A K_{2P}-like extracellular structure stabilized by disulphide bonds likely forms above T-type channels. The apparent dismantling of this extracellular structure, increases the monovalent ion permeation, to a level where differing sized monovalent ions (Na+, K+, Li+) reach a saturating level of ion flow. The divalent ion passage is also compromised. Divalent ions have a weakened permeation and they have a weakened capability of blocking this overwhelming monovalent ion current flow. We observe an apparent concurrent ion flow of non-calcium divalent ions (barium) in the presence of monovalent ions, this is suggestive of a widened, accessible pore for the simultaneous entry of monovalent and divalent ions.

We also observed an increase in divalent metal cation sensitivity when cysteines in the turret are mutated in LCav3 - 12ΔC channels. The apparent dismantling of the extracellular structure leads to a loss of the toxin and drug shield to nickel and zinc, allowing for great access to the pore. Most modeling of divalent ion block of native channels includes

both low and high affinity blocking sites, and the extracellular turret adds a layer to the blockade that is likely more simplified when it is absent. Much of the turret sequences in domain II are unconserved amino acids, and these differences could provide unique external landscapes outside the pore, and unique countermeasures against the binding of specific toxins generated by differing predators against their T-type channels. Protostome invertebrates also have a requirement for sodium permeant T-type channels, and generated an alternative spliced variant in the Domain II turret as a solution for the lack of Nav1 sodium channels outside the brain and the lack of Nav1 channels in animals species such as the nematode, *C. elegans*. It is likely that both the requirements for flexible ion selectivity and modification of toxin binding, led to the evolution of the extended extracellular turret for T-type channels, which is absent in other calcium channel types, such as Cav1 and Cav2 channels. There is a certain vulnerability of T-type channels, inward rectifiers (such as KIR and hERG) and K_{2P} channels, because they commonly operate in the low voltage range, where toxin blockade dramatically alters the level of membrane excitability at rest.

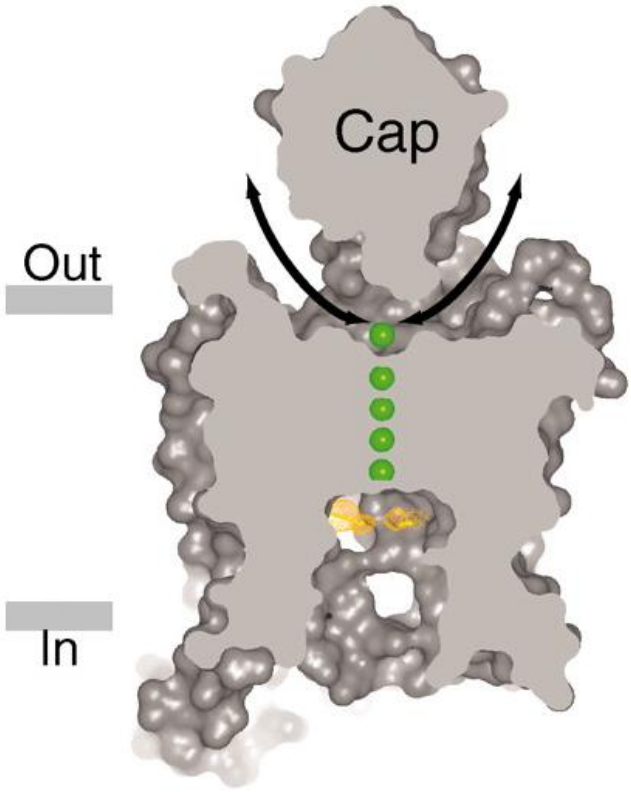

Figure 4.2. Side view K2P channel.

Turrets from the two-pore potassium channel form together to create an extracellular helical cap. Extracellular ions are pre-filtered by the helical cap, which lies just above the pore and ions access the selectivity pore from side portals. The shorter turret in LCav3-12a may produce a differing structure compared to LCav3-12b, which possesses a longer turret region, and also differing from mammalian T-type channels which also likely have a unique extracellular structure above them. (Reproduced from Miller & Long, 2012)

4.11 Future direction and considerations

Further research will be important to understand the mechanism of the extracellular turret and the role of cysteine residues in the turret. At the moment, the turret remains largely unexplored in its structure-function roles of four domain voltage gated ion channels. In the absence of a crystallography structure, it is difficult to determine the exact mechanisms behind the functioning of T-type calcium channels with extracellular turrets.

One set of experiments that can be carried out is to evaluate whether there are changes in the minimal pore size of T-type channels in LCav3 lacking cysteines compared to native LCav3 channels. We can carry out a similar experiment as Cataldi and colleagues (2002), where they defined the size of the pore of native T-type channels and other calcium channels by the degree of block with side chain derivatives of ammonium compounds. These compounds include mono-, di- , tri- and tetra- methyl ammonium compounds can be placed internally and a bi-ionic reversal experiment can be conducted to determine the pore cavity size. It is predicted that mono and di- methyl ammonium ions will be able to pass through the pore because their molecular sizes are smaller than cesium, whereas tri- and tetra- methyl ammonium compounds may be less permeable through the pore.

We have shown that barium in LCav3 channels lacking cysteines appear to have a weakened block for monovalent ion current. We can evaluate the strength of sodium block in an anomalous mole fraction effect experiment, where we add increasing extracellular concentrations of barium ions, in the presence of 60 mM external sodium ions, using identical concentrations as we did with external doses of calcium ions in the presence of sodium ions for previous anomalous mole fraction experiments. Another divalent ion, besides barium with a similar structure to calcium is strontium. Preliminary work suggest that strontium ranges between barium and calcium ions, and we have the possibilities of evaluating whether strontium behaves like barium in LCav3 channels lacking cysteines, with a reduced block of strontium ions of the sodium current.

We are interested in a better method to accurately measuring the relative permeabilities of sodium and calcium/barium ions. This method can be carried out using

instantaneous current voltage relationships (IIV). IIV provides a tail current that reflects the amount of current generated at a specific voltage without the complication of the concurrent gating of channels. It provides data on how voltage and ion concentration can affect ionic permeability assuming that the number of open channels remains constant and current sizes are affected by voltage (Khan et al, 2008). We can use equimolar concentrations of a monovalent ion such as sodium on both sides of the membrane producing a zero net charge at 0 mV, which should have an expected reversal potential at 0 mV. We can apply differing external concentrations of divalent cations such as calcium or barium and measure the changes to kinetics, current sizes and reversal potentials. It can provide a quantitative measure of the relative permeabilities of calcium and barium ions with the relative flux (inward and outward) for sodium ions.

We know that nickel and zinc block of T-type channels is enhanced in LCav3 channels lacking cysteine residues. Copper is a trace ion like zinc that is concentrated in the brain and implicated in modulating neuronal excitability in the normal and diseased brain (such as Alzheimer's Disease) (Lacinova, 2011). We can test whether the same increase in blocking potency with copper ions is observed for LCav3 T-type channels lacking cysteine residues.

We also have preliminary evidence that the most potent classes of T-type channel blockers known for blocking mammalian T-type channels (such as TTA-P2 and Z944) have no effect on snail LCav3 channels, unless we puncture the membrane. Once we puncture the membrane, the drug concentration of 1 uM, completely blocks the snail LCav3 channel, which is the dose used to block all mammalian T-type channels. TTA-P2 is as potent at blocking snail T-type channels, but is unable to access the pore by an external pathway. We have received high affinity T-type channel blocker, Z944 from Terry Snutch, of Zalicus Pharmaceuticals. Z944 is in phase 2 clinical trials for treatment of chronic pain. We will test whether the turret regions interfere with drug access of snail T-type channels. We hypothesize that the external structure above the snail T-type channel serves as a toxin shield that prevents external access for TTA-P2 and Z944. We will test the external access of TTA-

P2 and Z944 for its block of LCav3 channels lacking cysteines, to evaluate whether the external structure serves as a protective structure against drug access. Divalent metal ion and drug response profiles should also be conducted for LCav3-α1H to investigate whether or not there are changes to drug sensitivity for these channels too.

It is likely that the turret in Domain II partners with other domains, likely the Domain IV turret region which is across from it in the three dimensional structure of T-type channels. Inter-subunit interactions could generate the analogous external structure in K_{2P} channels (Miller and Long, 2012). Domain II and Domain IV turrets could form inter-subunit disulphide bonds. We want to carry out double swaps of Domain II and IV turrets in mammalian and snail T-type channels, and determine whether these turrets alone will confer the drug access properties, and the altered calcium and sodium permeation that is characteristic for each channel.

Some of the unique features of T-type channel may be obscured because our recordings are at the whole cell level. We can also carry out single channel recordings to get a sense of single channel opening times, refractory times and divalent ion permeability, especially the peculiar observations seen when barium is the charge carrier. In addition, it would be interesting to carry out microelectrode or current clamp recordings on snail cardiomyocytes (possessing mostly sodium permeant, LCav3-12a channels) and prostate and/or albumin glands (possessing more calcium selective, LCav3-12b channels) to evaluate how modified calcium and sodium permeability affects electrical activity in a more native physiological context.

Chapter 5
General Conclusions

Mechanisms surrounding ion permeability and selectivity in T-type channels remain highly undiscovered. Evidently, T-type calcium channels can generate varying sodium permeability in the presence of different extracellular turrets with changes in 7 to 10 amino acids. We have shown that alternative splicing of exon 12 can generate sodium permeable T-type channels that are absent in the more calcium selective mammalian T-type channels. The original hypothesis focused on creating a uni-cysteine turret to mimic the structure of calcium selective mammalian T-type channels. This hypothesis was not supported by the data collected because mutations of cysteines produced voltage gated calcium channels that were less selective for divalent and monovalent cation ions. Instead, LCav3 channels lacking cysteines generated T-type channels that were more sodium permeable, less calcium permeant, with a weakened capacity for divalent cations (except for calcium) to block the monovalent ion currents. The block of divalent metal cations such as nickel and zinc, dramatically increase, and our evidence suggests that the cysteine mutations in the turret dismantled the external structure that serves as a drug and toxin shield that is similar to K_{2P} channels. Placing the exon 12 turret from Cav3.2 (LCav3-α1H) was insufficient for creating a calcium selective channel on its own, and it is likely the domain II turret works with other regions of the T-type channel to confer sodium and calcium permeation.

This thesis has provided a basis to challenge the notion that the selectivity filter is the only regulator for the sodium and calcium selectivity in four domain ion channels. It also questions the notion that T-type channels are exclusive members within the calcium channel family, and that they can also be classified as sodium channels, at least in protostome invertebrates. The exclusive expression of the highly sodium permeant T-type channel observed in the snail heart, brings to light that there are differences in the primitive invertebrate heart for generating cardiac action potentials. Finally, these results provides a foundation for future drug development research, where it is clear that the extracellular turret

is an important structural element for regulating drug access and affinity, besides its influences on gating and ion selectivity.

References

Arias- Olguín, I.I., Vitko, I., Fortuna, M., Baugart, J., Sokolova, S., Shumilin, I.A., Van Deusen, A., Soriano-García, M., Gomora, J.C., & Perez-Reyes, E. (2008). Characterization of the gating brake in the I-II loop of Cav3.2 T-type Ca^{2+} channels. *The Journal of Biological Chemistry,* 283 (13), 8136-8144.

Anderson, P.A.V., & Greenberg, R.M. (2001). Phylogeny of ion channels: clues to structure and function. *Comparative Biochemistry and Physiology,* 129,17-28.

Armstrong, C.M. (1971). Interaction of tetraethylammonium ion derivatives with the potassium channels of giant axons. *Journal of General Physiology,* 258 (4), 413-437.

Baumgart, J.P., Vitko, I., Bidaud, I., Kondratskyi, A., Lory, P., & Perez-Reyes, E. (2008). I-II loop structural determinants in the gating and surface expression of low voltage-activated calcium channels. *PLoS one,* 3 (8), e2976. doi:10.1371/journal.pone.0002976.

Berneche, S., Roux, B., (2003). A microscopic view of ion conduction through the K+ channel. *PNAS,* 100 (15), 8644-8648.

Broshawn, S.G., del Marmol, J., MacKinnon, R. (2012). Crystal structure of the human K2P TRAAK, a lipid- and mechano-sensitive K+ ion channel. *Science,* 335, 436-441.

Burgess, D.E., Crawford, O., Delisle, B.P., & Satin, J. (2002). Mechanism of inactivation gating of human T-type (low-voltage activated) calcium channels. *Biophysical Journal,* 82, 1894-1906.

Cataldi, M., Perez-Reyes, & Tsien, R.W. (2002). Differences in apparent pore sizes of low and high voltage-activated ca2+ channels. *Journal of Biological Chemistry,* 277 (48), 45969-45976.

Catterall, W.A. (1995). Structure and function of voltage-gated ion channels. *Annual Reviews of Biochemistry,* 64, 493-531.

Catterall, W.A. (2010). Ion channel voltage sensors: structure, function and pathophysiology. *Neuron,* 67 (6), 915-928.

Chemin, J., Monteil, A., Perez-Reyes, Bourinet, E., Naregot, J., & Lory, P. (2002). Specific contribution of human T-type calcium channel isotypes (α_{1G}, α_{1H}, α_{1I}) to neuronal excitability. *Journal of Physiology,* 5(1),3-14.

Cheong, E., & Shin, H.S. (2013). T-type Ca^{2+} channels in absence epilepsy. *Biochimica et Biophysica Acta,* 1828, 1560-1571.

Choi, K.L., Aldrich, R.W., & Yellen, G. (1991). Tetraethylammonium blockade distinguishes two inactivation mechanisms in voltage-activated K+ channels. *PNAS*, 88, 2092-5095.

Cibulsky, S.M, & Sather, W.A. (2000). The EEEE locus is the sole high affinity Ca^{2+} binding structure in the pore of a voltage-gated Ca^{2+} channel: block by Ca2+ entering from the intracellular pore entrance. *Journal of General Physiology*, 116, 349-362.

Cribbs, L.L, Lee, H.H., Yang, J., Satin, J., Zhang, Y., Daud, A., Barclay, J., Williamson, M.P., Fox, M., Rees, M., & Perez-Reyes, E. (1998). Cloning and characterization of alpha1H from heart, a member of the T-type Ca2+ channel gene family. *Circulation Research*, 83, 103-109.

Cribbs, L.L., Martin, B., Schroder, E.A., Keller, B.B., Delisle, B.P., & Satin, J. (2001). Identification of the T-type calcium channel (Cav3.1d) in developing mouse heart. *Circulation Research*, 88, 403-407.

Dang, T.X., & McCleskey, E.W. (1998). Ion channel selectivity through stepwise changes in binding affinity. *Journal of General Physiology*, 111, 185-193.

Dawson, D.F., Boone, A.N., Senatore, A., Pitcaru, J., Thiyagalingam, S., Jackson, D., Davison, A., & Spafford, J.D. (2014). Gene slicing of an invertebrate beta subunit (LCavβ) in the N-terminal and HOOK domains and its regulation of LCav1 and LCav2 calcium channels. *PLoS One*, 9 (4), doi: 10.1371/journal.pone.0092941.

Deschênes, M., Paradis, M., Roy, J.P., & Sterlade, M. (1984). Electrophysiology of neurons of lateral thalamic nuclei in cat: resting properties and burst discharges. *Journal of Neurophysiology*, 51, 1196-1219.

Diaz, D., Bartolo, R., Delgadillo, D., Higueldo, F., & Gomora, J.C. (2005). Contrasting effects of Cd2+ and Co2+ on the blocking/unblocking of human Cav3 channels. *Journal of Membrane Biology*, 207 (2), 91-105.

Doering, C.J., and Zamponi, G.W. (2003). Molecular pharmacology of high voltage-activated calcium channels. *Journal of Bioenergetics and Biomembranes*, 35, 491-505.

Doyle, D.A., Morais Cabral, J., Pfuetzner, R.A., Kuo, A., Gulbis, J.M., Cohen, S.L., Chait., B.T., & MacKinnon, R. (1998). The structure of the potassium channel: molecular basis of K+ conduction and selectivity. *Science*, 280 (5360), 69-77.

Dun, W., Jiang, M., & Tseng, G.N. (1999). Allosteric effects of mutations in the extracellular S5-P loop on the gating and ion permeation properties of hERG. *Pflugers Archiv: European Journal of Physiology*, 439, 141-149.

Eisenman,G., Sandbolm, J.P., and Walker, J.L. (1967). Membrane structure and ion permeation. Study of ion exchange membrane structure and function is relevant to analysis of biological ion permeation. *Science,* 155, 965-974.

Fabiato, A. (1992). Two kinds of calcium-induced release of calcium from sarcoplasmic reticulum of skinned cardiac cells. *Advances in Experimental Medicine and Biology*, 311, 245-262.

Fan, J.S., Jiang, M., Dun, W., McDonald, T.V., & Tseng, G.N. (1999). Effects of outer mouth mutations on hERG channel function: a comparison with similar mutations in the *Shaker* channel. *Biophysical Journal*, 76, 3128-3140.

Fougere, R.R., Es-Salah-Lamoureux, Z., Rezazadeh, S., Eldstrom, J., & Fedida, D. (2011). Functional characterization of the LQT2-causing mutation R582C and the associated voltage-dependent fluorescence signal. *Heart Rhythm*, 8 (8), 1273-1280.

Gardner, D.R., & Brezden, B.L. (1990). Ion channels in *Lymnaea Stagnalis* heart ventricle cells. *Computational Biochemistry Physiology*, 96A (1), 79-85.

Gillespie. D., & Boda, D. (2008). The anomalous mole fraction effect in calcium channels: a measure of preferential selectivity. *Biophysical Journal*, 95, 2658-2672.

Grant, A.O. (2009). Cardiac ion channels. *Circulation Arrhythmia Electrophysiology*, 2, 185-194.

Hagiwara, S., Fukuda, J., Eaton, D.C. (1974). Membrane currents carried out by Ca2+, Sr2+ and Ba2+ in barnacle muscle fiber during voltage clamp. *Journal of General Physiology*, 63, 565-578.

Hagiwara N, Irisawa H, & Kameyama M (1988). Contribution of two types of calcium currents to the pacemaker potentials of rabbit sino-atrial node cells. *Journal of Physiology*, 395, 233-253.

Hagiwara, S., Ozawa, S., & Sand O. (1975). Voltage clamp analysis of two inward current mechanisms in the egg cell membrane of a starfish. *The Journal of General Physiology*, 65 (5), 617-644.

Heinemann, S.H., Terlau, H., Stuhmer, W., Imoto, K., & Numa,S. (1992). Calcium channel characteristics conferred on the sodium channel by single mutations. *Nature*, 356, 441-443.

Hess, P., Lansman, J.B., Tsien, R.W. (1986). Calcium channel selectivity for divalent and monovalent cations. Voltage and concentration dependence of single channel currents in ventricular heart cells. *Journal of General Physiology*, 88, 293-319.

Highshima, M., Kinoshita, H., & Koshino, Y. (1998). Contribution of T-type calcium channels to afterdischarge generation in rat hippocampal slices. *Brain research*, 781, 127-134.

Hille, B. (3rd Ed.). (2001). *Ion channels of excitable membranes*. Sunderland, Massachusetts: Sinauer Associates.

Jiang, M., Zhang, M., Maslennikov, I.V., Liu, J., Wu, D.M., Korolkova, Y.V., Arseniev, A.S., Grishin, E.V., & Tseng, G.N. (2005). Dynamic conformational changes of extracellular S5-P linkers in hERG channel. *Journal of Physiology*, 569 (1), 75-89.

Jimenez- Vargas, J.M., Restano- Cassulini, R.R. & Possani, L.D.(2012). Toxin modulators and blockers of hERG K+ channels. *Toxicon*, 60, 492-501.

Kang, H.W., Park, J.Y., Jeong, S.W., Kim, J.A., Moon, H.J., Perez-Reyes, & E., Lee, J.H. (2006). A molecular determinant of nickel inhibition in Cav3.2 T-type calcium channels. *The Journal of Biological Chemistry*, 281 (8), 4823-4830.

Kim, D., Song, I., Keum, S., Lee, T., Jeong M.J., Kim, S.S., McEnery, M.W., & Shin H.S. (2001). Lack of the burst firing of thalamocortical relay neurons and resistance to absence seizures in mice lacking α1G T-type Ca^{2+} channels. *Neurons*, 31, 35-45.

Klöckner, U., Lee, J., Cribbs, L.L., Daud, A., Hescheler, J., Pereverev, A., Perez-Reyes, E., & Schneider, T. (1999). Comparison of the Ca^{2+} currents induced by expression of three cloned α1 subunits, α1G, α1H, α1I, of low-voltage-activated T-type Ca^{2+} channels. *European Journal of Neuroscience*, 11 (12), 4171-4178.

Kostyuk, P.G., Mironov, S.L., & Ya, M.S. (1983). Two ion-selecting filters in the calcium channels of the somatic membrane of mollusk neurons. *Journal of Membrane Biology*, 76, 83-93.

Lacinova, L. (2011). T-type calcium channel blocks – new and notable. *General Physiology and Biophysics*, 30, 403-409.

Larsen, J.K., Mitchell, J.W., Best, P.M.. (2002). Quantitative analysis of the expression an distribution of calcium channel alpha 1 subunit mRNA in the atria and ventricles of the rate heart. *Journal of Molecular and Cellular Cardiology*, 34, 533-546.

Lee, J., Kim, D., & Shin, H.S. (2004). Lack of delta waves and sleep disturbances during non-rapid eye movement in sleep in mice lacking alpha1G-subunit of T-type calcium channels. *PNAS*, 101, 18195-18199.

Lee, J., Kim, D., & Shin, H.S. (2004). Lack of delta waves and sleep disturbances during non-rapid eye movement in sleep in mice lacking alpha1G-subunit of T-type calcium channels. *PNAS*, 101, 18195-18199.

Lee, J., & Shin, H.S. (2007). T-type calcium channels and thalamcortical rhythms in sleep: a perspective from studies of T-type calcium channel knockout mice. *CNS & Neurological Disorders – Drug targets*, 6 (1), 63-70.

Lees-Miller, J.P., Duan, Y., Teng, G.Q., Thorstad, K., & Duff, H.J. (2000). Novel gain-of-function mechanism in K+ channel- related long QT syndrome: altered gating and selectivity in the HERG1 N629D mutant. *Circulation Research*, 86(5), 507-513.

Levine, T.B., Bernink, P.J., Caspi, A., Elkayam, U., Geltman, E.M., Greenberg, B., McKenna, W.J., Ghali, J.K, Giles, T.D., Marmor, A., Reisin, L.H., Ammon, S., & Lindberg, E. (2000). Effect of mibefradil, a T-type calcium channel blocker, on morbidity and mortality in moderate to severe congestive heart failure: the MACH-1 study. Mortality assessment in congestive heart failure trail. *Circulation*,101 (7), 758-764.

Li, J., Stevens, L., & Wray, D. (2005). Molecular regions underlying the activation of low- and high-voltage activating calcium channels. *European Biophysics Journal*, 34, 1017-1029.

Liu, J., Zhang, M., Jiang, M., & Tseng, G.N. (2002). Structural and functional role of the extracellular S5-P linker in the HERG potassium channel. *Journal of General Physiology*, 120 (5), 723-737.

Llinas, R., & Yarom, Y. (1981). Electrophysiology of mammalian inferior olivary neurons in vitro. Different types of voltage-dependent ionic conductances. *Journal of Physiology*, 315, 549-567.

Lopez-Barneo, J., Hoshi,T., Heinermann, S.H. & Aldrich, E.W. (1993). Effects of external cations and mutations in the pore region of C-type inactivation of *Shaker* potassium channels. *Receptors Channels,* 1, 61-71.

Martinez, M.L., Heredia, M.P., & Delagado, C. (1999). Expression of T-type Ca2+ channels in ventricular cells from hypertrophied rat hearts. *Journal of Molecular and Cellular Cardiology*, 31, 1617-1625.

Mathie, A., Al-Moubarak, E., & Veale, E.L. (2010). Gating of two pore domain potassium channels. *Journal of Physiology,* 588 (17), 3149-3156.

McCleskey, E.W. (1999).Calcium channel permeation: a field in flux. *Journal of General Physiology,* 113 (6), 765-772.

McComb, C., Varshney, N., & Lukowiak, K. (2005). Juvenile *Lymnaea* ventilate, learn and remember differently than do adult *Lymnaea*. *Journal of Experimental Biology*, 208, 1459 – 1467.

Miller, A.N., & Long, S.B. (2012). Crystal structure of the human two-pore domain potassium channel K2P1. *Science*, 335, 432-436.

Mitchell, J.W., Larsen, J.K., & Best, P.M. (2002). Quantitative analysis of the expression and distribution of calcium channel alpha subunit mRNA in the atria and ventricles of the rat heart . *Journal of molecular and cellular cardiology*, 34 (5), 519-532.

Monteil, A., Chemin, J., Leuranguer, V., Altier, C., Mennessier, G., Bourinet, E., Lory, P., & Nargeot, J. (2000). Specific properties of T-type calcium channels generated by the human α_{1I} subunit. *The Journal of Biological Chemistry*, 275 (22),16530-16535.

Nagle, G.T., de Jong-Brink, M., Painter, S.D., and Li, K.W. (2001). Structure, localization and potential role of a novel molluscan trypsin inhibitor in *Lymnaea*. *European Journal of Biochemistry,* 268, 1213-1221.

Nelson, M.T., Woo, J., Kang, H.W., Vitko, I., Barrett, P.Q., Perex-Reyes, E., Lee, J.H., Shin, H.S., & Todorovic, S.M. (2007). LaReducing agents of sensitive C-type nociceptor by relieving high-affinity zinc inhibition of T-type calcium channels. *Neurons*, 31, 35-45.

Nimigean, C.M., & Allen, T.W. (2011). Origins of ion selectivity in potassium channels from the perspective of channel block. *Journal of General Physiology*, 137 (5), 405-413.

Nosal, O.V., Lyubanova, O.P., Naidenov, V.G., & Shuba, Y.M. (2013). Complex modulation of Cav3.1 T-type calcium channel by nickel. *Cellular and Molecular Life Sciences* 70, 1653-1661.

Noskov, S.Y., & Roux, B.. (2006). Ion selectivity in potassium channels. *Biophysical Chemistry,* 124, 279-291.

Nuss, H.B.,& Houser, S.R. (1993). T-type Ca^{2+} current is expressed in hypertrophied adult feline left ventricular myocytes. *Circulation Research*, 73, 777-782.

Ono, K., & Iijima, T. (2005). Pathophysiological significant of T-type Ca^{2+} channels: properties and functional roles of T-type Ca^{2+} channels in cardiac pacemaking. *Journal of Pharmacological Sciences*, 99, 194-204.

Ono, K., & Iijima, T. (2010). Cardiac T-type Ca2+ channels in the heart. *Journal of Molecular and Cellular Cardiology*, 48, 65-70.

Ouadid, H., Seguin, J., Richard, S., Chaptal, P.A., & Nargeot, J. (1991). Properties and modulation of Ca channels in adult human atrial cells, *Journal of Molecular and Cellular Cardiology*, 23, 41-54.

Park, H.J., Park, S.J., Ahn, E.J., Lee, S.Y., Seo, H., Lee, J.H. (2013). Asp residues of the Glu-Glu-Asp-Asp pore filter contribute to ion permeation and selectivity of the Cav3.2 T-type channel. *Cell Calcium,* 54 (3), 226-235.

Payandeh, J., Scheuer, T., Zheng, N., & Catterall, W.A. (2011). The crystal structure of a voltage- gated sodium channel. *Nature,* 475, 353-358.

Perez-Reyes, E. (2003). Molecular physiology of low-voltage-activated T-type calcium channels. *Physiological Reviews*, 83, 117-161.

Perez-Reyes, E. (2010). Characterization of the gating brake in the I-II loop of Cav3 T-type calcium channels. *Channels,* 4 (6), 453-458.

Ren, D., Navarro, B., Xu, H., Yue, L., Shi, Q., & Clapham, D.E. (2001).A prokaryotic voltage-gated sodium channel. *Science*, 294 (5550), 2372-2375.

Sather, W.A., & McCleskey, E.W. (2003). Permeation and selectivity in calcium channels. *Annual Reviews of Physiology*, 65, 133-159.

Satoh, H. (2003). Sino-atrial nodal cells of mammalian hearts: ionic currents and gene expression of pacemaker ionic channels. *Journal of Smooth Muscle Research,* 39 (5), 175-193.

Schlief, T., Schonherr, R., Imoto, K., & Heinemann, S.H. (1996). Pore properties of rat brain II sodium channels mutated in the selectivity filter domain. *European Biophysics Journal* 25 (2), 75-91.

Sen, L., & Smith, T.W. (2012). T-type Ca2+ channels are abnormal in genetically determined cardiomyopathic hamster hearts. *Circulation Research,* 75 (1), 149-155.

Senatore, A. (2012). *Alternative splicing of Lymnaea Cav3 and NALCN ion channel genes serves to alter biophysical properties, membrane expression, and ion selectivity* (Doctoral dissertation, University of Waterloo, Ontario, Canada). Retrieved from https://uwspace.uwaterloo.ca/handle/10012/6926

Senatore, A., Boone, A.N., Lam, S., Dawson, T.F., Zhorov, B.S. & Spafford, J.D. (2011). Mapping of dihydropyridine binding residues in a less sensitive invertebrate L-type calcium channel (LCa_v1). *Channels,* 5(2), 173-187.

Senatore, A., Guan, W., Boone, A.N. & Spafford, J.D. (2014). T-type channels become highly permeable to sodium ions with an alternate extracellular turret region (S5-P) outside the selectivity filter. *Journal of Biological Chemistry,* doi:10.1074/jbc.M114.551473.

Senatore, A., Guan, W., & Spafford, J.D. (2014). Cav3 T-type channels: regulators for gating, membrane expression, and cation selectivity. *Pflugers Archive: European Journal of Physiology,* 466 (4), 645-660.

Senatore, A. & Spafford, J.D. (2006). Transient and big are key features in an invertebrate T-type channel (LCav3) from the central nervous system *of Lymnaea stagnalis*. *The Journal of Biological Chemistry,* 285 (10), 7447-7458.

Senatore, A. & Spafford, J.D. (2012). Gene transcription and splicing of T-type channels are evolutionarily conserved strategies for regulating channel expression and gating. *PLoS ONE,* 7 (6): e37409, doi:10.1371/journal.pone.0037409.

Senatore, A., Zhorov, B.S., & Spafford, J.D. (2012). Cav3 T-type calcium channels. *WIREs Membrane Transport and Signal*, 1: 467-491. doi:10.1002/wmts.41

Senatore, A., Boone, A. N., & Spafford, J.D. (2011).Optimized transfection strategy for expression and electrophysiological recording of recombinant voltage-gated ion

channels in HEK-293T cells. *Journal of Visualized Experiments*, (47): e2314 10.3791/2314, doi:10.3791/2314.

Serrano, J.R., Perez-Reyes, E., & Jones, S.W. (1999). State-dependant inactivation of the α1G T-type calcium channel. *Journal of General Physiology* 114, 185-201.

Shcheglovitov, A., Kostyul, P., & Shuba, Y. (2007). Selectivity signatures of three isoforms of recombinant T-type Ca^{2+} channels, *Biochmica et Biophysica Acto*, 1768 (6), 1406-1419.

Shcheglovitov, A., & Shuba, Y. (2006). Sodium/calcium selectivity of cloned calcium T-type channels, *Neurophysiology*, 38 (3), 149-157.

Shi, W., Wymore, R.S., Wang, H.S., Pan, Z., Cohen, I.S., McKinnon, D., & Dixon, J.E. (1997). Identification of two nervous system- specific members of the erg potassium channel gene family. *Journal of Neuroscience*, 17, 9423-9432.

Shuba, Y.M. (2014). Models of calcium permeation through T-type channels. *Pflugers Archive – European Journal of Physiology*, doi: 10.1007/s00424-013-1437-3.

Silverthorn, D.U. (4^{th} Ed.). (2007). *Human physiology: an integrated approach*. San Francisco, California: Pearson Education.

Spafford, J.D., Dunn, T.P., Smit, A.B., Syed, N.I., & Zamponi, G.W. (2006). In vitro characterization of L-type calcium channels and their contribution to firing behavior in invertebrate respiratory neurons. *Journal of Neurophysiology*, 95 (1), 42-52.

Splawski, I., Yoo, D.S., Stotz, S.C., Cherry, A., & Clapham, D.E. (2006). CACNA1H mutations in autism spectrum disorders. *Journal of Biological Chemistry*, 281 (31), 22085-22091.

Staras, K., Gyori, J., & Kemenes, G. (2002). Voltage-gated ionic currents in an identified modulatory cell type controlling molluscan feeding. *European Journal of Neuroscience*, 15 (1), 109-119.

Steriade, M. (2005). Sleep, epilepsy and thalamic reticuluar inhibitory neurons. *Trends in Neuroscience*, 28, 317-324.

Strong, M., Chandy, K.G., & Gutman, G.A. (1993). Molecular evolution of voltage-sensitive ion channel genes: on the origins of electrical excitability. *Molecular Biology and Evolution* 10, 221-242.

Tao, X., Avalos, J.L., Chen, J., and MacKinnon, R. (2009). Crystal structure of the eukaryotic strong inward-rectifier K+ channel Kir2.2 at 3.1 Å resolution. *Science,* 326, 1668-1674.

Talavera, K.,Staes, M., Janssens, A., Klugbauer, N., Droogmans, G., Hoffman, F., & Nilius, B. (2001). Aspartate resides of the Glu-Glu-Asp-Asp (EEDD) pore locus control selectivity and permeation of the T-type Ca2+ channel alpha (1G). *Journal of Biological Chemistry*, 276, 45628-45638.

Talavera, K., Janssens, A., Klugbauer, N., Droogmans, G., & Nilius, B. (2003). Pore structure influences gating properties of the T-type Ca2+ channel α_{1G}. *Journal of General Physiology*, 121, 529-540.

Talavera, K., & Nilius, B. (2006). Biophysics and structure – function relationship for T-type Ca2+ channels. *Cell Calcium*, 40, 97-114.

Tang, L., Gamal El-Din, T.M., Payandeh, J., Martinez, G.Q., Heard, T.M., Scheuer, T., Zheng, N., & Catterall, W.A. (2014). Structural basis for Ca2+ selectivity of a voltage-gated calcium channel. *Nature*, 505, 56-61.

Traboulsie, A., Chemin, J., Chevalier, M., Quignard, J.F., Nargeot, J., & Lory, P. (2007). Subunit-specific modulation of T-type calcium channels by zinc. *Journal of Physiology*, 578 (1), 159-171.

Torres, A.M., Bansal, P.S., Sunde, C., Clarke, C.E., Bursill, J.A., Smith, D.J., Bauskin, A., Breit, S.N., Campbell, T.J., Alewood, P.F., Kuchel, P.W., & Vandenberg, J.I. (2003). Structure of the HERG K+ channel S5P extracellular linker: role of an amiphipathic α-helix in C-type inactivation. *Journal of Biological Chemistry*, 278, 42136-42148.

Van Horn, J.D., Bulaj, G., Goldenberg, D.P., & Burrow C.J. (2003). The Cys-Xaa-His metal binding motif: {N} versus {S} coordination and nickel mediated formation of cysteinyl sulfinic acid. *Journal of Biological Inorganic Chemistry*, 8, 601-610.

Vandenberg, J.I., Perry, M.D., Perrin, M.J., Mann, S.A., Ke, Y., & Hill, A.P. (2012). hERK K+ channels: structure, function and clinical significance. *Physiological Reviews*, 92, 1393-1478.

Vassort, G., Talavera, K., & Alvarez, J.L. (2006). Role of T-type Ca2+ channels in the heart. *Cell Calcium*, 40, 205-220.

Vitko, I., Bidaud, I., Aria, J.M., Mezghrani, A., Lory, P., & Perez-Reyes, E. (2007). The I-II loop controls plasma membrane expression and gating of Cav 3.2 T-type Ca^{2+}

channels: a paradigm for childhood absence epilepsy mutations. *Journal of Neuroscience*, 27(2), 322-330.

Vitko, I., Chen, Y., Arias, J.M., Shen, Y., Wu.X.R., & Perez-Reyes, E. (2005). Functional characterization and neuronal modeling of the effects of childhood absence epilepsy variants of CACNA1H, a T-type calcium channel. *Journal of Neuroscience*, 25 (19), 4844-4855.

Walsh, C.P., Davies, A., Butcher, A.J., Dolphin, A.C., & Kitmitto, A. (2009). Three-dimensional structure of Cav3.1: comparison with the cardiac L-Type voltage-gated calcium channel monomer architecture. *Journal of Biological Chemistry*, 284 (33), 22310-22321.

Xu, C.Q., Zhu, S.Y., Chi, C.W., & Tytgat, J. (2003). Turret and pore block of K+ channels: what is the difference?. *TRENDS in Pharmacological Sciences*, 24 (9), 446-448.

Yeoman, M.S., Brezden, B.L., & Benjamin, P.R. (1999). LVA and HVA Ca^{2+} currents in ventricular muscle cells of the *Lymnaea* Heart. *Journal of Neurophysiology*, 82, 2428-2440.

Yang, J., Ellinor, P.T., Sather, W.A., Zhang, J.F.,& Tisen, R.W. (1993). Molecular determinants of Ca^{2+} selectivity and ion permeation in L-Type Ca^{2+} channels. *Nature*, 366, 158-161.

Zamponi, G.W. (2005). *Voltage- gated calcium channels*. New York, New York:Eurekah.com and Kluwer Academic/ Plenum.

Zhang, Y., Mori, M., Burgess, D.L., & Noebels., J.L. (2002). Mutations in high-voltage-activated currents in mouse thalamic relay neurons. *Journal of Neuroscience*, 22, 6362-6371.

Zhou, Z., & Lipsius, S.L. (1994). T-type calcium current in latent pacemakers cells isolated from cat right atrium. *Journal of Molecular Cell Cardiology*. 26, 1211-1219.